Coupling of two natural complex systems: earthquake-triggered landslides

by

Masoumeh Ghahramani

A thesis
presented to the University of Waterloo
in fulfillment of the
thesis requirement for the degree of
Master of Science

in
Earth Sciences

Waterloo, Ontario, Canada, 2012

© Masoumeh Ghahramani 2012

AUTHOR'S DECLARATION

I hereby declare that I am the sole author of this thesis. This is a true copy of the thesis, including any required final revisions, as accepted by my examiners.

I understand that my thesis may be made electronically available to the public.

Abstract

This thesis contains two main parts. The first part presents a database compiling 137 landslide-triggering earthquakes (LTEs) worldwide, with magnitudes greater than the minimum observed threshold for causing landslides (M4.5), for the period of 1998 -2009. Our data sources include a comprehensive review of the existing literature on earthquake-triggered landslides (ETLs), and also a USGS-based earthquake catalog (PAGER-CAT) that contains information on earthquake-triggered secondary events. Only 14 earthquakes out of the 137 seismic events induced significant numbers of landslides (>250). We compared the number of ETLs with the total number of earthquakes with $M \geq 4.5$ (n=68,734*)* during the same period of time. The results show that only 0.2 % of ETLs and only 4.5% of earthquakes of $M > 6$ resulted in landslide. In addition, we compiled a database of 37 large-scale landslides, involving initial failure volumes of greater than 20 Mm^3 that occurred worldwide between 1900 to 2010. The database contains large-scale earthquake-triggered ($n_{ETLs}=18$) and non-earthquake-triggered landslides ($n_{NETLs}=20$), i.e., ca. 50% of large-scale landslides were induced by seismic activity. Surprisingly, the volume-temporal frequency curves of ETLs and NETLs show almost identical slopes and intercepts. Thus, for a given volume, the annual frequency of ETLs is almost identical to that of NETLs in the 110 year period. In contrast to previous studies, this thesis found that the volume of the largest landslide triggered by a given landslide-triggering earthquake is not a function of earthquake magnitude. Peak ground motions (PGA, PGV, and PSA) were calculated for the 18 large-scale ETLs at the site of each occurrence and the resulting values show a correlation with the volume of landslides below the threshold of ca. 80 Mm^3. Above this threshold, the relationship between peak ground motions and ETL volume shows complex and nonlinear behavior. The results suggest that 1) other special conditions are required for significant earthquake-triggered landslides to occur, and 2) that very large earthquake-triggered landslides (volume greater than 80 Mm^3) result from complex progressive failure mechanisms initiated by seismic shaking (i.e., above this threshold volume, landslide volume is independent of PGA, PGV, and PSA).

A detailed analysis of the two 1985 Nahanni earthquakes and the North Nahanni rockslide triggered by the first main shock is carried out in the second part of the study. The North Nahanni rockslide, Northwest Territories, Canada was triggered by the earthquake of M=6.6 on October 5th, 1985. The slide occurred in a Palaeozoic carbonate sequence along a thrust fault, which partly follows bedding and partly cuts across bedding. The sliding surface within the limestone consisted of two planes; the lower plane dipped at 20° while the upper plane dipped at 35°. Slope stability analysis is performed using discontinuum numerical modeling. Static slope stability analyses indicate that the sliding rock was marginally safe for the sliding surface friction angles of 24^o or higher. Dynamic analyses of the co-seismic movements are conducted by applying a series of sinusoidal waves to the base of the model. The amplitudes of the October earthquake's seismic waves are estimated using strong motion data available from the second main shock. The results, from the dynamic analysis indicate that the slope becomes unstable for given seismic inputs at a specific range of friction angles (24^o to 30^o) for the sliding surface and the deformation behavior of the North Nahanni rock masses is dependent on the frequency of the seismic signals. Because the static slope stability analysis showed that the slope was close to instability prior to the seismic shaking, we suggest that the 1985 Nahanni earthquake operated as a trigger event that accelerated the occurrence of the slide. This finding supports our earlier results of the global scale study, which showed that the triggering event does not change the general trend of the frequency-volume distribution of landslides; however, it can accelerate the occurrence of slope failure.

Acknowledgements

It is a pleasure to thank those who made this thesis possible. Firstly, I would like to express my sincere gratitude to Prof. Stephen Evans for his supervision, patient guidance, support, and excellent advice throughout my research project. Secondly, I am most grateful to Prof. Gail Atkinson for her advices, and insightful comments on aspects of seismology presented in this work as well as her constructive feedback on my thesis. I would also like to thank Prof. Giovanni Cascante for his valuable discussions and accessibility.

I would also acknowledge Dr. Karen Assatourians for all discussions we had, and his willingness to share his bright thoughts with me. Many thanks to my friends and colleagues in particular to Keith Delaney, Behrad Madjdabadi, and Mona Khalegy Rad for their help and supports, it was great to collaborate with all of you. My special thanks go to Mary McPherson for the great feedback and reviews on my thesis.

Lastly, I am very thankful to my family. They have always supported, encouraged, and inspired me in every step of my life, and in particular, I would like to thank my husband and best friend, Mohamad Niknam, without whose love, support, and assistance, I would not have finished this thesis.

Dedication

This thesis is dedicated to

my loving parents, Behnaz and Nader

and my dear husband, Mohamad.

Table of Contents

List of Figures

List of Tables

Chapter 1

Introduction

1.1 Context

Many geophysical processes display complex behavior. In general, complex systems are sensitive to initial conditions, and minor disturbances may lead to chaotic behavior (Bak 1996, Newman and Turcotte, 2002). Bak et al. (1987) were the first to introduce the concept of self-organized criticality in order to explain the behavior of a complex system, the "sand pile" model. In self-organized criticality, the input to the "sand pile" model is constant, whereas the output is a series of events or “avalanches”. The noncumulative frequency-area distribution of model ‘avalanches’ is known to follow a power-law distribution (Bak et al. 1987, Bak 1996, Turcotte, 1999):

$$N = A^{-b} \qquad \textbf{(1.1)}$$

where N and A are the number and area of avalanches respectively, and b is a constant with a value $b \sim 1$.

Although the concept of self-organized criticality was first proposed to describe the complexity of the "sand pile" model, it is also associated with several natural hazards, (e.g., earthquakes, landslides and wildfires) (Bak 1996). For earthquakes, the slow movement of the tectonic plates, over hundreds to thousands of years, leads to stress accumulation. Therefore, stress is relieved in earthquakes satisfying a power-law (Gutenberg-Richter)

relation (Malamud and Turcotte, 1999). A power law distribution refers to the fact that larger size events are less frequent, while smaller size events are more frequent. A general Gutenberg-Richter relation is as follows:

$$LogN = -bm + c \qquad \textbf{(1.2)}$$

where, N and m are numbers and magnitude of earthquakes, respectively, while, b and c are constant (Gutenberg and Richter, 1956). For landslides, slope instabilities develop slowly and are relieved in the landslides. The volume-frequency distribution of landslides is also well approximated by the power-law relation (Turcotte, 1999). The frequency-size distribution of complex natural phenomena display Gaussian or in some cases power-law (fractal) distribution. Studies show that earthquakes and landslides are statistically characterized by power-law distributions (Malamud and Turcotte, 1999).

1.1.1 Complexity of earthquake-triggered landslides

Coupling the two natural hazards, landslides and earthquakes, creates a complex system that is called an earthquake-triggered landslide. Earthquake-triggered landslides (ETLs) are destructive natural hazards but are poorly understood (Keefer, 1984). Earthquake-triggered landslides have caused several major disasters worldwide during the last hundred years (e.g., the 1949 Khait Earthquake, Tajikistan (Evans et al., 2009)). In many earthquakes, landslides have caused more damage than other earthquake-triggered secondary geohazards such as liquefaction and tsunamis (Kramer, 1996). In the 1964 Alaska earthquake (M9.2) almost 56% of the total damage cost was caused by earthquake-triggered landslides (Kramer, 1996, and the references therein). The first systematic investigation of the characteristics of ETLs

was carried out by Keefer (1984), who is generally regarded as the pioneer of this field of study. He compiled a selective database on ETLs worldwide for the period 1811 to 1980. Since 1984, a number of studies have been published on the subject of ETLs, and other work has extended Keefer's original database (Keefer, 1994, and 2002; Malamud et al., 2004; Rodriguez et al., 1999). Chapter 2 of this thesis follows in this tradition by updating the ETL database once again.

1.2 Research needs

In recent years, there has been an increasing interest in the study of earthquake-triggered landslides; however, much uncertainty still exists about the relationship between earthquake (seismic) and landslide (geological) parameters. Some high priority research needs are identified in the following paragraph.

More complete and updated earthquake-triggered landslide catalogues/inventories need to be compiled for better understanding of the linkages in this complex system. Wasowski et al. (2011) have highlighted the need for more complete and comprehensive seismic landslide inventories on a regular basis. Although there have been many studies on the subjects of earthquakes and landslides, the connection between these two complex systems is not well established (e.g., the relationship between earthquake parameters, site seismic effects, and landslide occurrence and behavior). Furthermore, Wasowski et al. (2011) emphasized the necessity for analysis of the behavior of ETLs and their associated slope failures that cause permanent slope deformations. In the modeling of catastrophic seismic landsides, higher levels of detail and accuracy in geotechnical characterization of slope material properties are urgently needed due to their influence on the reliability of analysis (Wasowski et al., 2011).

1.3 Objectives

The overall purpose of this thesis is to analyze and explain the behavior of earthquake-triggered landslides in relation to earthquake parameters on a global scale (Chapter 2) and at site scale (Chapter 3). Six specific research objectives were formulated in pursuit of this goal:

1) Present our compilation and analysis of two new worldwide databases of earthquake-triggered landslides for the period of 1900-2010 and landslide-triggering earthquakes from 1998 to 2009;

2) Review and re-examine the relationships between landslide characteristics and earthquake parameters and compare the results with those of previous studies;

3) Investigate and explain the effects of earthquake parameters on the occurrence of earthquake-triggered landslides;

4) Review the geological setting of the Nahanni region (N.W.T., Canada) and the characteristics of the 1985 Nahanni earthquakes and the associated North Nahanni earthquake-triggered rockslide;

5) Define a method to estimate the October 1985 Nahanni earthquake ground motion response spectra at the site of the North Nahanni rockslide, based on the available strong motion data from the second Nahanni earthquake of December 23, 1985;

6) Analyze the static and seismic stability of the North Nahanni rock slope using UDEC (Universal Distinct Element Code).

1.4 Structure of the thesis

This first chapter introduces the complexity of earthquake-triggered landslides and highlights the most pressing needs of ETL research. It also gives an overview of the specific objectives

of the thesis. Chapters 2 and 3 are written as standalone papers. Chapter 2 addresses the first three objectives that are mentioned in Section 1.2 and presents a comprehensive documentation and analysis of earthquake-triggered landslides and landslide-triggering earthquakes on a global scale. This chapter specially examines the relationship between the occurrence of ETLs and earthquake parameters. The last three objectives of the thesis are addressed in Chapter 3. In this chapter, a detailed analysis of the 1985 North Nahanni earthquake-triggered landslide is carried out for the first time. The North Nahanni rockslide, with an estimated volume of 7.6 Mm^3, occurred in an uninhabited region (62.27 N, 124.17 W) of the Mackenzie Mountains, Northwest Territories, Canada, and was triggered by the Nahanni October 5th, 1985 earthquake (M_w=6.6). The North Nahanni rockslide is one of the largest historical landslides in the eastern part of the Canadian Cordillera. This chapter deals with the geological setting of the rockslide site as well as the geometry of the slope. It also presents the geological and seismological properties of the Nahanni earthquakes, and provides detailed geologic data on the 1985 North Nahanni rock mass (e.g., rock type, structure, nature and spacing of fractures) to evaluate the stability of the rock slope using a numerical model, the distinct element UDEC code (Itasca Consulting Group Inc. 2011). Finally, discussion and conclusions are presented in Chapter 4.

Chapter 2

Occurrence of earthquake-triggered landslides

2.1 Introduction

Earthquake-triggered landslides have caused significant damage in recent history (Kramer, 1996). In some cases, the impacts of ETLs on human social and economic activity have been greater than those of other secondary events (Utsu, 2002; Kramer, 1996). For example, as noted in Chapter 1, in the 1964 Alaska earthquake (M9.2), almost 56% of the total damage cost was caused by earthquake-triggered landslides (Kramer, 1996). The 1949 Khait Earthquake (M7.4) triggered hundreds of landslides in a mountainous region of central Tajikistan. Evans et al. (2009) estimated that a total of 7200 people were killed by earthquake-triggered landslides in the epicentral region of this earthquake (Evans et al., 2009). Kobayashi (1981) showed that, more than half of all deaths in large earthquakes (M≥7) in Japan during the period of 1964 to 1980 were caused by landslides. The 2008 M7.9 Wenchuan earthquake, triggered several thousand landslides; based on Sichuan Bureau of Land and Resources data (Cui et al. 2011), about 20,000 deaths were caused by landslides and rock avalanches which is about one third of total fatalities (Cui et al. 2011). The Daguangbao rockslide (Figure 2. 1) was the largest landslide (volume of 750 Mm^3) triggered by the 2008 M7.9 Wenchuan Earthquake, Sichuan, China (Chigira et al. 2010).

This chapter provides a comprehensive analysis of earthquake-triggered landslides on a global scale.

2.1.1 Previous work

The first serious investigations and analyses of earthquake-triggered landslides emerged in 1984. Keefer (1984) studied the general characteristics of earthquake-triggered landslides using data from 40 selected historical earthquakes that occurred between 1811 and 1980.The landslides were classified into 14 different types, and the total numbers of landslides of each type were determined for each earthquake. In his analysis of the relationships between characteristics of landslides and earthquake parameters, Keefer (1984, 2002) found that the number of earthquake-triggered landslides increases with increasing earthquake magnitude. However, we extended this study by considering recent data from 1998 to 2009 (Figure 2.7). The results show, not only that moderate-sized earthquakes can produce large numbers of landslides, as contended by Keefer (2002), but also, that large-sized earthquakes can induce only a few landslides, which does not support Keefer's findings (details are given in section 2.3.2).

Although Keefer (1984) has carried out an extensive analysis of earthquake-triggered landslides, his selective study did not take into account some of the major earthquakes which have triggered significant landslides (e.g., 1911 Tajikistan; 1929 New Zealand; 1933 China; 1941 Taiwan; and 1946 Peru). The findings would have been more convincing if Keefer (1984) had considered a wider range of data.

Rodriguez et al. (1999) extended the work of Keefer (1984) on earthquake-triggered landslides. A new database of earthquake-triggered landslide was compiled for the period of 1980 to 1997. The correlations between landslide characteristics and earthquake parameters were investigated using the new database (Rodriguez et al., 1999). The results were generally

similar to the findings by Keefer (1984); however, the presence of outliers was observed in some of the correlations (Rodriguez et al., 1999, page 325).

Malamud et al. (2004) considered the probability densities for three substantially complete landslide inventories: landslides in the Umbria region (Italy), triggered by rapid snowmelt in January 1997; landslides triggered by the 1994 M6.7 Northridge California earthquake; landslides in Guatemala, triggered by heavy rainfall from Hurricane Mitch in late October and early November 1998. Based on their observations among these three sets of probability densities, they suggested a general probability distribution for landslide occurrence during a landslide-generating event (Malamud et al., 2004).

The general landslide distribution proposed by Malamud et al. (2004) has been used to quantify the total volume, the maximum landslide areas and volumes associated with each landslide-generating event. Malamud et al. (2004) described that a landslide event may include a single or many thousands of landslides, associated with a trigger such as an earthquake, a heavy rain, or a volcanic eruption. Malamud et al. (2004) also proposed a magnitude scale, m_L, for a landslide-generating event based on the logarithm of the total number of landslides triggered by the event (Malamud et.al, 2004). The obtained results were combined with an empirical magnitude-volume equation proposed by Keefer (1994) (Keefer's data with additional Northridge earthquake data were used in their analysis) to quantify the area and the volume of the largest earthquake-triggered landslide as a function of earthquake magnitude. In section 2.5.2, we re-examine the assertion made by Malamud et al. (2004), using a new database for the period 1998-2009.

2.1.2 Objectives

Our global study of earthquake-triggered landslide occurrence has three objectives: 1) to report on the analysis of our two worldwide databases of earthquake-triggered landslides for the period of 1900-2010 and landslide-triggering earthquakes from 1998 to 2009, 2) to review and re-examine the relationships between landslide characteristics and earthquake parameters from our new databases and then compare the results with previous work done by Keefer (1984, 2002) and Malamud et al. (2004), 3) to investigate the effects of earthquake parameters on the occurrence and characteristics of earthquake-triggered landslides.

2.2 Database I: Compilation

A database containing 137 landslide-triggering earthquakes worldwide, with magnitudes greater than the minimum observed threshold for causing landslides (M4.5), was compiled for the period of 1998 -2009. This time period leads on, from the work of Rodriguez et al. (1999), who examined the period of 1980-1997. Our data sources include a comprehensive review of the existing literature on earthquake-triggered landslides, and a USGS-based earthquake catalog "PAGER-CAT" (http://earthquake.usgs.gov/research/data/pager/), which contains information on earthquake-induced secondary events (Allen et al. 2009).

2.3 Database analysis, Part I

The comparison between the numbers of landslide-triggering earthquakes and total numbers of earthquakes (n=68733*)* during the period 1998 to 2009 shows that only a very small percentage of earthquakes caused landslides. Our study shows that only 0.2 % (137 out of 68733) of earthquakes, with $M \geq 4.5$, triggered significant landslides, and only 4.5 % (84 out

of 1844) of earthquakes of $M \geq 6$ resulted in earthquake-triggered landslides (Figure 2. 2 and Table 2.1). Later in this chapter, we demonstrate that almost 50 % of huge landslides are earthquake-induced.

It is important to investigate the conditions under which earthquakes cause landslides. Figure 2.3 shows the global distribution map of the 137 landslide-triggering earthquakes (1998-2009). The highest percentage of these 137 earthquakes occurred in Asia (60 %) following by south and Central America (13.5 %); more information is given in Table 2.2. The global seismic hazard map (GSHM) is used as the base map for landslide-triggering earthquake distribution (Giardini et al., 1999) in Figure 2.3. The global seismic hazard map shows the peak ground acceleration (PGA) that a site can expect with the probability of 10 % in 50 years. The color scale represents the PGA ranges from very low (0-0.2 m/s^2) in White to very high (4-5 m/s^2) in Red-Brown. The distribution of landslide-triggering earthquakes on the GSHM indicates that in general, there is a higher probability of ETL occurrence in regions with higher expected PGA.

Table 2.1: The cumulative percentage of landside-triggering earthquakes (LTE) with respect to the total number of earthquakes within different ranges of magnitudes (1998 – 2009)

Earthquake magnitude range	Number of earthquakes	Number of LTE	% of LTE
M ≥ 4.5	68733	137	0.2
M ≥ 5	19432	130	0.7
M ≥ 6	1844	84	4.5
4.5≤ M <5	49301	6	0.01
5≤ M <6	17588	46	0.26
6≤ M <7	1670	51	3.1
7≤ M <8	160	27	16.9
8≤ M <9	13	5	38.5
M ≥ 9	1	1	100

Earthquakes in the compiled database are classified into the three sets of catalogs based on an estimate of the number of landslides that occurred during each earthquake. The first catalog (Class A) contains 14 earthquakes, each having a moment magnitude (M) within the range of 6.2-8.5 and each having caused at least 250 landslides. More detailed information is given in Table 2.3. Moment magnitude (M) was introduced by Hanks and Kanamori in 1979 and is defined as follows:

$$\mathrm{M} = \frac{2}{3}\log(M_0) - 10.7 \qquad \textbf{(2.1)}$$

where M_0 is seismic moment, which is a quantity related to the area of the fault and the average amount of slip over the fault plane (Hanks and Kanamori, 1979).

The second catalog (Class B) includes 13 earthquakes ranging in moment magnitude between 5.0 and 8.0. Earthquakes in the Class B catalog triggered single or only a few small-scale landslides. Finally, the third catalog (Class C) contains those landslide-triggering earthquakes in which there is no information available on the numbers and characteristics of their corresponding landslides (the lists of earthquakes in class B and C catalogs are given in Appendix A). In this chapter, we analyze the geological and seismological characteristics of significant landslides and their triggering earthquakes from the Class A catalog.

Table 2.2: Worldwide distribution of 137 landslide-triggering earthquakes (LTE) (1998-2009)

Continent	Number of LTE out of 137	% of LTE
Asia	82	60
Central & South America	19	13.8
AUS and Oceania	12	8.7
Europe	12	8.7
North America	7	5.1
Africa	5	3.6

2.3.1 Earthquake characteristics

Earthquake source parameters were obtained from PAGER-CAT and the U.S. National Earthquake Information Center (NEIC) catalogs (USGS-based earthquake catalogs, http://earthquake.usgs.gov/earthquakes/eqarchives/epic/) for landslide-triggering earthquake events during the period of 1998-2008 and 2008-2009, respectively. Table 2.3 contains information on epicentral location, magnitude and depth of each landslide-triggering earthquake (Class A) as well as the source fault types. The values of the moment magnitude (M) within the Class A database range from 6.2 to 8.5, and we note that all the earthquakes are shallow (focal depth <80 km) (Figure 2.4). The source fault types are classified into three categories: normal, thrust and strike-slip. A histogram of the source fault types is given in

Figure 2.5. Interestingly, 64.3 % of the landslide-triggering earthquakes were associated with thrust faulting (magnitude rage of 6.6 to 8.4), while 21.4 % and 14.3% ruptured along the strike-slip (having magnitude range of 6.2 to 7.9) and normal faults (magnitudes of 6.9 and 7.7), respectively. The magnitude-frequency curves for landslide-triggering earthquakes and total number of earthquakes with $M \geq 6$ during 1998-2009 are plotted in Figure 2.6. This figure shows that the Magnitude-frequency curves of LTEs and all earthquakes have a same trend for $M \geq 7.5$, however the slope of the LTE curve decreases for earthquake magnitude less than 7.5. One possible argument for this change might be that our catalog (LTE) is not complete for earthquake magnitude less than 7.5, although earthquake magnitude range of 6-7.5 is expected to be less affected by data incompleteness in our catalog. Beside this, another explanation could be that the physical processes involved in triggering a landslide are divided into two regimes based on magnitude of earthquakes in which for magnitude higher than 7.5 the LTE magnitude-frequency curve follows the general Gutenberg-Richter distribution.

Table 2.3: List of Landslide-triggering earthquakes (Class A), 1998-2009

Number	Earthquake	Country	Date	Latitude	Longitude	Mw	Depth (km)	Fault Type	Number of landslides	References
1	Chichi	Taiwan	20/09/1999	23.77 N	120.98 E	7.6	33	Inland thrust fault	Ten thousand	Chen et al., 2004
2	El Salvador	El Salvador	13/01/2001	13.05 N	88.66 W	7.7	60	Offshore, Normal fault	More than 500	Jibson et al., 2004
3	El Salvador	El Salvador	13/02/2001	13.67 N	88.94 W	6.5	10	Strike-Slip Fault	Hundreds	Jibson et al., 2004
4	Southern Peru	Peru	23/06/2001	16.26 S	73.64 W	8.4	33	Thrust fault	Hundreds	Keefer and Moseley, 2004
5	Denali Fault	Alaska	03/11/2002	63.52 N	147.44 W	7.9	4	Strike-slip fault	Thousands	Jibson et al., 2006
6	Tecomán	Mexico	22/01/2003	18.77 N	104.10 W	7.5	24	Thrust fault	Several thousand	Keefer et al., 2006
7	Fiordland	New Zealand	21/08/2003	45.10 S	167.14 E	7.2	28	Thrust fault	Several hundreds	Hancox et al., 2003
8	Mid Niigata	Japan	23/10/2004	37.23 N	138.78 E	6.6	16	Reverse fault	More than 1000	Chigira and Yagi, 2006
9	Kashmir	Pakistan	08/10/200 5	34.54 N	73.59 E	7.6	26	Thrust fault	Several thousand	Owen et al., 2008
10	Solomon Islands	Solomon Islands	01/04/2007	8.466 S	157.04 E	8.1	24	Thrust fault	Thousands	McAdoo et al., 2008
11	Aysén Fjord	Chile	21/04/2007	45.24 S	72.65 W	6.2	36	Strike-slip fault	Hundreds	Sepulveda et al., 2010
12	Wenchuan	China	12/05/2008	31.00 N	103.32 E	7.9	19	Thrust fault	More than 15,000	Sato and Harp, 2009. Yin et al.,
13	Iwate-Miyagi Nairiku	Japan	13/06/2008	39.03 N	140.88 E	6.9	7	Normal fault	More than 4000	Yagi et al., 2009
14	Padang, west Sumatra	Indonesia	30/09/2009	0.72 S	99.87 E	7.5	81	Oblique-thrust fault	Thousand	Rosyidi et al., 2011

2.3.2 Landslide characteristics

Ten landslide-triggering earthquakes have been selected from the Class A database, based on the availability of information on the characteristics of their corresponding landslides, to investigate the types of landslides associated with each earthquake. We classified landslides into five different types: rock falls, rockslides, rock avalanches, debris slides, and debris flows. Table 2.4 shows that the most dominant types of earthquake-triggered landslides are rock falls and rock slides.

In contrast to the previous results obtained by Keefer (1984, 2002) who found a positive correlation between the total number of triggered landslides and earthquake magnitude, Rodriguez et al. (1999) demonstrated that the total number of landslides is not dependent on an earthquake's magnitude. We re-examined the relationship between the total number of triggered landslides and earthquake magnitude using our database from Table 2.3 (Figure 2.7). Our observation agrees with that of Rodriguez et al. (1999), who showed that the total number of landslides cannot be expressed as a function of earthquake magnitude.

Table 2.4: Types of E-T landslides, 1998-2009

Earthqua	Country	Date	Magnitu	Rock falls	Rock slides	Rock avalanches	Debris Slides	Debris flows
Chichi	Taiwan	20/09/19	7.7		×	×	×	
El	El Salvador	13/01/20	7.7	×	×		×	×
El	El Salvador	13/02/20	6.6	×	×		×	×
Denali	Alaska	03/11/20	7.9	×	×	×		
Tecomán	Mexico	22/01/20	7.6	×	×			
Fiordland	New Zealand	21/08/20	7.2	×			×	×
Mid	Japan	23/10/20	6.6			×		
Kashmir	Pakistan	08/10/20	7.6	×	×			
Wenchuan	China	12/05/20	7.9	×		×		×
Iwate–	Japan	13/06/20	6.9				×	×

2.4 Database II compilation

A database of 37 landslides, with initial failure volumes greater than 20 Mm^3that occurred worldwide between 1900 and 2010, has been compiled. The database contains large-scale earthquake-triggered (n=18) and non-earthquake-triggered landslides (n=20) (ETL and NETL respectively), (Evans, unpublished data).The data are listed in Tables 2.5 and 2.6.

Table 2.5: Characteristics of large-scale (volume ≥ 20 Mm^3) earthquake-triggered landslides during the period 1900-2010 (ETL) (Evans, unpublished data)

Number	Locality	Country	Latitude	Longitude	M	Year	Volume(Mm^3)
1	Usoy	Tajikistan	38 16 26 N	72 36 11 E	7	1911	2000
2	Dongban chauythtt, Sichaun	China	31 38 11 N	104 07 39 E	8	2008	750
3	Bairaman	Papua New Guinea	05 35 12 S	151 12 46 E	7.1	1985	180
4	Diexi	China	32 02 25 N	103 40 29 E	7.4	1933	150
5	Tsao-Ling 4	Taiwan	23 34 35 N	120 40 19 E	7.6	1999	126
6	Hattian Bala	Pakistan	34 08 22 N	73 43 51 E	7.6	2005	85
7	Tsao-Ling 1	Taiwan	23 34 35 N	120 40 19 E	7.1	1941	84
8	Khait	Tajikistan	39 11 25 N	70 55 44 E	7.4	1949	60
9	Falling Mountain	New Zealand	42 53 47 S	171 40 59 E	7.1	1929	57
10	Chiu-Fen-Erh-Shan	Taiwan	23 57 27 N	120 50 36 E	7.6	1999	42
11	Rio Llama Ancash	Peru	08 24 22 S	77 34 39 W	7.3	1946	36.5
12	Mount Ontake	Japan	35 52 25 N	137 29 14 E	6.8	1984	36
13	Lituya Bay	Alaska USA	58 40 32 N	137 29 17 W	7.7	1958	30
14	Madison Canyon	USA	44 49 44 N	111 25 39 W	7.3	1959	30
15	Schwan	Alaska USA	60 52 43 N	145 10 46 W	9.2	1964	27
16	Allen 4	Alaska USA	60 47 15 N	144 54 57 W	9.2	1964	23
17	Steller 1	Alaska USA	60 34 58 N	143 17 31 W	9.2	1964	20
18	North McGinnis Peak	Alaska USA	63 34 04 N	146 15 11 W	7.9	2002	20

Table 2.6: Characteristics of large (volume ≥ 20 Mm^3) non earthquake-triggered landslides during the period 1900-2010 (NETL) (Evans, unpublished data)

Number	Locality	Country	Latitude	Longitude	Year	Volume(Mm^3)
1	Kaiaput	Papua New Guinea	06 07 02 S	146 18 03 E	1988	1300
2	Mayunmarca	Peru	12 36 55 S	74 39 25 W	1974	1000
3	Pufu Ravine, Luquan County, Yunnan	China	26 10 35 N	102 37 49 E	1965	450
4	Vajont	Italy	46 15 46 N	12 20 28 E	1963	292
5	Hiedayama	Japan	36 46 56 N	137 51 06 E	1911	150
6	Tsao-Ling 2	Taiwan	23 34 35 N	120 40 19 E	1942	100
7	Paatuut	Greenland	70 16 34 N	52 44 21 W	2000	90
8	Yigong	China	30 10 58 N	94 55 53E	2000	75
9	Mount Steele	Canada	61 06 42 N	140 18 08 W	2007	75
10	Ok Tedi Mine (Vancouver Ridge)	Papua New Guinea	05 13 04 S	141 08 35 E	1989	70
11	Tanggudong	China	29 24 46 N	101 07 06 E	1967	68
12	Mount Steller	Alaska USA	60 30 44 N	143 05 31 W	2005	50
13	Hope	Canada	49 18 14 N	121 14 51 W	1965	47
14	Gros Ventre	USA	43 37 55 N	110 32 47 W	1925	40
15	Valtellina	Italy	46 22 55 N	10 21 24 E	1987	35
16	Sale Mountain	China	35 33 49 N	103 35 07 E	1983	30
17	Frank	Canada	49 35 08 N	114 24 10 W	1903	30
18	Tsao-Ling 3	Taiwan	23 34 35 N	120 40 19 E	1979	26
19	La Josefina	Ecuador	02 51 08 S	78 50 44 W	1993	23
20	Costantino	Italy	38 08 48 N	16 00 19 E	1973	20

2.5 Data analysis, Part II

2.5.1 ETL frequency-volume distributions

The database (Tables 2.5 and 2.6) of the largest ETL and NETL that have occurred worldwide since 1900 has been studied. Figure 2.8 plots the annual cumulative volume-frequency distributions of ETLs versus NETLs. The magnitude-frequency curves have been fitted with power-law equations, and their respective slopes and intercepts are almost equal, as can be seen in the following equations ($R^2 = 0.97$ for both curves)

$$logN_1 = -0.650logV_1 + 0.05 \quad \textbf{(2.2)}$$

$$logN_2 = -0.669logV_2 + 0.17 \quad \textbf{(2.3)}$$

where N_1 and N_2 are the numbers of ETLs and NETLs respectively and V is corresponding volume. Figure 2.8 suggests that the type of triggering event (e.g., earthquake, rain storm) is not changing the general dependence of frequency of landslides on their volume.

Following our observation from Figure 2.8, we also derived a landslide distribution map for very large ($V \geq 20$ Mm^3) earthquake and non earthquake-triggered landslides (Figure 2.9). This map indicates that the large-scale ETLs and NETLs distributions during the period 1900-2010 are almost concentrated in the same regions. Therefore, we suggest that, these huge landslides occurred in areas, which are generally prone to landslides, and landslide-prone slopes need a minimum amount of external force to fail. That required external force could be obtained by any type of triggering event (earthquake, heavy rainfall, volcanic activity or other sources); however, we should emphasize that the amplitude of external

forces exert a powerful effect upon the characteristics of the associated landslides (e.g., volume, area, types).

2.5.2 Correlation between the volume of largest ETLs and earthquake magnitudes (1900-2010)

Malamud et al. (2004) proposed an analytical relationship between the maximum earthquake-triggered landslide volume (V_{Lmax}) and earthquake magnitude (Equation 2.4) by combining an empirical equation derived by Keefer (1994) and the general earthquake-triggered landslide distribution discussed in Section 2.1.2 above.

$$logV_{Lmax} = 1.36M - 11.58\ (\pm 0.49) \qquad \textbf{(2.4)}$$

We investigated the relationship between the volume of the largest ETLs and their corresponding earthquake magnitudes for the period of 1900 to 2010. Figure 2.10 compares the result from our database with the empirical equation (equation 2.4) suggested by Malamud et al. (2004). Contrary to their proposed equation, our data shows that the volume of the largest landslide triggered by a given earthquake is not a simple function of earthquake magnitude. In the next section, we explore the idea that earthquake peak ground motions (i.e., PGA, PGV) could be a potential earthquake parameter to replace earthquake magnitude to correlate with ETL volumes.

2.5.3 Volume of ETL and PGA, PGV, PSA

We calculated peak ground acceleration (PGA), peak ground velocity (PGV), and 5%-damped pseudo-absolute-acceleration spectra (PSA) at frequencies of 1 Hz, 5 Hz, and 10 Hz from the 18 landslide-triggering earthquakes at the location of their corresponding largest earthquake-triggered landslides (Table 2.7). We used ground motion prediction equations developed by Boore and Atkinson (2008) to obtain the average horizontal component of ground motions as a function of earthquake magnitude and distance from the epicenter to the site of the landslides (Equation 2. 5). The following procedure was performed to obtain the results.

The equation 2.5 is the general form of ground motion prediction by Boore and Atkinson (2008):

$$\ln(Y) = F_M(M) + F_D\left(R_{JB}, M\right) + F_S\left(V_{S30}, R_{JB}, M\right) + \varepsilon\sigma_T \qquad \textbf{(2.5)}$$

where F_M and F_D are the magnitude scaling and distance function, respectively and F_S represents site amplification. M is moment magnitude, R_{JB} is the Joyner-Boore distance which is defined as the closest distance to the surface projection of the fault (R_{JB} is approximated to be equal to the epicentral distance in our calculation) and V_{S30} is the average shear-wave velocity from the surface to a depth of 30 m and the last term ($\varepsilon\sigma_T$) is the square root of the overall variance of the regression (Boore and Atkinson 2008).

The magnitude scaling is given by:

for $M \leq M_h$

$$F_M(M) = e_1 U + e_2 SS + e_3 NS + e_4 RS + e_5 (M - M_h) + e_6 (M - M_h)^2 \quad \textbf{(2.6a)}$$

and for $M \geq M_h$

$$F_M(M) = e_1 U + e_2 SS + e_3 NS + e_4 RS + e_7 (M - M_h) \quad \textbf{(2.7b)}$$

where *U*, *SS*, *NS*, and *RS* are dummy variables which stand for unspecified, strike-slip, normal-slip, and reverse-slip fault type, respectively, and M_h, the "hinge magnitude", is a coefficient for the shape of the magnitude scaling. All the values are given in Boore and Atkinson (2008, Table 7, page 120).

The distance function is given by:

$$F_D(R_{JB}, M) = [C_1 + C_2 (M - M_{ref})] \ln \left(\frac{R}{R_{ref}}\right) + C_3 (R - R_{ref}) \quad \textbf{(2.8)}$$

$$R = \sqrt{{R_{JB}}^2 + h^2} \quad \textbf{(2.9)}$$

where c_1, c_2, c_3, M_{ref}, R_{ref}, and h are the coefficients, that were determined in Boore and Atkinson (2008, Table 6, page 119).

The site amplification is divided into linear (F_{LIN}) and nonlinear (F_{NL}) parts (Equation: 2.10), the mathematical description of each term can be found in Boore and Atkinson (2008, pages 107-109).

$$F_C = F_{LIN} + F_{NL} \quad \textbf{(2.10)}$$

The calculated PGAs, PGVs and PSAs at three frequencies are plotted against the volume of the ETLs, below a threshold of ca. 80 Mm^3 (n=11) in the range of 20-80 Mm^3. In Figures 2.11 and 2.12 there is a clear trend of increasing landslide volume with increasing PGA, PSA, and PGV. Figure 2.11 shows that data values have a similar distribution in all the four

plots and have an average of R^2= 0.64 for PGA and PSAs, and R^2= 0.75 for PGV. These findings are consistent with Meunier et al.'s (2007) findings, which showed the rate of slope failure is proportional to the PGA or PGV caused by an earthquake. However, our results also indicate that huge ETLs with volumes greater than 80 Mm^3 are independent of the calculated PGA, PGV, and PSA at different periods at the site of landslides.

Table 2.7: Calculated peak ground motions from the 18 landslide-triggering earthquakes at the location of their corresponding largest earthquake-triggered landslides, 1900-2010.

Year	Country	M	Volume (Mm^3)	Distance (m)	PGA (g)	PSA @1HZ (g)	PSA @5HZ (g)	PSA @10HZ (g)	PGV (cm/s)
1911	Tajikistan	7	2000	19.1	0.33	0.32	0.87	0.61	39.81
2008	China	8	750	103.93	0.10	0.13	0.20	0.16	22.16
1985	Papua New Guinea	7.1	180	18.61	0.34	0.33	0.89	0.63	43.37
1933	China	7.4	150	5.07	0.62	0.67	1.80	1.25	109.43
1999	Taiwan	7.6	126	38	0.24	0.23	0.55	0.42	37.09
2005	Pakistan	7.6	85	46.18	0.21	0.21	0.47	0.36	32.39
1941	Taiwan	7.1	84	26.24	0.28	0.27	0.70	0.50	34.40
1949	Tajikistan	7.4	60	11.1	0.45	0.46	1.22	0.88	71.74
1929	New Zealand	7.1	57	13.53	0.40	0.40	1.08	0.77	53.28
1999	Taiwan	7.6	42	24.9	0.31	0.30	0.75	0.57	48.97
1946	Peru	7.3	36.5	24.31	0.30	0.29	0.75	0.55	41.45
1984	Japan	6.8	36	9.27	0.47	0.49	1.32	0.92	55.49
1958	Alaska USA	7.7	30	67.58	0.15	0.16	0.32	0.25	26.05
1959	USA	7.3	30	21.23	0.33	0.32	0.82	0.60	45.31
1964	Alaska USA	9.2	27	139.17	0.10	0.15	0.15	0.15	30.46
1964	Alaska USA	9.2	23	155.6	0.08	0.14	0.12	0.12	27.58
1964	Alaska USA	9.2	20	243.9	0.03	0.09	0.04	0.04	17.18
2002	Alaska USA	7.9	20	59.9	0.18	0.19	0.38	0.30	32.24

2.6 Conclusions

This chapter presented a comprehensive study of worldwide earthquake-triggered landslides using our compiled databases. First, we described the compilation of landslide-triggering

earthquake catalog. In addition, we compiled a database of catastrophic landslides, involving initial failure volumes of greater than 20 Mm^3. The results of the data analyses are summarized below.

Our observations suggest a geological dichotomy: although a very small percentage of earthquakes cause landslides (4.5 % for $M \geq 6$), almost 50% of the large-scale catastrophic landslides ($V \geq 20$ Mm^3) in the period 1900-2010 were triggered by earthquakes. Analysis of the earthquake-triggered landslides from 1998 to 2009 showed that the total number of earthquake-triggered landslides during or after an earthquake cannot be expressed as a function of the earthquake magnitude. Our observation also indicated that the most dominant types of ETLs are rock fall and rockslide and more than 60 % of the landslide-triggered earthquakes occurred as a result of seismic events along thrust faults.

We found that the volume of the largest landslide triggered by a given LTE is not a simple function of earthquake magnitude (a source characteristic); however, the volume of huge landslides below a threshold of ca. 80 Mm^3 in the range of 20-80 Mm^3 has a good correlation with calculated earthquake peak ground motions at the site of the triggered landslides. This result is consistent with Meunier et al.'s (2007) findings, which showed the rate of slope failure is proportional to the peak ground acceleration (PGA) or peak ground velocity (PGV) caused by an earthquake. Very large ETLs (volume greater than 80 Mm^3) result from complex progressive failure mechanisms initiated by seismic shaking, i.e., above this threshold volume, landslide volume is independent of PGA, PGV and PSA. This suggests that, other factors are also required to cause a massive bedrock landslide, suggesting other special conditions are required for large earthquake-triggered landslides to occur.

Lastly, the magnitude and frequency curves of huge ETLs and non-ETLs for events during the period 1900-2010 are almost identical in slope and intercept; these observations showed that the type of triggering event does not change the general dependence of frequency of landslides on their volume.

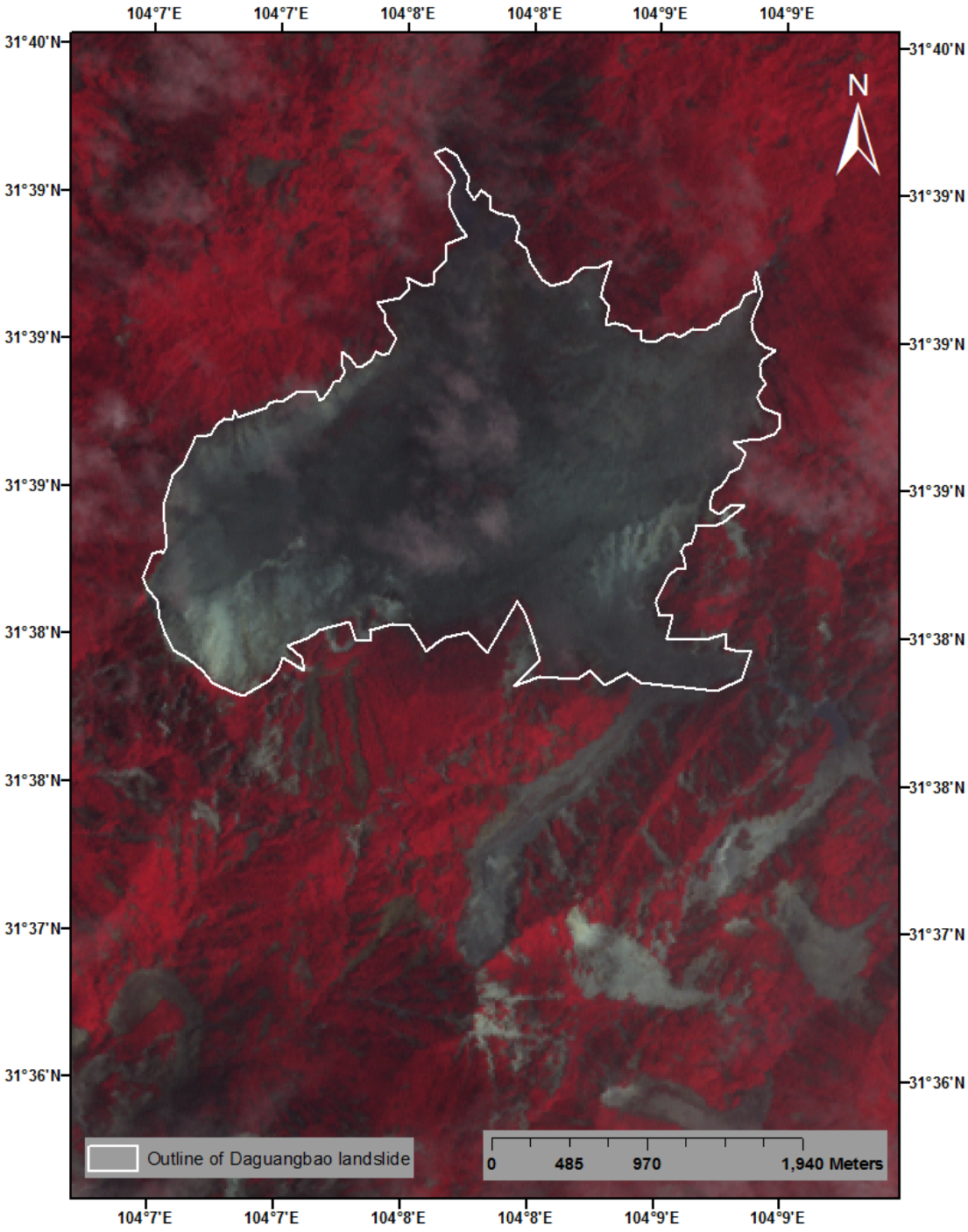

Figure 2.1: Daguangbao landslide area on an ASTER image taken on May 30, 2008

The landslide was triggered by the M7.9 Wenchuan earthquake on May, 12, 2008.

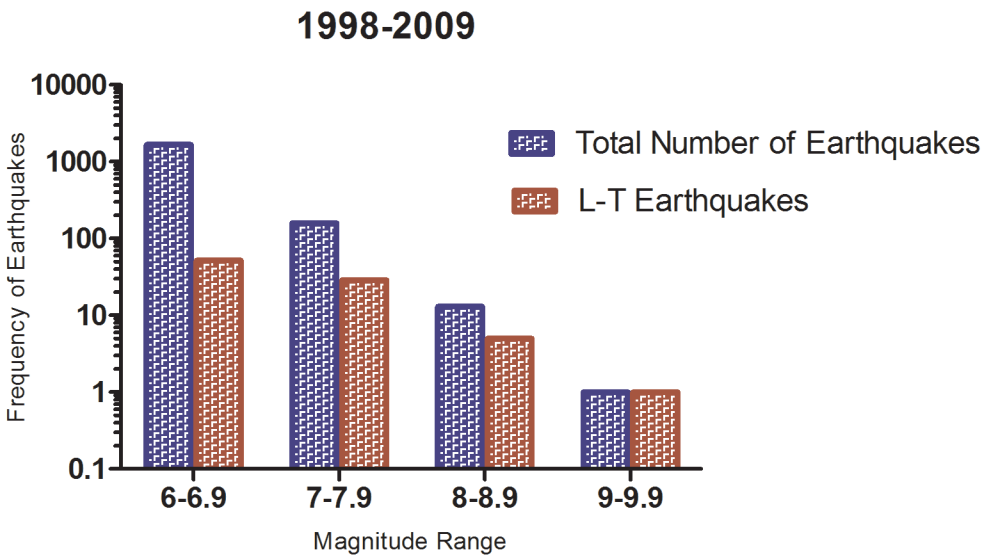

Figure 2.2: The histogram of landslide-triggering earthquakes (n= 137) frequency and total number of earthquakes (n= 68733) within different range of magnitudes from 1998 to 2009

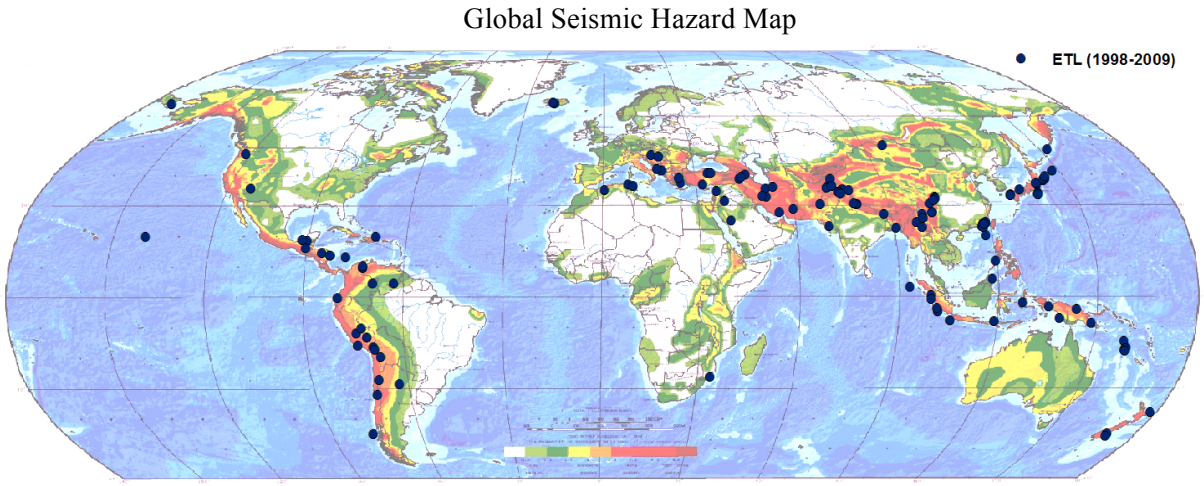

Figure 2.3: Landslide-triggering earthquakes (n=137) distribution map (1998-2009). Global seismic hazard map used as the base map (Giardini et al., 1999)

The global seismic hazard map shows the peak ground acceleration (PGA) that a site can expect with the probability of 10 % in 50 years. The colors represent the PGA ranges from very low of 0-0.2 m/s^2 (White) to very high of 4-5 m/s^2 (Red-Brown).

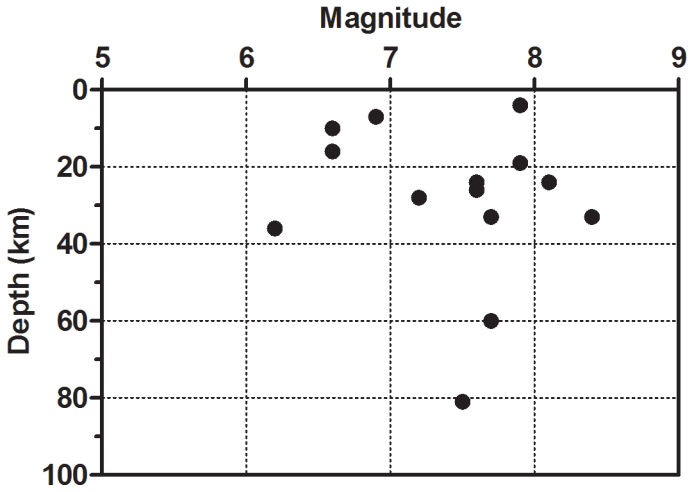

Figure 2.4: Depths of Class A landslide-triggering earthquakes (n=14). All are considered as shallow earthquakes (depth < 80 km) (1998-2009)

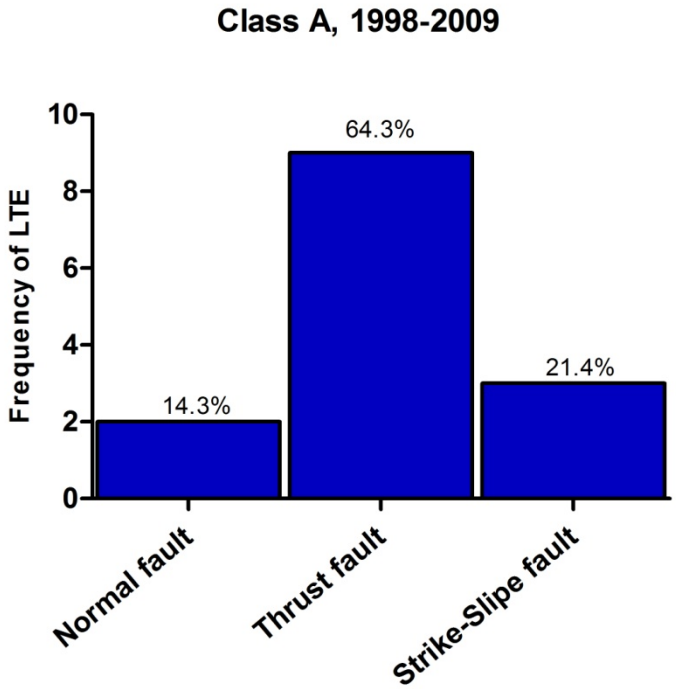

Figure 2.5: Histogram showing source fault types for the earthquakes from the Class A database (1998-2009)

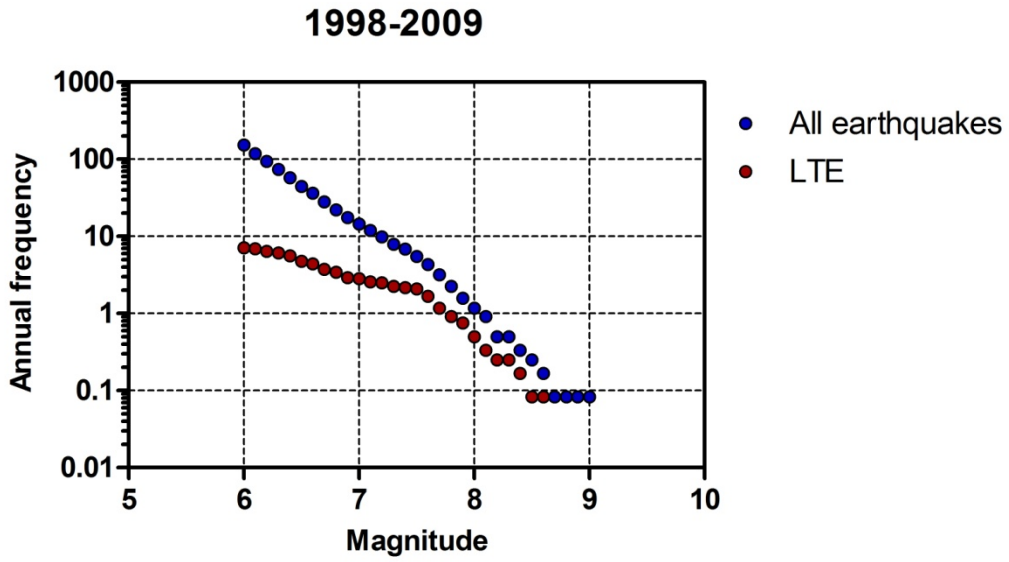

Figure 2.6: Annual cumulative magnitude-frequency distribution of landslide-triggering earthquakes (Red; n=84) and total number of earthquakes (Blue; n=1844) for M≥ 6 for the period of 1998-2009

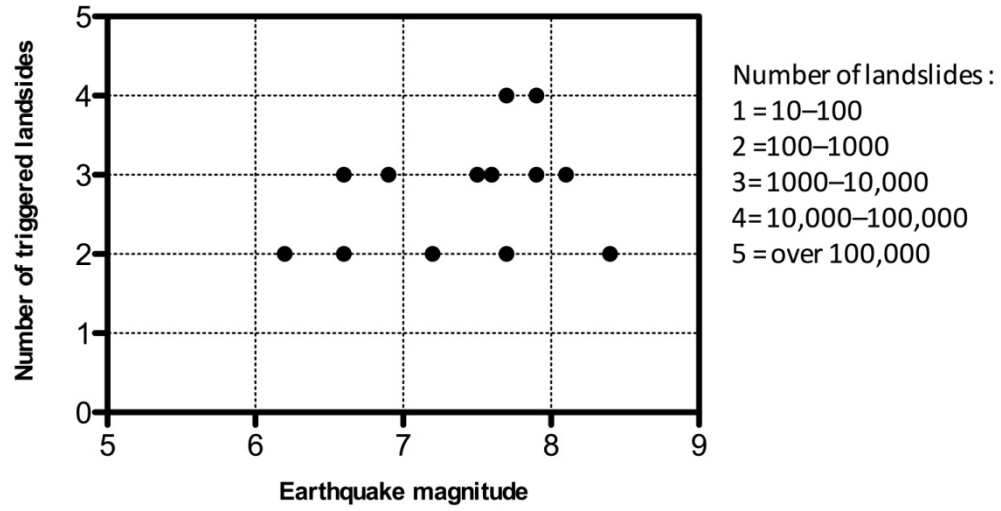

Figure 2.7: Relation between total numbers of reported earthquake-triggered landslides and earthquake magnitude for earthquakes from Table 2.3.

Numbers of reported earthquake-triggered landslides are not precisely known for all earthquakes in our database; therefore, an order of magnitude scale is used in this plot.

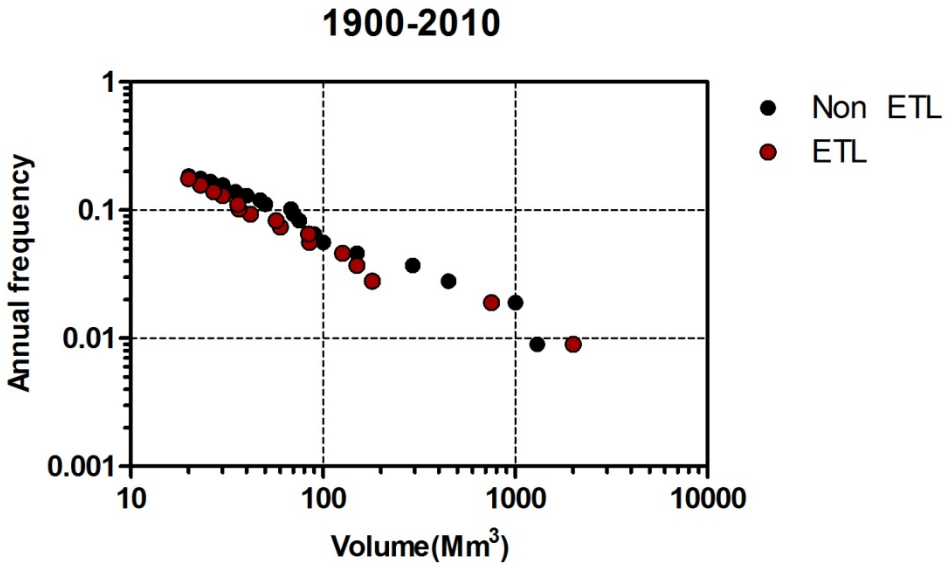

Figure 2.8: Annual cumulative magnitude-frequency distribution of large-scale earthquake (ETL) (volume ≥ 20 Mm^3; n=18) and non-earthquake-triggered landslides (NETL) (volume ≥ 20 Mm^3; n=20) for the period 1900-2009. Magnitude is expressed as landslide volume (Evans and Ghahramani, unpublished data)

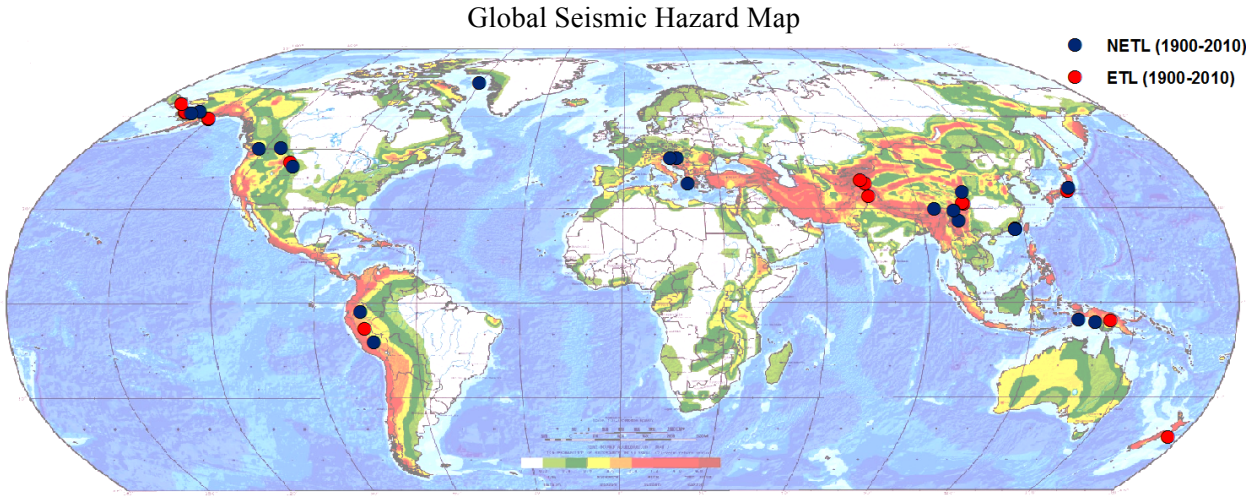

Figure 2.9: Map of large-scale landslides (volume ≥ 20 Mm^3) that occurred during the period 1900-2010. Dark blue and pink dots represent non-earthquake-triggered and earthquake-triggered landslides, respectively. Global seismic hazard map used as the base map (Giardini et al., 1999)

The global seismic hazard map shows the peak ground acceleration (PGA) that a site can expect with the probability of 10 % in 50 years. The colors represent the PGA ranges from very low of 0-0.2 m/s^2 (White) to very high of 4-5 m/s^2 (Red-Brown).

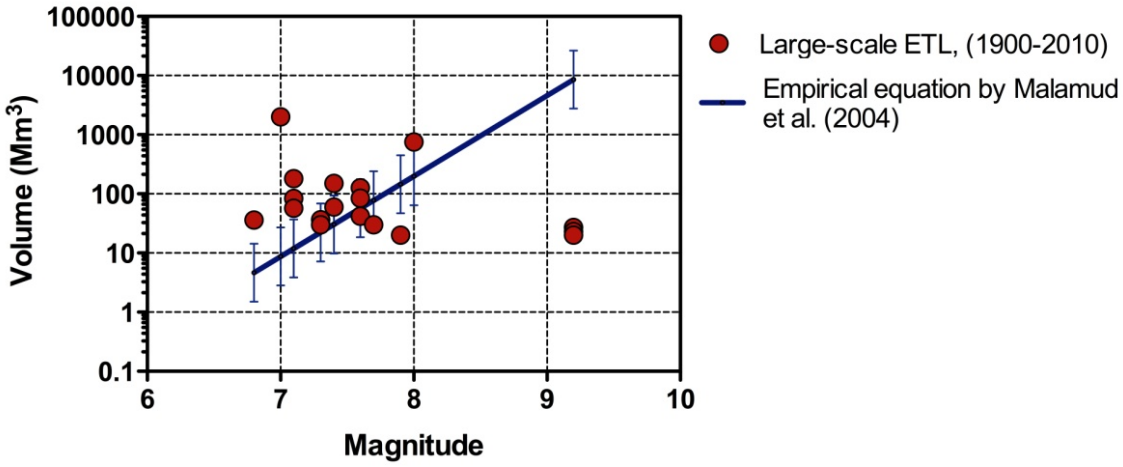

Figure 2.10: Volume of the largest earthquake-triggered landslides (n=18) from 1900 to 2010 versus moment magnitude of the earthquakes (Red) and Malamud et al. (2004) V-M empirical equation (Equation 2.4), considering 0.45 Error bars (Blue)

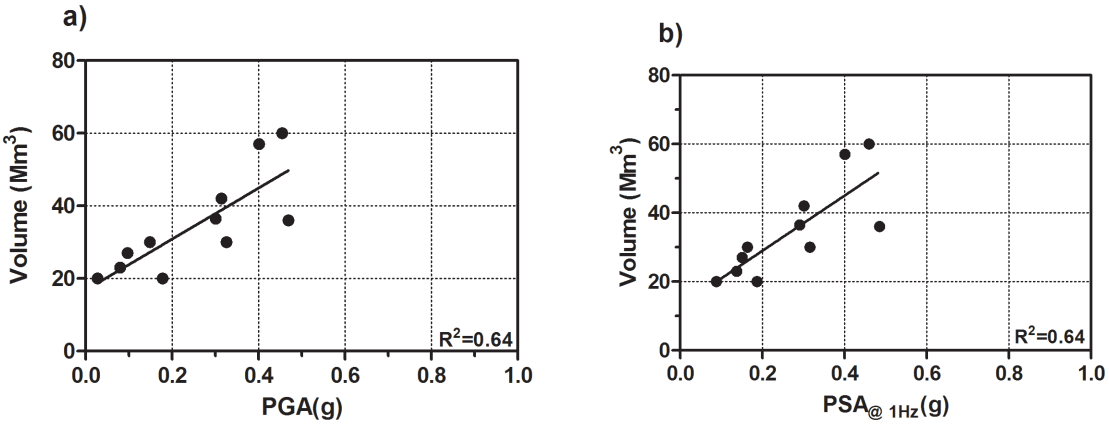

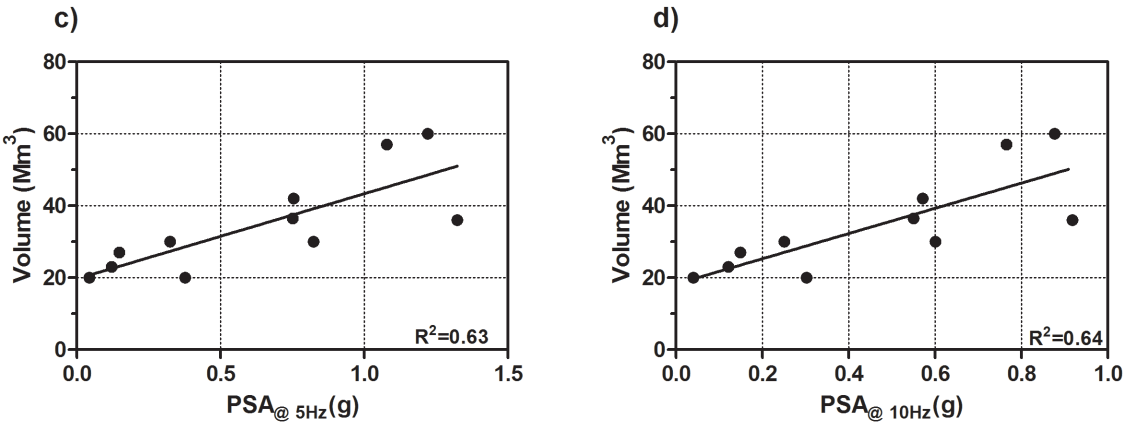

Figure 2.11: The relationship between the volume of the large-scale earthquake-triggered landslides, within the volume range of 20-80 Mm^3, and earthquake PGA (a) and earthquake acceleration response spectra (PSA) (b, c, and d) for the period of 1900-2010

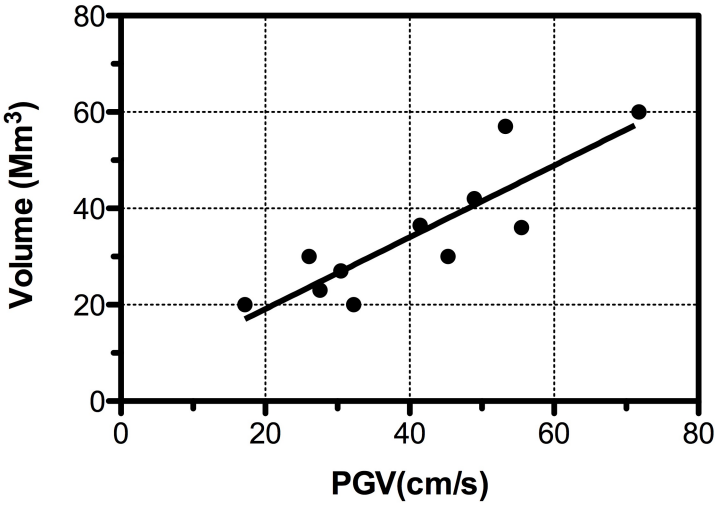

Figure 2.12: The relationship between the volume of the large-scale earthquake-triggered landslides, within the volume range of 20-80 Mm^3, and earthquake peak ground velocity (PGV) (R^2=0.75), 1900-2010.

Chapter 3

The 1985 Nahanni earthquakes and the associated North Nahanni rockslide, N.W.T., Canada

3.1 Introduction

The 1985 North Nahanni rockslide, (volume ~7.6 Mm^3), occurred at 62.27°N and 124.17°W in an uninhabited region of the foothills of the Mackenzie Mountains, Northwest Territories, Canada (Figure 3.1). The landslide was triggered by the M_w=6.6 October 5th, 1985 earthquake (Evans et al., 1987; Wetmiller et al., 1988). The epicenter of the earthquake (62.19^{o}N, 124.24^{o}W) was approximately 10 km south- southwest of the landslide and had a focal depth of almost 6 km (Wetmiller et al., 1988). A second larger earthquake occurred on December 23, 1985, at almost the same location (62.19° N, 124.24° W), with magnitude M=6.8 (Figure 3.2). Although the magnitude of the second earthquake was larger than the first one, it triggered no landslides of the same scale as the North Nahanni rockslide. This case history is of interest for two reasons: 1) we have very detailed geological data from the landslide as well as strong motion records from the second earthquake, and 2) since the 1985 North Nahanni landslide occurred in an uninhabited area, we can study the physics of this complex natural phenomenon without any influence from human activities.

No comprehensive study has been done to analyze the behaviour of the 1985 North Nahanni rockslide in relation to earthquake parameters. Also, the stability of the slide has not been quantitatively analysed and the sliding mechanism of the rock mass during the earthquake shaking is still not well understood. In this chapter, we provide a numerical

analysis of the stability of the failed slope before, and during the earthquake using UDEC (Universal Distinct Element Code, Itasca Consulting Group Inc. 2011). UDEC is a numerical modeling code, based on the distinct element technique, for advanced geotechnical analysis of rock, soil, and structural support in two dimensions.

3.1.1 Previous work

The 1985 Nahanni seismic events are the largest ever recorded in the eastern part of the Canadian Cordillera, and several investigations were conducted after the two large Nahanni earthquakes and the North Nahanni rockslide (Evans et al., 1987; Weichert et al., 1986; Wetmiller et al., 1988; Choy and Boatwright, 1988).

The characteristics of the earthquakes and their source parameters were determined by Wetmiller et al. (1988), who also carried out a study of aftershock sequences and implications for seismic hazard in the same paper (Wetmiller et al., 1988). Weichert et al. (1986) installed three temporary accelerographs in the vicinity of the epicenter immediately after the October 5th earthquake, so they were in situ for the December 23rd event. Characteristics of the second earthquake (e.g., epicenter, focal depth) were calculated from the observed seismograms (Weichert et al., 1986). Choy and Boatwright (1988) analyzed teleseismic P waves generated by the 1985 Nahanni earthquakes in time and frequency domains. The time domain analysis resulted in the determination of the depth, focal mechanism, and source complexity of earthquakes, while the frequency domain analysis was used to estimate the acceleration source spectrum for the largest Nahanni earthquake (December 23). Choy and Boatwright (1988) determined that the results of the teleseismic

analysis are in a good agreement with the results from the analysis of the aftershock and the strong motion records by Wetmiller et al. (1988), and Weichert et al. (1986) . The study also indicated that the stress release in both main shocks exhibited an extreme complexity of rupture processes (Choy and Boatwright, 1988). Boore and Atkinson (1989) calculated P wave spectral ratios for all earthquakes during the year 1985 with an additional 1988 earthquake, using many recorded data from the Western Canada Telemetry Network (WCTN), the Eastern Canada Telemetry Network (ECTN), and the Global Digital Seismographic Network (GDSN). Boore and Atkinson (1989) also obtained source acceleration spectra for all the 1985 Nahanni earthquakes by combing the calculated spectral ratios with the source acceleration spectrum of the largest event estimated by Choy and Boatwright (1988).

The North Nahanni rockslide was studied by Evans et al. (1987) and Hu and Evans (1993). Evans et al. (1987) estimated the volume of the landslide to be approximately 5-7 million m^3; later, the volume was recalculated by Hu and Evans (1993) as 7.6 Mm^3. The field investigations at the rockslide included a detailed study of the structural geology, in particular, the sliding surface which followed a thrust fault, measurement of the surface roughness of the sliding surface, and slope geometry determination before and after the slide (Evans et al., 1987).

Conventional methods for computing slope stability during seismic activity may be divided into three main classes:1) pseudostatic analysis, 2) permanent-displacement analysis, and 3) stress-deformation analysis. Each method has its strengths and weaknesses, and can be appropriately applied in different situations (Jibson 2011).

The seismic stability of slopes was initially analyzed in the early 1920s by a pseudostatic approach and the paper by Terzhagi (1950) is the first documentation of this method in the technical literature. In this model, the effect of earthquake force is added to the static limit-equilibrium analysis by considering pseudostatic acceleration components, which produce inertial forces. Limit-equilibrium analysis simply considers the force equilibrium equation for a rigid body of soil or rock above a potential failure surface. In the pseudostatic approach, the average effects of vertical forces tend to be very small; thus, only the horizontal component of earthquake shaking is usually considered (Jibson, 2011). Newmark (1965) proposed the permanent-displacement method, using any ground motion acceleration data in order to compute finite displacement of a slope in a non-equilibrium state. Newmark's method addressed some of the simplistic assumptions of pseudostatic analysis, and due to its simplicity was used extensively to estimate seismic-induced slope displacement. Clough and Chopra (1966) used the finite-element method to perform stress-deformation analysis using the stress-strain behavior of rocks and soil. The stress-deformation technique for slope stability can predict the pattern's amplitude of stresses and mass movements during and after deposition. Before widespread computer use and the rise of numerical modeling, this type of analysis was very complex and computationally hard. However, with advancements in computing efficiency, this method soon began to be applied to slopes, in particular, earth dams, and it provided a modeling tool for the static and dynamic deformation of soil systems. Based on developments in stress-deformation analysis a whole family of analytical methods has been produced, including finite difference, distinct element, and discrete element modeling (Jibson, 2011).

Numerical modeling provides a new approach to compute the real dynamic interaction between material, site geometry and wave propagation (e.g., Havenith et al., 2003). Numerical rock slope stability techniques are divided into three main categories: 1) the continuum model; 2) the discontinuum model and 3) the hybrid approach (Eberhardt et al., 2004) . Continuum approaches used in slope stability analysis include the finite element method (FEM) and finite difference method (FDM). Due to the rapid development of computing power, both are very often used in slope stability analysis. Some examples are as follow, stability estimation of the Rosone landslide in the western Alps computed with FEM (Forlati et al., 2001); back-analysis of the Frank slide (Canada) with FDM (FLAC) by Benko and Stead (1998).

Discontinuum methods (e.g., the distinct element method, the discontinuous deformation analysis, and the particle flow codes) divide the problem into a discrete number of blocks, which are interacting with each other and at the same time are subject to external forces and move as a function of time. In the discrete element method, the algorithm is based on a force-displacement law specifying the interaction between deformable intact rock blocks and a law of motion, which determines displacements induced in the blocks by non zero net forces (Eberhardt et al., 2004).

Discontinuities such as faults, joints and bedding planes control the behavior of a rock mass since a rock mass is not a continuum. The presence of discontinuities has an extreme influence on the stability of rock slopes, and the behavior of these features has a critical role in stability evaluation. Although continuum codes have been extremely useful for the analysis of rock slopes that consist of massive intact rock and soil-like rock masses, they are

not appropriate for slopes controlled by discontinuity behavior (Bhasin and Kaynia, 2004). The discrete element method (DEM) is especially designed to solve discontinuity problems (Cundall, 1987). In the DEM, a rock mass is represented as an assemblage of discrete blocks, and joints as interfaces between blocks (Itasca Consulting Group Inc. 2011). Several studies have investigated the stability of rock slopes using discontinuum modeling methods. For example, Bhasin and Kaynia (2004) analyzed the stability of a rock slope in western Norway, using UDEC code (Itasca Consulting Group Inc. 2011); Benko and Stead (1998) have used the finite difference and distinct element techniques to re-examine failure mechanisms involved in the Frank slide.

In this study, the distinct element UDEC code has been used to analyze the stability of the North Nahanni rock mass before (static analysis) and during (dynamic analysis) the earthquake shaking.

3.1.2 Objectives

A comprehensive study has been done to investigate the Nahanni landscape's response to the 1985 earthquakes. We analyzed the behaviour of the 1985 North Nahanni earthquake-triggered landslide in relation to the earthquake parameters as a case study. In this chapter, we first review and describe the geological setting of the Nahanni rockslide. Second, the details of the characteristics of the rockslide are given followed by the characteristics of the October and December 1985 earthquakes. We then define a method to calculate the October 1985 earthquake acceleration response spectra at the site of the rockslide, based on the available strong motion data from the second earthquake on the 23rd of December, 1985.

Finally, a discontinuum numerical modeling technique (UDEC) is used to calculate the static and seismic stability of the rock slope prior to and during the first main shock.

3.2 The 1985 North Nahanni rockslide

3.2.1 Geological setting

The rockslide occurred in the Middle Devonian Nahanni Formation from a northeast side of the northwest-trending anticlinal ridge (Hu and Evans, 1993; Douglas and Norris, 1976). The ridge has peak elevations of approximately 1070 m above sea level (height of 543.21 m) and it is located along the axis of the English Chief Anticline. The rockslide involved massively-bedded fine-grained crystalline limestone (Evans et al., 1987).

3.2.2 Structural geology

The sliding surface followed the surface of a thrust fault developed partly along bedding and partly across bedding (Evans et al., 1987). The discontinuities around the slide from the outcrops are divided into several structural domains (Figure 3.3) and the mean orientations of discontinuities in each structural domain are summarized in Table 3.1, 3.2, and 3.3 (McMartin and Evans, 1994).

Table 3.1: Orientation of Bedding Planes (Hu and Evans, 1993)

Domain	Dip direction	Dip angle
1	019	21
2	042	35
3	061	17
4	031	20

The thrust fault which outcrops in the upper part of the failure surface is striking almost parallel to the bedding plane but is dipping almost 15^{o} steeper than the bedding (Figures 3.4, and 3.9). The contact between the fault plane and the bedding plane on the failure surface is very smooth and gradual. Each domain contains several joint sets which are listed in Table 3.3. The strike joint sets and dip joint sets are dominant joint sets at most of the outcrops (Hu and Evans, 1993; McMartin and Evans, 1994). For the present study all structural measurements were plotted on a lower hemisphere of an equal area stereographic projection using the software DIPS (Figures 3.5, and 3.6).

Table 3.2: Structural domains of the fault around the North Nahanni rockslide (Hu and Evans, 1993)

Description of each domain is as follows, FP: East part of the failure surface across bedding, the measurements were taken from the lower part where the fault surface gradually changes to dipping at 20°. The overall dip is 35° measured from the topographic map (1:5000), F: West part of the failure surface across bedding, FG: Fault surface recognized in gully north of the slide and north of the Domain 3 of bedding, FPF: FP and F together. The Table has been reproduced from Hu and Evans (1993).

Domain	Dip direction	Dip angle
FP	032	28
F	038	37
FG	044	35
FPF	034	31
All domains together	037	32

Table 3.3: Major joint sets and their orientation (Hu and Evans, 1993)

Domain	Joint set (dipdir/dip)
1	a - 130/87 b - 221/69 c - 175/80
2	a - 316/85 b - 223/58
3	a - 308/82 b - 215/65 c - 175/84
4	048/90*

3.2.3 Slope geometry

The rockslide detached from the NE flank of the NW-SE trending English Chief Anticline (Appendix B). The axis of this anticline is about 1 km west of the rockslide (Evans et al. 1987). The movement of the sliding rock masses has exposed part of the sliding surface, while the front (lower) part was buried under the sliding debris. Field observations indicated the existence of large blocks of limestone in the debris directly below the detachment zone including an intact rock slab with an area of approximately 0.5 ha (Evans et al., 1987). The displaced rock mass moved down the bedding dip and was deposited in the valley floor below the depletion zone. A small portion of the deposited debris travelled 1 km beyond the toe of the slope, in the direction of the valley slope (Evans et al., 1987; Hu and Evans, 1993) (Figure 3.3).

As noted in Section 3.1.1, Evans et al. (1987) estimated the volume of the rockslide to be of the order of 5-7 Mm^3. Hu and Evans (1993) carried out a later recalculation in which the total volume of the rockslide was 7.6 M m^3. The volume overlying the lower sliding surface was $5.8x10^6$ m^3 (76 % of the total volume), while that overlying the upper sliding surface was $1.8x10^6$ m^3 which is 24 % of the total volume (Hu and Evans, 1993).

We have created pre- and post-slide digital elevation models (DEMs) from large scale topographic maps (1:1000) using GIS (Geographic Information System) (Figures 3.7, and 3.8). The 0.5 m resolution digital elevation models were utilized in order to construct slope profiles. As can be seen in Figure 3.9, the sliding surface consists of two planar elements. The lower part dips at 20° and is parallel to bedding, and the upper part dips at 35° and cut across bedding (Figure 3.9). The upper part of the sliding surface intersects the ground surface near the top of the ridge. The lateral scarp, which follows the combination of joint sets and is 45°-50° from the dip direction of the bedding, separates the sliding mass from the remaining rock mass on the southeast side of the rockslide (Hu and Evans, 1993). We also used a change detection technique in GIS to quantify topographic changes resulting from the rockslide (Figure 3.10). The elevation change map shows that maximum deposition of rock mass took place at an elevation of approximately 750 m (Figure 3.10).

3.2.4 Frictional properties of the sliding surface

The exact value of the friction angle and cohesion along the sliding surface before the October 1985 event is not known. Hu and Evans (1993) conducted tilting table tests on two samples taken from the sliding surface after the slide, following the procedure described by

Bruce et al. (1989) to determine the friction angles of rock surfaces. They repeated the test five times for both samples. The sliding angles (φ_s) were found to be 25.0°±1.4° and 21.3°±1.9°, represented by means and standard deviations. The lower value, 21.3°, may represent the lower bound of the friction angle of the sliding surface. The lateral scarp follows the combination of steeply dipping joint sets. The dip directions of the strike joints and dip joints are 90° or greater from the sliding direction (Figures 3.5 and 3.6), so it is reasonable to assume that the lateral frictional resistance against sliding was negligible.

3.3 The 1985 North Nahanni earthquakes

The two relatively large Nahanni earthquakes occurred in the Mackenzie District of the Northwest Territories, Canada in 1985 (Figure 3.12). These events occurred in the zone of low seismic activity of Mackenzie Mountain, where no historical seismicity of this magnitude had been reported (Basham et al., 1985; Weichert et al., 1986). Earthquakes from 1961 to 2012 for M≥ 3 within the circular area of 300 kilometers radius around the 1985 Nahanni main shocks, has been selected from NEIC and NEDB (National Earthquake Database, http://earthquakescanada.nrcan.gc.ca/stndon/NEDB-BNDS/bull-eng.php) catalogs. The magnitude-frequency curve for the earthquakes is plotted in Figure 3.11. The magnitude-frequency curve has been fitted with the power-law equation:

$$\log(N) = 4.17 - 0.93M \qquad \textbf{(3.1)}$$

Where N is annual frequency and M is earthquake magnitude. Therefore, the return period of the October 1985 Nahanni earthquake (magnitude 6.6) is almost one in 100 years.

The largest historical earthquakes that occurred in the Eastern Canadian Cordillera are listed in Table 3.4 (Wetmiller et al., 1988).

Table 3.4: Large historical earthquakes in the Eastern Canadian Cordillera (Wetmiller et al., 1988).

Date	Latitude	Longitude	Ms
04 /02/ 1918	52.28°	-118.37°	6.0
29/05/1940	66.88°	-135.5°	6.2
05/06/1940	66.91°	-134.9°	6.5
01/03/1955	65.30°	-132.80°	6.6
05/10/1985	62.19°	-124.24°	6.6
23/12/1985	62.19°	-124.24°	6.9

3.3.1 Characteristics of the 1985 Nahanni earthquakes

The first large earthquake, with a moment magnitude of 6.6 occurred on 5 October 1985. Its epicenter was located at 62.19° N, 124.24° W, and the focal depth was 6.0 km (Wetmiller et al., 1988). The second main earthquake with a moment magnitude (M) of 6.8 occurred on 23 December 1985 at nearly the same location (Table 3.5). The second large earthquake epicenter and focal depth were calculated by Weichert et al. (1986) based on the information from the recorded strong motion data (Evans et al., 1987; Wetmiller et al., 1988; Weichert et al., 1986). Detailed information related to the two earthquakes is given in Table 3.5.

The area affected by the earthquakes was estimated using Modified Mercalli (MM) intensities based on the only available information from inhabited areas. The measured affected area for the October event is estimated to be 1.5 million km^2 (Wetmiller et al., 1988).

Table 3.5: Characteristics of the two 1985 Nahanni earthquakes (Wetmiller et al., 1988)

Earthquake parameters	October 5th	December 23th
Epicenter	61.19°N, 124.24°W	61.19°N, 124.24°W
Focal depth	6 km	6 km
Magnitude	6.6	6.8
Strike	N175°E	N175°E
Dip	34°W	25°W
Rake	90 °	90 °
Length	25 km	25 km
Width	15 km	15 km
Stress drop	33 bars	50 bars
Moment	10^{26} dyne-cm	1.5×10^{26} dyne-cm
Felt area	1.5 million km^2	>1.5 million km^2
Area MM IV	0.8 million km^2	1.2 million km^2

3.3.2 Fault Geometry

According to Wetmiller et al. (1988) the focal mechanisms of the main shocks are as follows. The main shock ruptures had a rake of 90° (thrust fault) and a strike of N175°E. The measured dips were 34° and 25° to the west for the October and December events, respectively (Table 3.5). Their study suggested the possibility of co-planar listric fault planes. The two earthquakes and their aftershocks reveal the presence of a pre-existing blind fault that may possibly be associated with the English Chief Anticline. However, no evidence of a surface rupture break was found during field studies (Wetmiller et al., 1988).

3.4 The October 1985 earthquake acceleration response spectra and velocity estimation at the site of the North Nahanni rockslide

3.4.1 Methodology

After the first main shock in October, three accelerographs were deployed near the earthquake epicenter (Weichert et al., 1986), as shown in Figure 3.12. The strong motion data of the second main event on December 23 were recorded by these three accelerographs. Using strong motion data from the second main event at Station 2, the closest seismograph to the 1985 North Nahanni rock landslide, we have estimated the velocity spectra and acceleration response spectra of the first large earthquake at the site of the rockslide. Basic assumptions used in our estimation are as follows; the two earthquakes had the same location, and Station 2 is assumed to have been located at the site of the North Nahanni rockslide. Station 2 was deployed at the elevation of 914m (http://www.earthquakescanada .nrcan.gc.ca/stnsdata/nwfa/ev/sm/Nahanni_1985-86/), which is close to the level of the highest elevation of the rock mass detachment zone (almost 950 m.a.s.l). Therefore, the same topographic conditions are considered in our calculation. Our procedures are described in the following sections. Figures 3.13 and 3.14 show the horizontal acceleration and velocity time histories of the December main shock which were recorded at Station 2.

3.4.2 Computed spectral ratios

Boore and Atkinson (1989) calculated spectral ratios of moderate-to-large earthquakes that occurred in part of the District of Mackenzie, Northwest Territories, Canada during the year 1985 with an additional event in 1988, relative to the spectrum of the largest event

(December 23, 1985) (Boore and Atkinson, 1989). Spectral ratio (SR) is described by Chael (1987). Recorded data from a seismograph can be expressed as the convolution of its source time function $S(t)$, propagation path effects $E(t)$, site effect (background noise) $N(t)$, and the seismic instrument response $I(t)$ in the time domain (Chael, 1987).

$$X(t) = [S(t) * E(t) + N(t)] * I(t) \qquad \textbf{(3.2)}$$

where $X(t)$ is an observed seismogram and $*$ represents convolution. However, in the frequency domain, the convolution becomes point-wise multiplication:

$$X(\omega) = [S(\omega) \cdot E(\omega) \cdot I(\omega)] + [N(\omega) \cdot I(\omega)] \qquad \textbf{(3.3)}$$

The background noise is assumed to be uncorrelated with the signal; therefore, the energy spectrum is given by

$$|X(\omega)|^2 = |S(\omega) \cdot E(\omega) \cdot I(\omega)|^2 + |N(\omega) \cdot I(\omega)|^2 \qquad \textbf{(3.4)}$$

$E(\omega)$ is approximated to be the same function for all events due to the fact that the distances between source locations are small compared to the distance between each source and the receiver. $I(\omega)$, the response of the instrument to any signal, is also considered to be the same (Chael, 1987). The noise term ($\left|N(\omega).I(\omega)\right|^2$) can be subtracted from $\left|X(\omega)\right|^2$ to obtain the

noise-corrected energy spectrum. As a result, the ratio of the noise-corrected energy spectra (SR), for any two earthquakes recorded at a fixed station, is equal to the ratio of their source spectra (Chael, 1987; Aki, 1967).

$$SR = \left|\frac{X_2(\omega)}{X_1(\omega)}\right|^2 + \left|\frac{S_2(\omega)}{S_1(\omega)}\right|^2 \qquad \textbf{(3.5)}$$

Boore and Atkinson (1989) used recorded data from The Western Canada Telemetred Network (WCTN) at regional distances, and the Eastern Canada Telemetry Network (ECTN) and the Global Digital Seismographic Network (GDSN) at teleseismic distances. The spectral ratios were calculated for the event of October 5, 1985, relative to those of the largest event (December 23, 1985). Note that the computed spectral ratios are for P waves. The square root of spectral ratios for the frequencies of 0.5, 1.0, 5.0, and 10.0 Hz were extracted from Figure 5 in Boore and Atkinson (1989). The results are given in Table 3.6. The averaged spectral ratios (Table 3.6) are used in Equation 3.6 to calculate ground motion spectra of the 1985 October earthquake at the site of the North Nahanni rockslide.

Table 3.6: Spectral ratios over individual stations within a specific range of frequencies for the 1985 Nahanni earthquakes.

The ratios were calculated by dividing the square root of the October event's energy spectrum by the December event's energy spectrum (Boore and Atkinson, 1989)

Station	0.5Hz	1Hz	5Hz	10Hz
GDSN	1.148	1.202	1.479	1.38
WCTN	0.933	1.259	1.259	1.51
ECTN	1.259	1.096	0.912	---
AVG of all	1.10	1.18	1.19	1.45

3.4.3 Velocity and acceleration response spectra (PSA)

The acceleration response spectra for the December 23 earthquake were calculated from the available recorded acceleration data at Station 2 (Figure 3.13), using a FORTRAN code developed by Nigam et al. (1968). The importance of the response spectra approach in the designing and analyzing of engineering structures has been well illustrated since the 1940s (Nigam and Jennings, 1968). The response spectra were first introduced by Biot (1941) and Housner (1941). The acceleration response spectrum is defined to be the maximum acceleration of a single degree of freedom oscillator when subjected to ground motion. We used the strong motion data of the December Nahanni earthquake from an open source file of the Natural Resource Canada website (http://earthquakescanada.nrcan.gc.ca//stnsdata/ nwfa/ev/sm/Nahanni_1985-86/). A FORTRAN computer program (Nigam and Jennings, 1968) is used to calculate 5%-damped PSA from the instrumental data for periods between 0.1 s to 2.0 s. The list of PSA values, for December main shock and at different frequencies, is given in Table 3.7.

Recorded horizontal velocity time histories of the Nahanni December earthquake at Station 2 are shown in Figure 3.14. We computed the Fourier velocity spectra from these available strong motion data and selected the velocity amplitudes of frequencies at 0.5, 1, 5, and 10 Hz for further analysis (Table 3.10).

All obtained values (Table 3.7, and 3.10) are used in Section 3.4.4 to estimate velocity and acceleration response spectra of the October main shock.

Table 3.7: Acceleration response spectra for the December 23, 1985 Nahanni earthquake

PSA_{Dec} (g)	PSA (g) for *f*= 0.5Hz	PSA (g) for *f*= 1Hz	PSA(g) for *f*= 5Hz	PSA (g) for *f*= 10Hz
PSA240°	0.08	0.13	0.41	0.64
PSA330°	0.11	0.28	0.53	0.55
AVG PSA	0.095	0.21	0.47	0.595

3.4.4 Calculations and results

The October 1985 earthquake ground motion at the site of the landslide were obtained using the following estimation,

$$X_{Oct} = (\frac{D_2}{D_1}) \cdot \sqrt{SR} \cdot X_{Dec} \qquad \textbf{(3.6)}$$

where $X(\omega)$ represents acceleration response spectra (PSA) or velocity spectra (V) and SR is the spectral ratio, both at specific frequencies. D_1 and D_2 are the closest distances from the location of the earthquake to the accelerograph station and the location of the North Nahanni rockslide, respectively. The ratio of $\frac{D2}{D1}$ is the distance correction factor.

In general, the closest distance has different definitions. Boore et al. (1997) expressed it as the closest distance to the surface projection of the rupture, while Abrahamson and Silva (1997) used the closest distance from the receiver to the rupture. In this case, the fault dimensions are large compared to the distances between the Station 2 and the North Nahanni rockslide. As suggested by Wetmiller et al. (1988), the fault shape is assumed to be

rectangular with the length and width of 25km and 15 km, respectively. Therefore, we assumed that the ratio of $\frac{D2}{D1}$ in Equation 3.6 is equal to one. We also calculated acceleration response spectra using epicenteral and hypocenteral distances (Tables 3.8, and 3.9). A List of calculated PSA_{Oct} and V_{Oct} at specific frequencies are given in Table 3.9 and Table 3.10. V_{Oct} values are used as seismic inputs for North Nahanni rock slope stability analysis in Section 3.5.4.

Table 3.8: Epicentral and Hypocentral distances from the earthquake location to the rockslide site and Station 2.

Distances to the location of earthquakes	Epicentral distance (km)	Hypocentral distance (km)
1985 North Nahanni Rock slide	9.42	11.17
Temporary Station 2	5.74	8.30

Table 3.9: Calculated acceleration response spectra for the October 5, 1985 Nahanni earthquake

Distance	PSA_{Oct} (g) for *f*= 0.5Hz	PSA_{Oct} (g) for *f*=1Hz	PSA_{Oct} (g) for *f*=5Hz	PSA_{Oct} (g) for *f*=10Hz
Epicenter	0.06	0.15	0.35	0.52
Hypocenter	0.08	0.18	0.43	0.64
$\frac{D2}{D1}$ =1	0.11	0.25	0.58	0.87

Table 3.10 Input velocities estimated for the October main shock at the site of Nahanni rockslide based on the strong motion data from second main shock (December, 1985).

Frequency (Hz)	$Velocity_{Oct}$ (m/s)	$Velocity_{Dec}$ (m/s)
0.5	0.201	0.143
1	0.098	0.083
5	0.012	0.01
10	0.004	0.003

3.5 Slope Stability analysis

In this part of the chapter, we provide an analysis of the static stability of the rock slope before the October earthquake, and a dynamic analysis of the movement of the sliding rock mass along the sliding surface during the October main shock.

A discontinuum numerical modeling study was undertaken using the UDEC Version 5.0 distinct element software (Itasca Consulting Group Inc. 2011). The distinct element technique is a powerful tool for modeling rock slope susceptibility to seismic events (e.g., earthquake and blasting). Distinct element codes are highly applicable to the modeling of discontinuity-controlled instabilities, and are capable of simulating large displacements due to slip or opening along discontinuities (Eberhardt et al., 2004). The most important advantages of distinct element techniques is that they enable a slope system to develop further than continuum methods (e.g., FEM, FDM) and allow singular blocks to deform separately (Havenith et al., 2003).

3.5.1 Modeling of the Nahanni rockslide in UDEC

We considered a rock mass model which contains bedding, fault, and a set of orthogonal joints. Initially a rectangular model with dimensions of 500 m by 500 m was considered. The numbers of joints in the model were reduced compared to those existing in the field and a spacing of 10 m for the orthogonal joint set and bedding plane was adopted. Figure 3.17 shows the jointed slope model used for numerical analysis. Although the spacing between the joints might be smaller in reality, spacing of 10 m is proposed to increase of efficiency of numerical simulation.

3.5.2 Input data of the rock mass

The rock mass around the rockslide area has been classified using the geomechanics RMR classification (Bieniawski, 1978), and the Geological Strength Index (GSI) System (Hoek 1994). The RMR of the rock mass was estimated at 74, a high RMR value that designates the rock mass as good quality rock. GSI values ranging between 70 and 75 were assigned to the rock mass using the original GSI chart by Hoek and Brown (1997), which is given in Appendix D. Cai et al. (2004) described a relationship between deformation modulus (E) and GSI. We have used the average estimated GSI value to estimate the elastic modulus of 30 GPa from the GSI-E plot given by Cai et al. (2004) (Figure 3.16). The bulk (K) and shear (G) modulus of the rock mass were calculated using the following relations (Itasca Consulting Group Inc. 2011):

$$K = \frac{E}{3(1-2\nu)} \qquad \textbf{(3.7)}$$

$$G = \frac{E}{2(1+\nu)} \qquad \textbf{(3.8)}$$

where the Poisson's ratio (ν) was estimated to be 0.28.

In the analysis, the Mohr-Coulomb failure criterion is assumed to apply along the sliding surface. The uniaxial compressive strengths of the limestone blocks are assumed to be 50 MPa (the lower limit) and 250 MPa (upper limit), and cohesion of sliding surface is assigned a value of zero, based on the assumption that sliding took place on a pre-sheared bedding plane and fault surface during the earthquake. Pore pressure is also assumed to be zero because dilation of rock masses can dissipate cleft water pressure on a well-drained slope immediately after a small amount of movement (Henkel, 1967). According to Hu and Evans (1993) the slope was well drained before the sliding event. Table 3.11, parts a, and b show the properties of the rock mass and joints used for the analysis.

Table 3.11: Distinct element parameters for the 1985 North Nahanni rockslide

a) Rock mass properties for the numerical modeling of the rockslide.

Rock Type	Limestone
Density	2600 kg/m^3
Elastic Modulus (Gpa)	30
Poisson's Ratio	0.28
Bulk Modulus (GPa)	22.7
Shear Modulus (GPa)	11.7
Friction angle	42^o
Cohesion (Mpa)	6.72

b) Discontinuity properties assumed for the UDEC simulations. jkn: normal contact rigidity, jks: tangential contact rigidity, Jfr_1: sliding surface friction angle, Jfr_2: friction angle of joints above sliding surface, $Cohesion_1$: sliding surface cohesion, and $Cohesion_2$: cohesion of joints above sliding surface.

Jkn (MPa)	10000
Jks (MPa)	1000
Jfr_1	21^o (lower limit) and 35^o (upper limit)
Jfr_2	35^o
$Cohesion_1$ (Mpa)	0
$Cohesion_2$(Mpa)	0.1

3.5.3 Static analysis

First, we estimated the impact of geological components on slope stability under static conditions. The manual-specified roller boundary conditions were applied along the bottom and sides of the model: displacement is not allowed in the x-direction along the y-axis, and movement at the base of the numerical model is not allowed in the y-direction (Itasca Consulting Group Inc. 2011). The stresses were assumed to vary linearly with depth, and at the bottom of the slope the horizontal and vertical stresses in the rock mass were estimated to be 12 MPa (density ≈ 2600 kg/cm^3, depth ≈ 450 m). A number of history points were monitored on the rock slope to observe its movement before the slope reached equilibrium (see Figure 3.17 for the location of these points). Figure 3.18 shows the shear displacements and the displacement vectors along the joints before the slope reached equilibrium at a friction angle of 24^o for sliding surface under static condition. The maximum displacement in the model before equilibrium under static conditions is about 12 cm. The plot of displacements along the monitored history points indicates that the slope is in equilibrium.

This stage is considered to represent the existing in situ stage where the rock mass conditions are observed to be stable prior to the earthquake.

Static factors of safety were determined for our basic model for a range of friction angles under static conditions. Sliding surface friction angles were selected in the range of 21^o to 35^o, based on the measured friction angle from the sliding surface taken after the slide (21^o to 25^o) (Hu and Evans, 1993). However, the slope was stable for friction angle values of 24^o or higher. The calculated factor of safety values for different friction angles are given in Table 3.12, the results show that the safety factor of this slope was very low under static conditions and was likely to fail under a weak seismic shaking.

Table 3.12: Factor of safety values under static conditions

Sliding surface friction angle	FOS
23^o	F<1
24^o	1.002
30^o	1.28
35^o	1.55

3.5.4 Dynamic analysis

The preceding numerical analysis showed that the North Nahanni slope was close to static instability before the October 1985 Nahanni earthquake. Dynamic stability of the slope is examined by applying various seismic inputs to the base of the model as plane waves. Seismic inputs are applied using different series of sinusoidal waves with a velocity range of 0.004-0.20 m/s (frequencies of 0.5, 1, 5, and 10 Hz) (Table 3.10). These seismic velocity

amplitudes of the October event at specific frequencies were calculated in Section 3.4.4 (Table 3.10).

In order to simulate a system's non-reflecting properties of earthquake motion, viscous boundary conditions were assigned to minimize wave reflection at the model boundaries. We investigated the rock slope threshold of tolerance under seismic loadings at different frequencies; the result shows that the minimum required horizontal velocity (i.e., velocity threshold) to reduce the factor of safety to below 1 is frequency dependent. Table 3.13 shows the velocity thresholds at four frequencies (0.5, 1, 5, and 10 Hz). Based on the velocity range given in Table 3.10 and the results from Table 3.13, it can be suggested that the friction angle of the sliding surface was a value from 24^{o} to less than 30^{o}. The results show that friction angle of 35^{o} for the sliding surface (non pre-sheared sliding surface) required a stronger earthquake (higher range of velocity values) to fail. Figure 3.19 displays the slope displacement with a friction angle of 24^{o} at those frequencies noted above; plots indicate that the maximum displacement of the rock mass in x direction is the highest at the frequency of 10 Hz. Note that the maximum displacement value for frequencies of 0.5, and 1 Hz is almost 3.8 meters, while it increases to 4.2 and 6.7 meters for frequencies of 5 and 10 Hz, respectively. Other researchers (Havenith et al., 2003; Bhasin and Kaynia, 2004) have investigated frequency dependence of rock slopes and demonstrated that the largest deformation occurs for source frequencies in the range of the fundamental frequency of the slope system. In our case, the natural frequency of the slope is estimated to be around 5 Hz using UDEC Version 5.0.

Figure 3.20 shows the sequence of movements in the slope, with friction angle of 24^o for the sliding rock mass, after the applied seismic loading at the frequency of 1 Hz and velocity amplitude of 0.1; the arrows represent displacement directions, and their colors indicate the displacement values. Figure 3.20 contains three parts and each part shows the time evolution of failure mechanism at 2.66 s, 5.32 s, and 11.84 s in parts a, b, and c respectively. The rock slope is shown to be unstable and has slid 6.1 m after 11.84 s.

Table 3.13: The velocity thresholds for instability at four frequencies for three different friction angles

Friction angle=24^o		**Friction angle=30^o**		**Friction angle=35^o**	
Velocity(m/s)	**Frequency**	**Velocity(m/s)**	**Frequency**	**Velocity(m/s)**	**Frequency**
0.1	0.5	---	0.5	---	0.5
0.09	1	---	1	---	1
0.008	5	0.03	5	0.03	5
0.007	10	0.009	10	0.01	10

3.6 Conclusions

In this chapter, a detailed analysis of the 1985 North Nahanni earthquake-triggered landslide was carried out. We estimated the October 1985 earthquake ground motion data at the site of the rockslide, based on the available strong motion records from the second earthquake on December 23. We used the defined method to obtain the seismic velocities of the October event. Slope stability analysis was performed using the distinct element method (UDEC). First, static loading was applied to simulate the rock mass conditions at the site, before the slide. Considering the friction angle range of 24^o to 35^o for the sliding surface, the computational results revealed an averaged factor of safety of slightly larger than 1 for the rock slope. Furthermore, dynamic stability analysis indicates that the magnitude deformation of the North Nahanni rock masses was dependent on the frequency content of the source

signal. Considering the calculated seismic data of the Nahanni earthquake on October 1985 with the estimated velocity thresholds at different frequencies, friction angles for the sliding surface before failure are predicted to be a value from 24^{o} to less than 30^{o}. As a conclusion, the North Nahanni rock slope had a low factor of safety and was susceptible to failure prior to the seismic shaking and the 1985 Nahanni first main shock operated as a trigger event that accelerated the occurrence of the slide.

Figure 3.1: Aerial viewed of the 1985 North Nahanni rockslide (volume of 7.6 Mm^3) triggered by the October 1985 Nahanni earthquake.

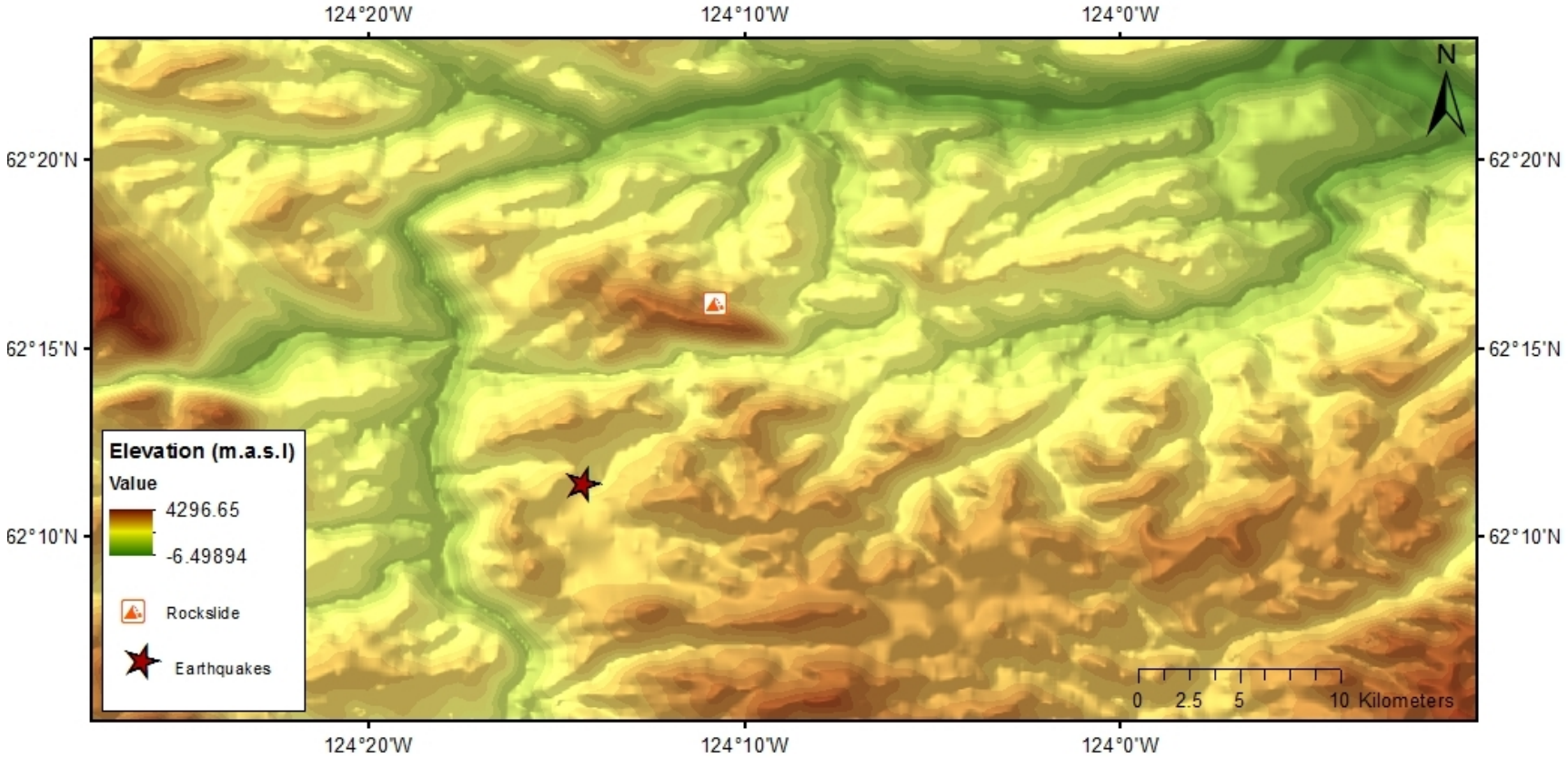

Figure 3.2: Digital elevation model (DEM) showing the peaks and valleys of the study area

The 1985 North Nahanni rockslide and the epicenter of 1985 Nahanni earthquakes are shown. DEM was generated, using GIS, from a digital topographic map that was obtained from the Geogratis website of Natural Resources Canada (http://geogratis.cgdi.gc.ca/).

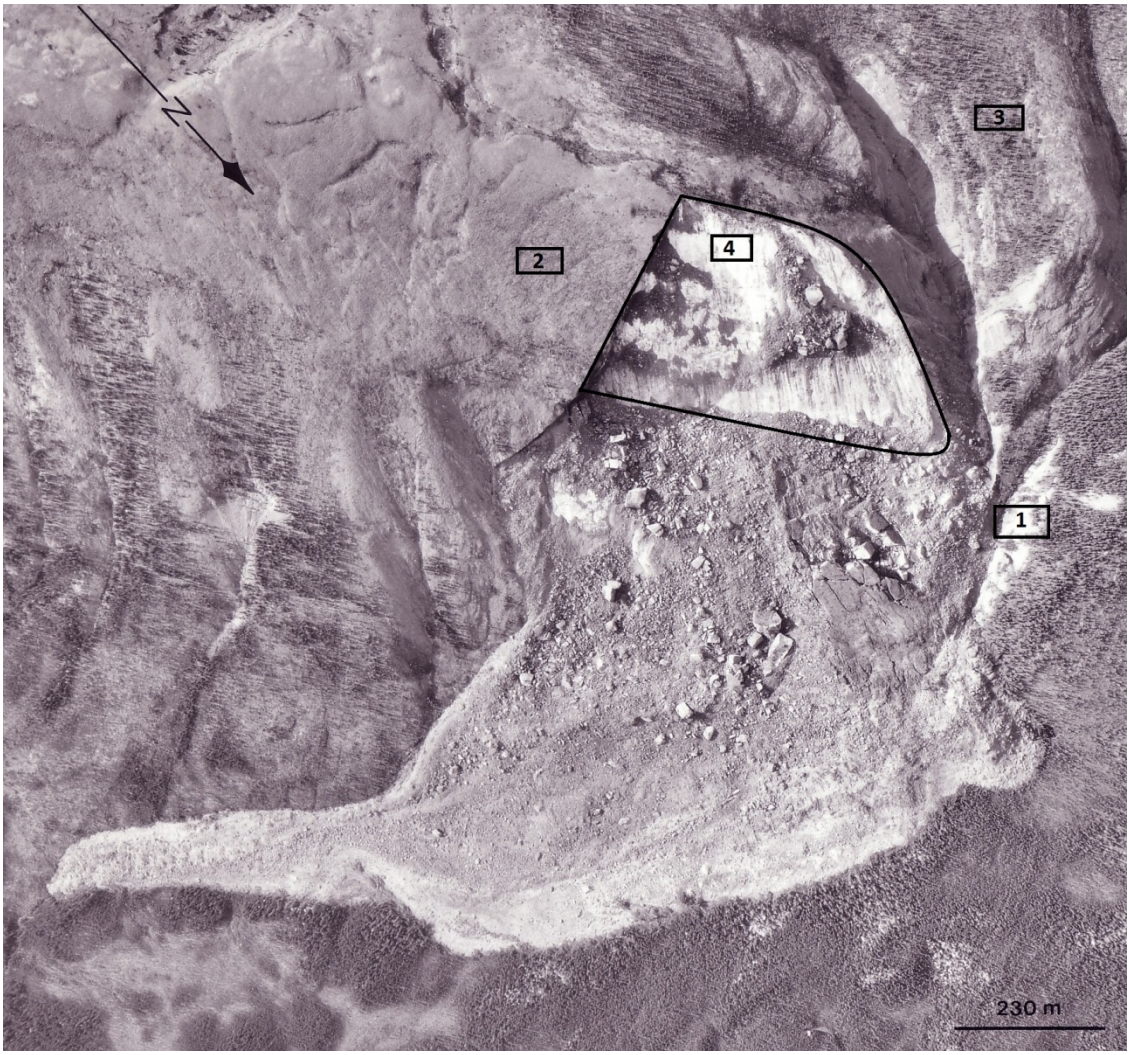

Figure 3.3: Aerial photograph of the North Nahanni rockslide, showing the extent of the slide and different rock mass structural domains discussed in text.

Most of the detached rock mass was deposited at the foot of the slope and a small portion of the deposited debris travelled almost 1 km perpendicular to the sliding slope. Large blocks are observable in the debris, directly beneath the detachment zone (S.G. Evans, personal communication, 2012).

Figure 3.4: View of the 1985 North Nahanni rockslide, looking south. Photo was taken by S. G. Evans (1986).

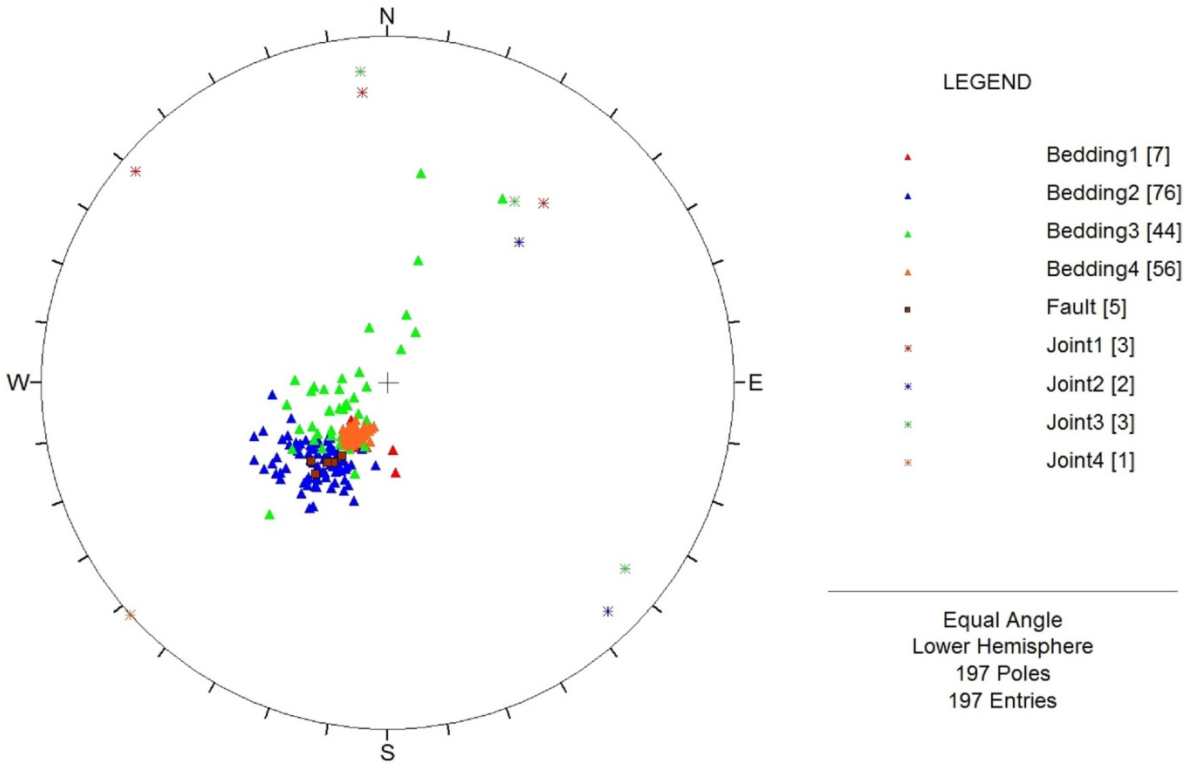

Figure 3.5: Lower hemisphere of equal area stereographic projection showing poles of 197 discontinuities

Discontinuity sets are bedding, fault, and 4 joint sets. The projection shows poles to northeast dipping bedding, fault, and joint set J4, poles to southeast/south/southwest dipping joint set J1, poles to northwest/southwest dipping joint set J2, and poles to northwest/southwest/south dipping joint set J3.

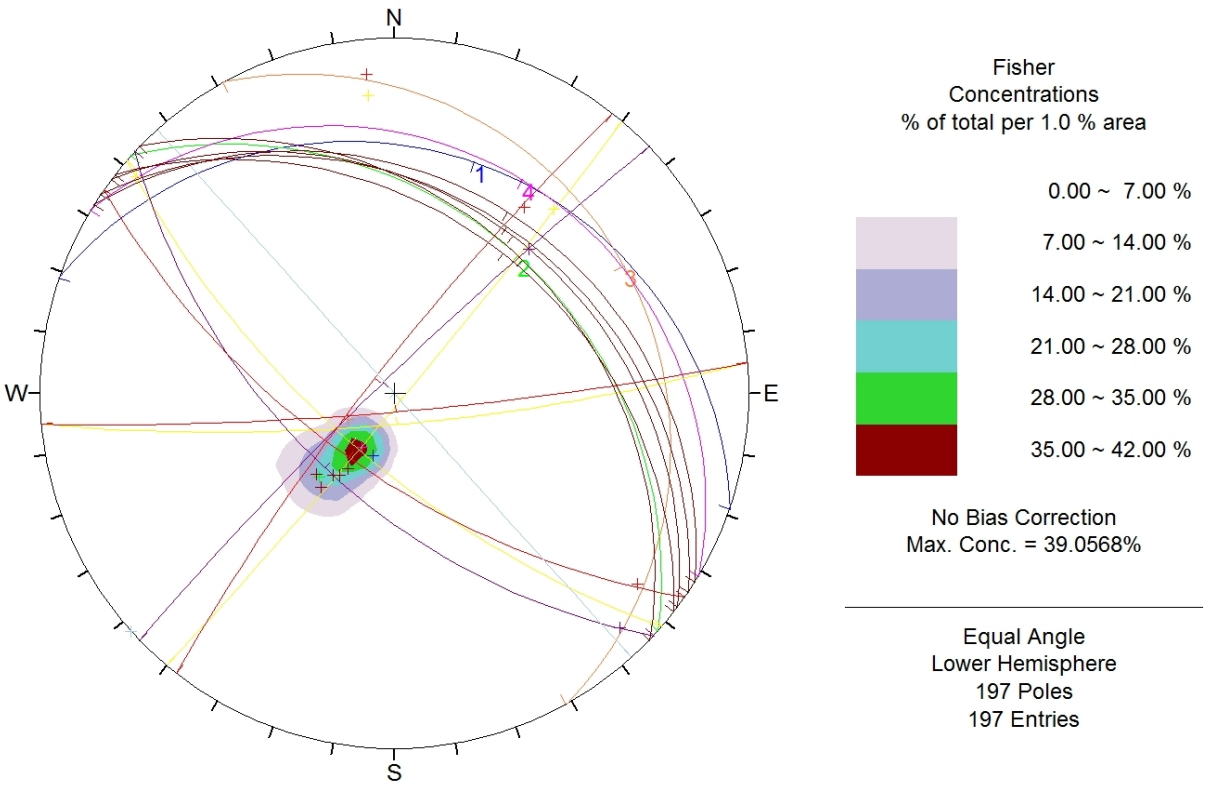

Figure 3.6: Lower hemisphere of equal area stereographic projection showing the planes, the major pole concentration and contours of the mean orientations of bedding in all the four structural domains.

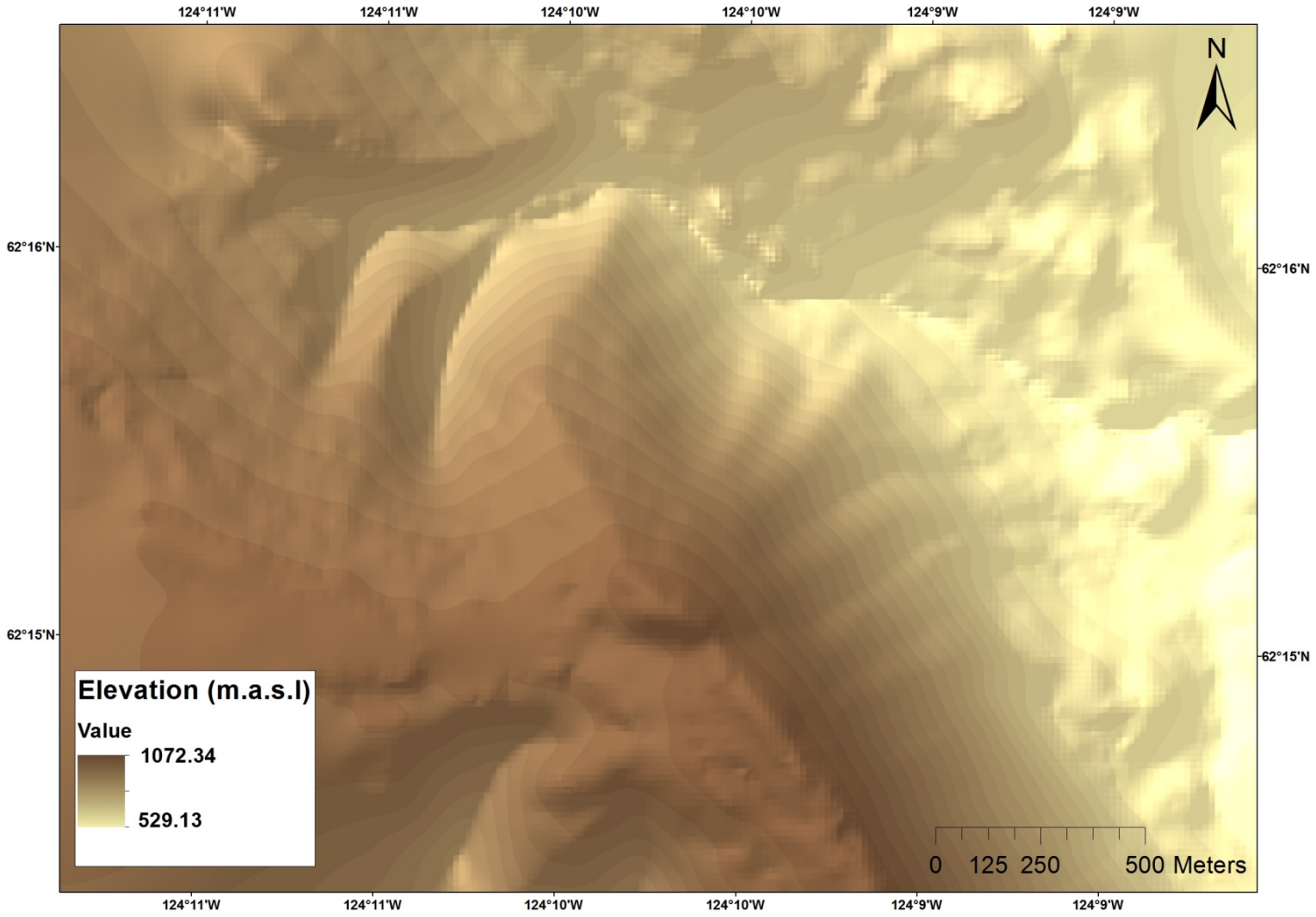

Figure 3.7: Digital elevation model (DEM) showing the North Nahanni rock slope before failure.

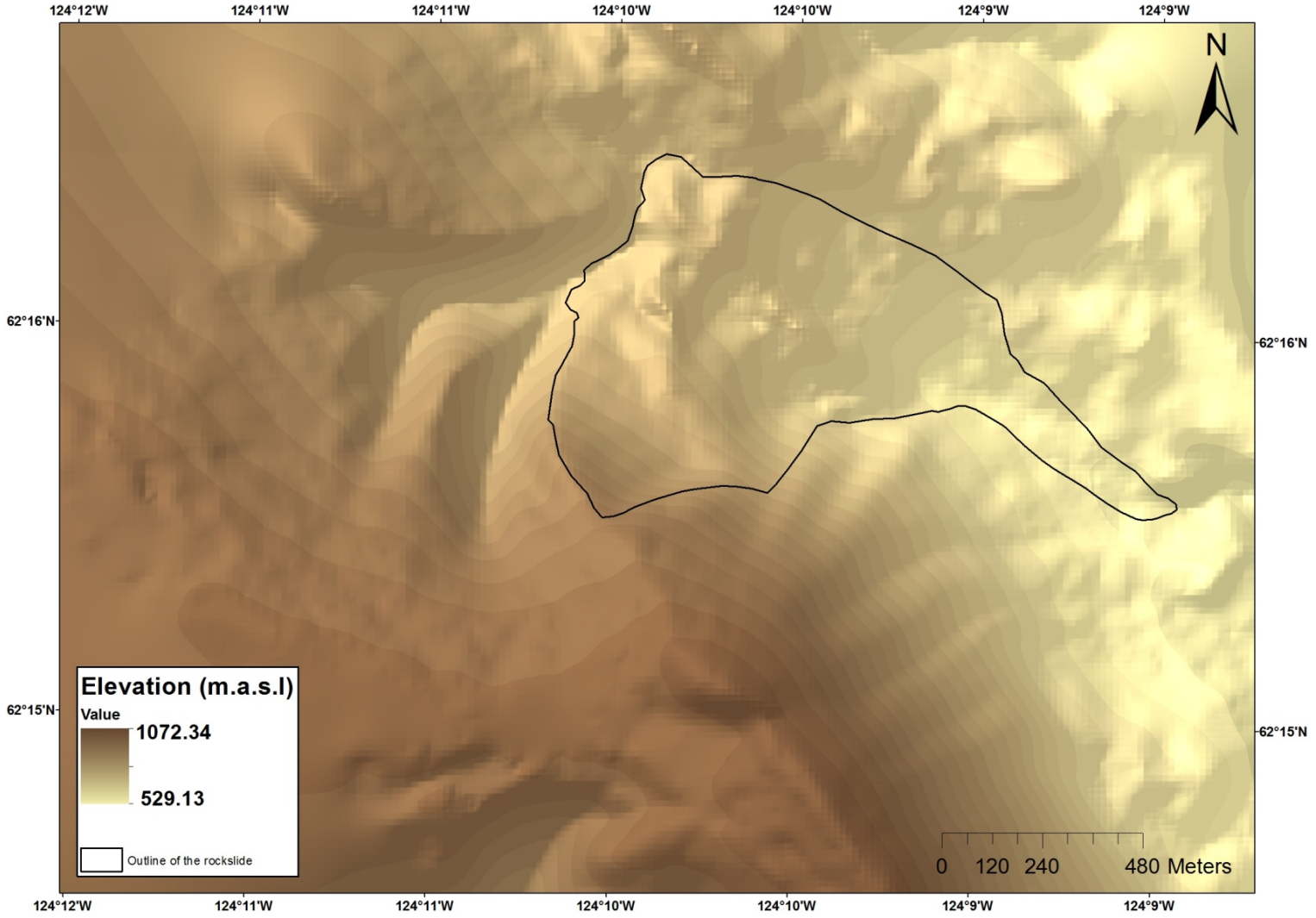

Figure 3.8: Digital elevation model (DEM) showing the rock slope after the slide. Black polygon shows the outline of the rockslide

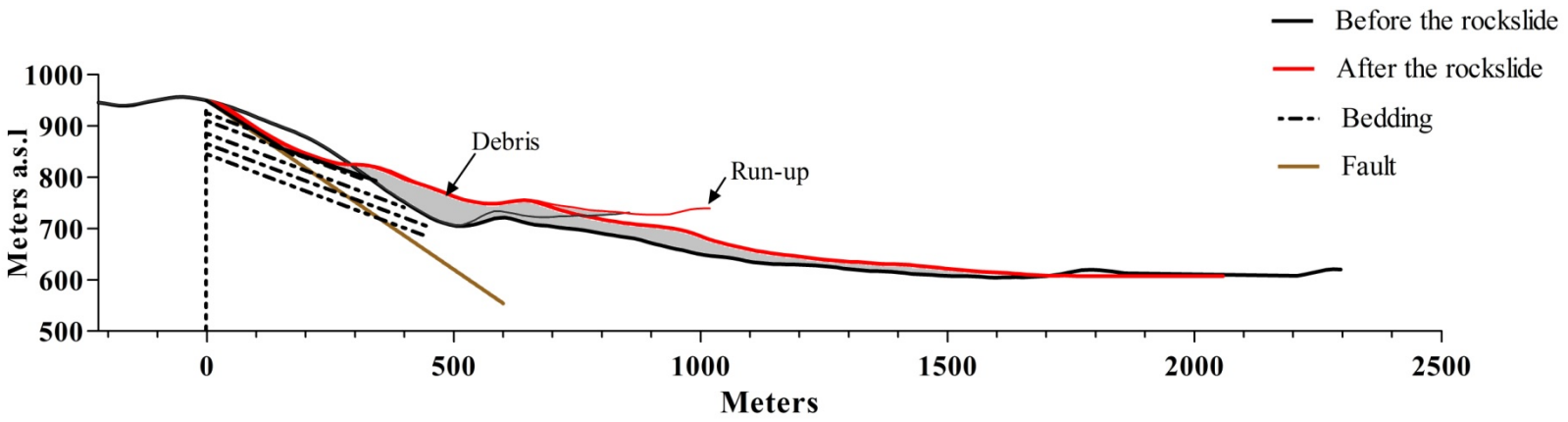

Figure 3.9: Topographic profile of the North Nahanni rockslide path, before (Black line) and after (Red line) the landslide.

The sliding surface consists of two planar elements. The lower part dips at 20° and is parallel to bedding, and the upper part dips at 35°. Slope profiles were constructed using the 0.5 m resolution digital elevation models (Figures 3.7 and 3.8).

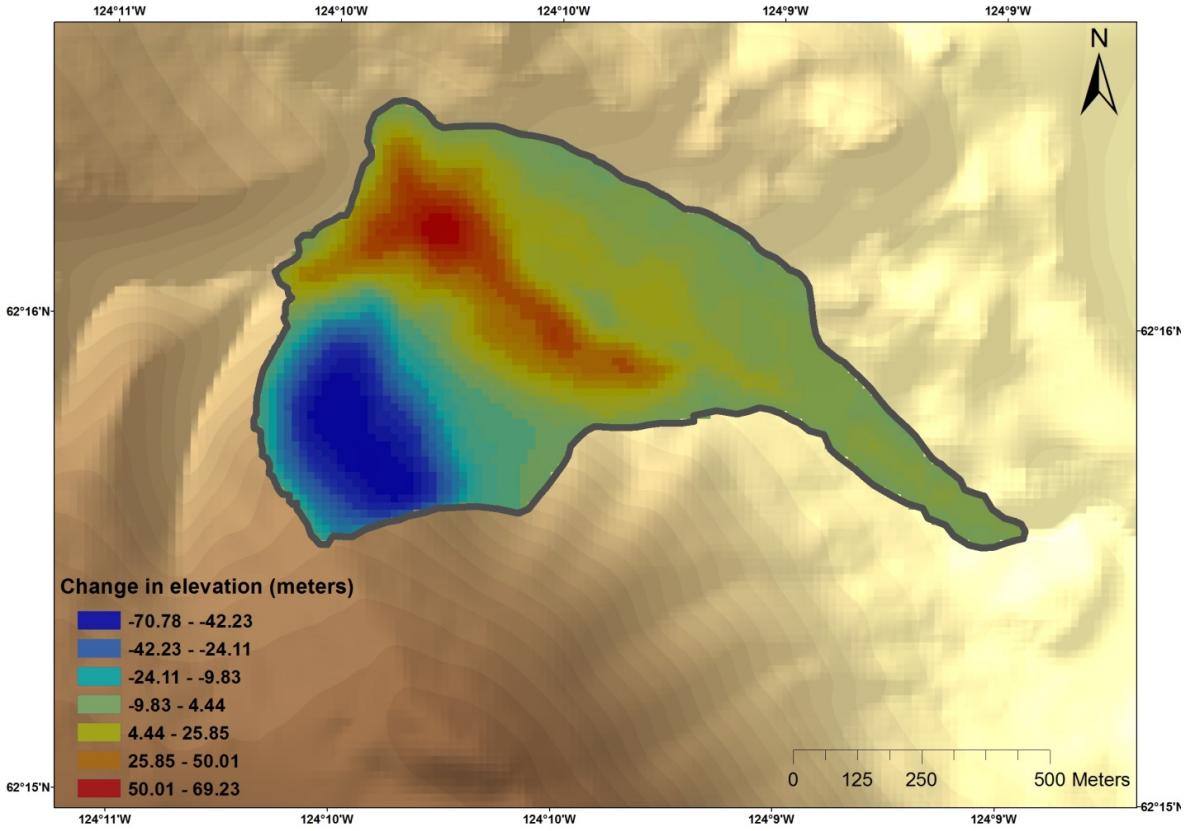

Figure 3.10: Topographic change map which result from using change detection technique in GIS.

Pre- and post-landslide images (Figure 3.7 and 3.8, respectively) have been used to generate the map.

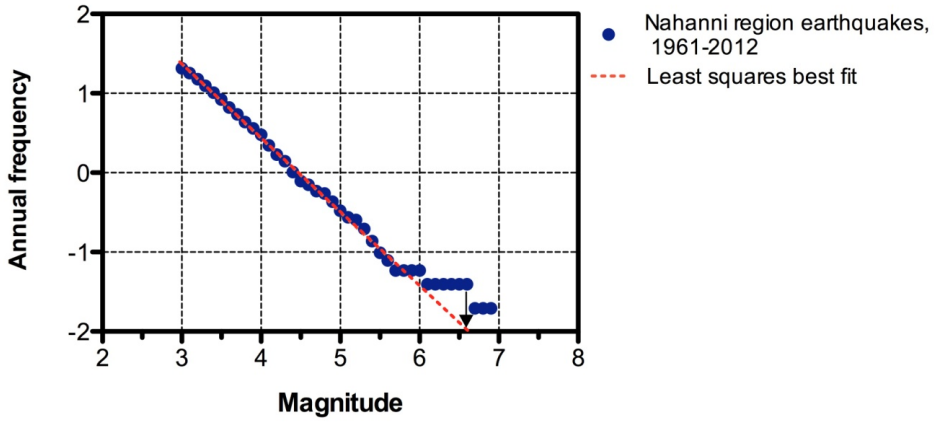

Figure 3.11: Annual cumulative magnitude-frequency distribution of earthquakes, 300 Kilometers in radius around the 1985 Nahanni earthquakes, with M ≥ 3 for the period of 1961-2012

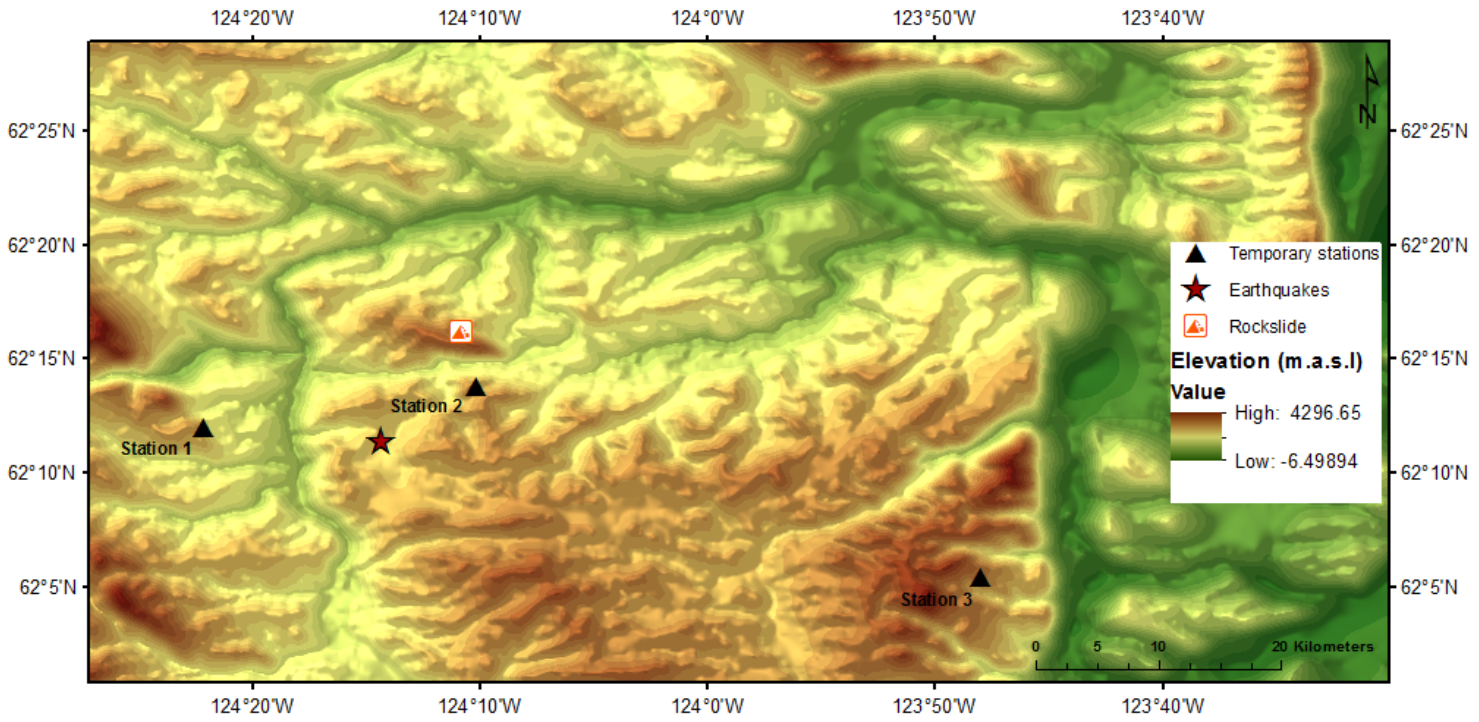

Figure 3.12: Digital elevation model (DEM) showing the location of the 1985 Nahanni earthquakes and the North Nahanni rockslide as well as the three temporary stations (Black triangles).

(a)

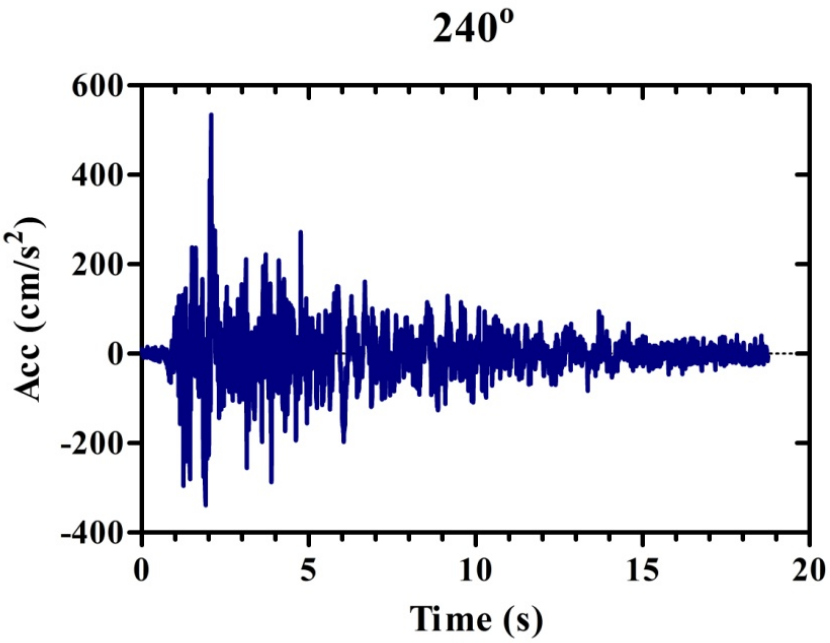

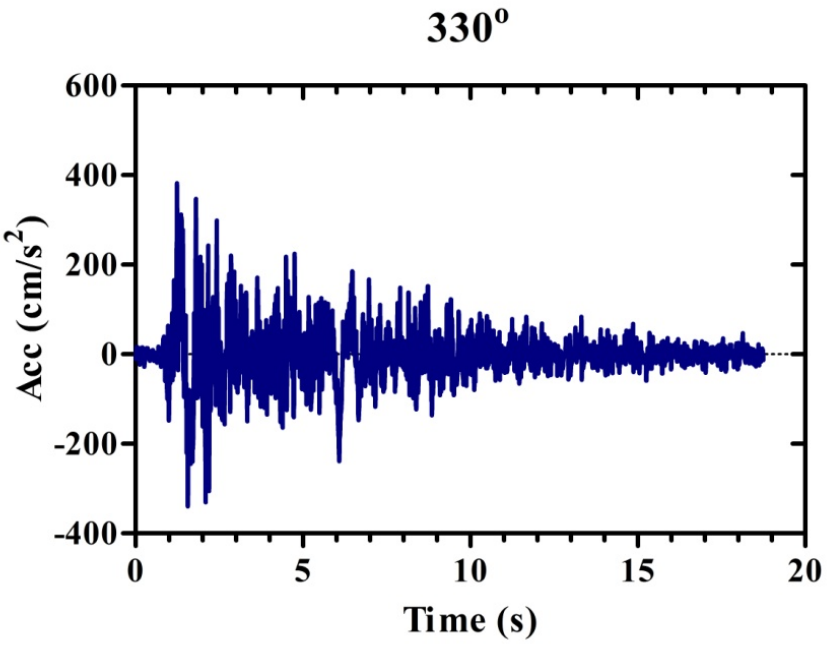

(b)

Figure 3.13: Two horizontal components of accelerations of the December 23, 1985 Nahanni earthquake at Station 2 (Figure 3. 12); part (a) at 240° and part (b) at 330°.

(a)

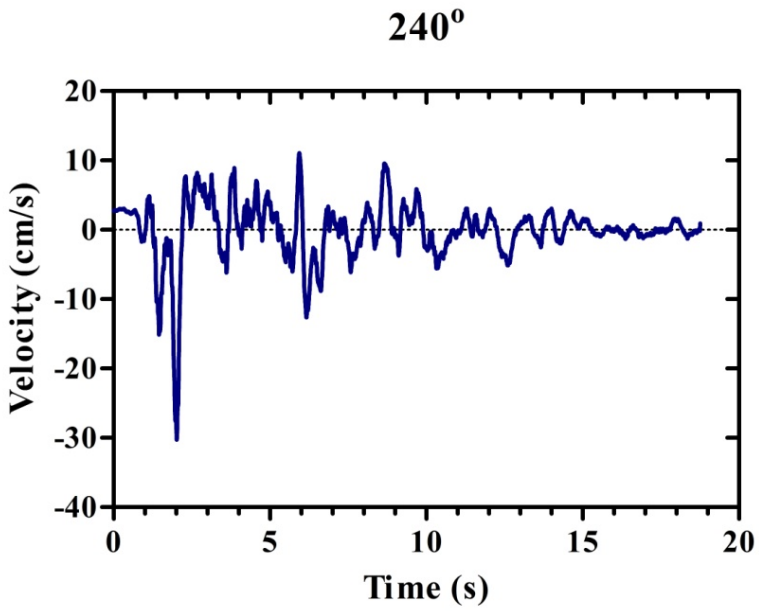

(b)

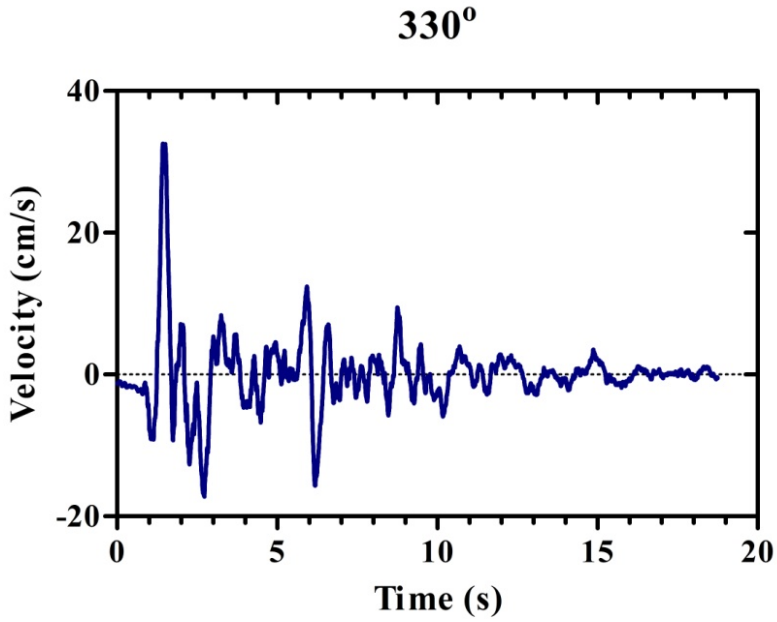

Figure 3.14: Observed horizontal velocity time histories of the December, 1985 earthquake at Station 2.

Two components of horizontal velocity at direction of 240° (a), and 330° (b)

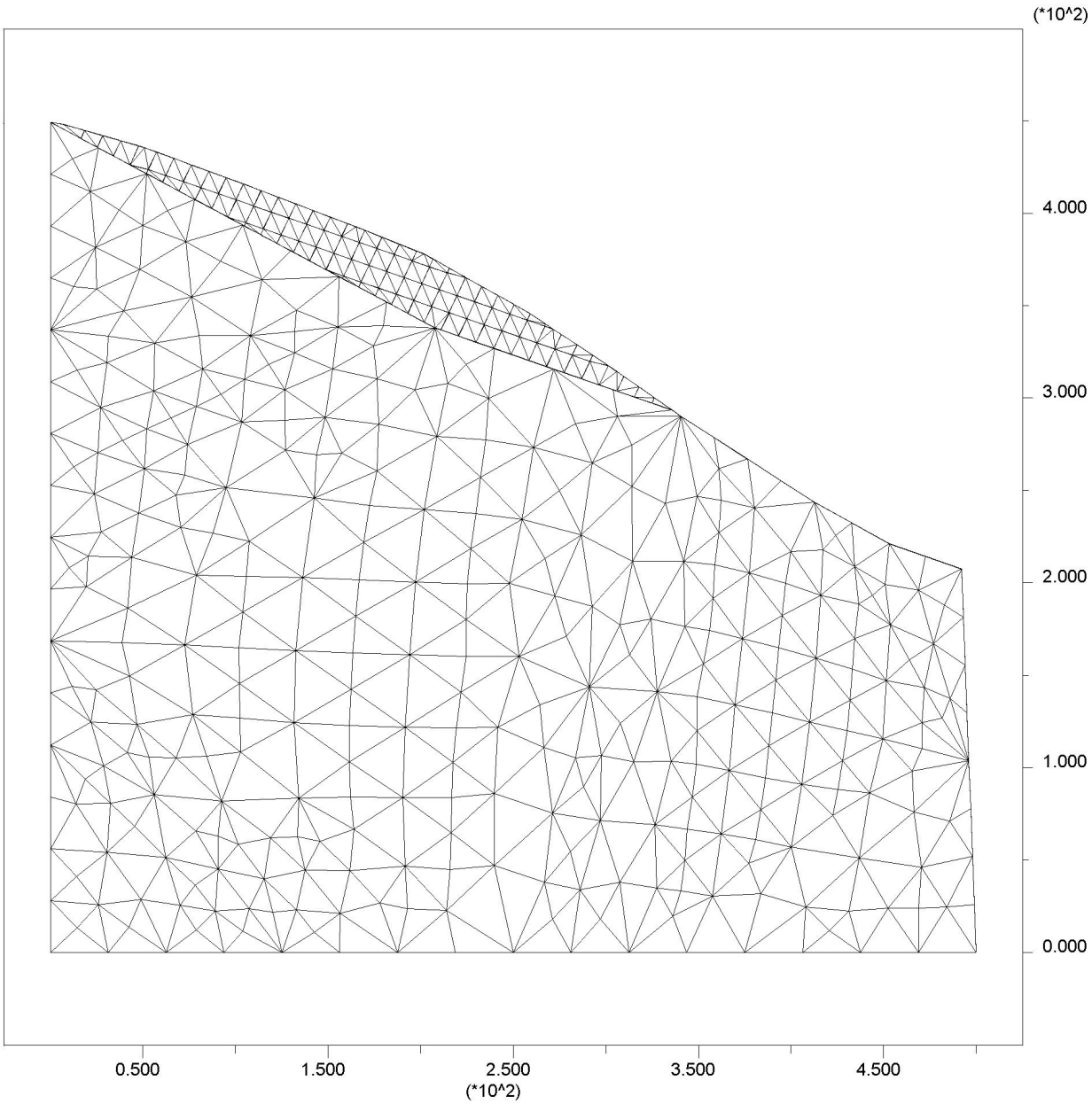

Figure 3.15: Geometry of the numerical slope model. All blocks are discretized into deformable triangular finite-difference zones. The units are in meters.

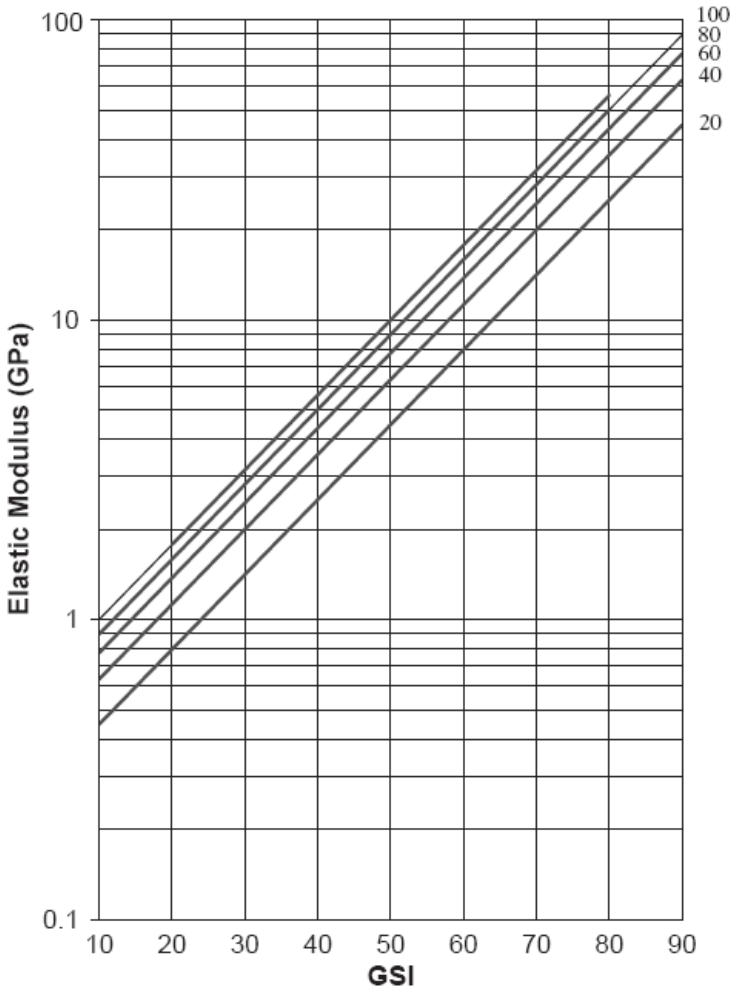

Figure 3.16: Relationship between elastic modulus and Geological Strength Index (GSI). Reproduced from Cia et al. (2004).

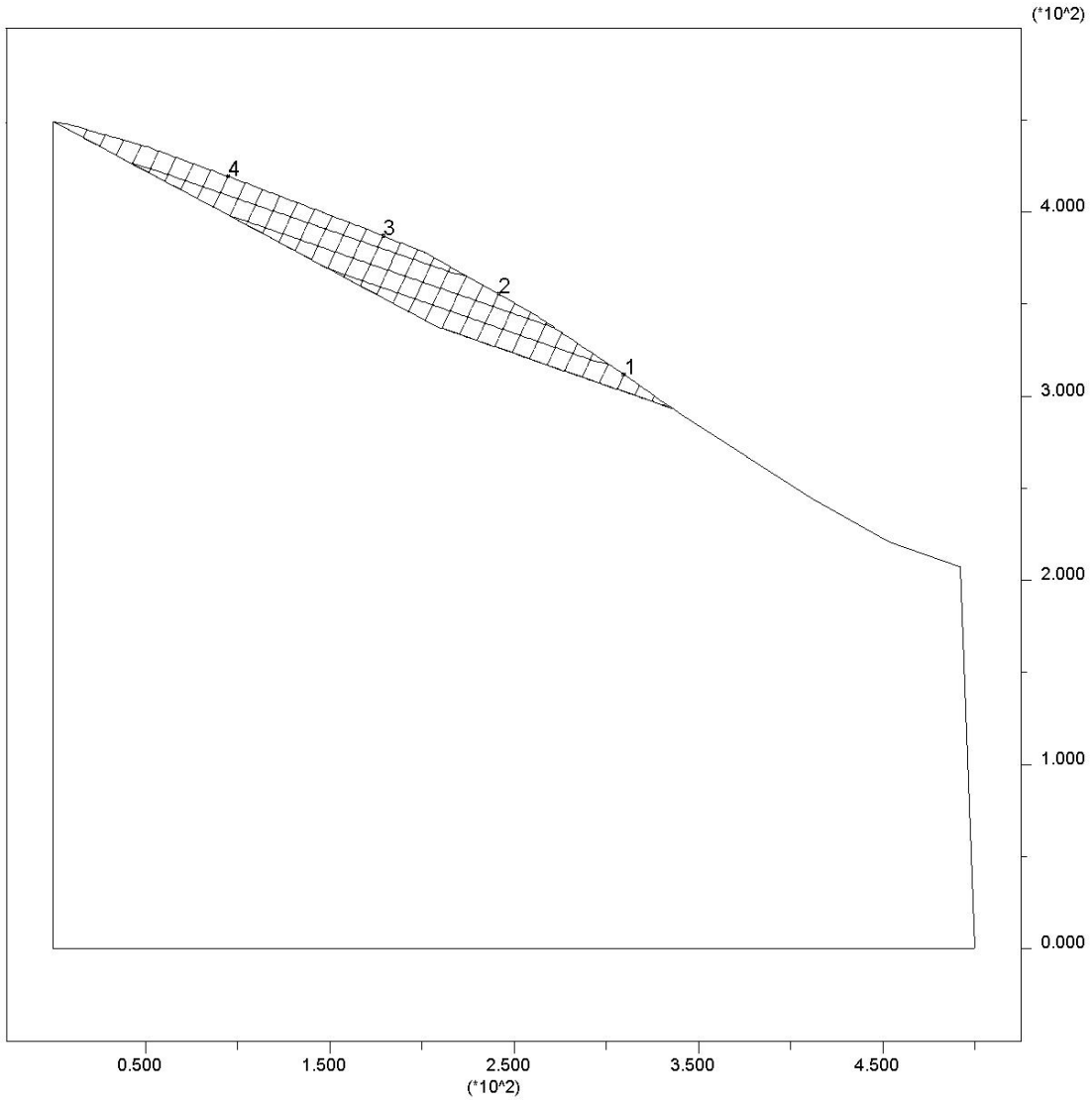

Figure 3.17: Geometry of the numerical slope model; numbers represent monitoring points for the slope and the x and y axes refer to the model dimensions.

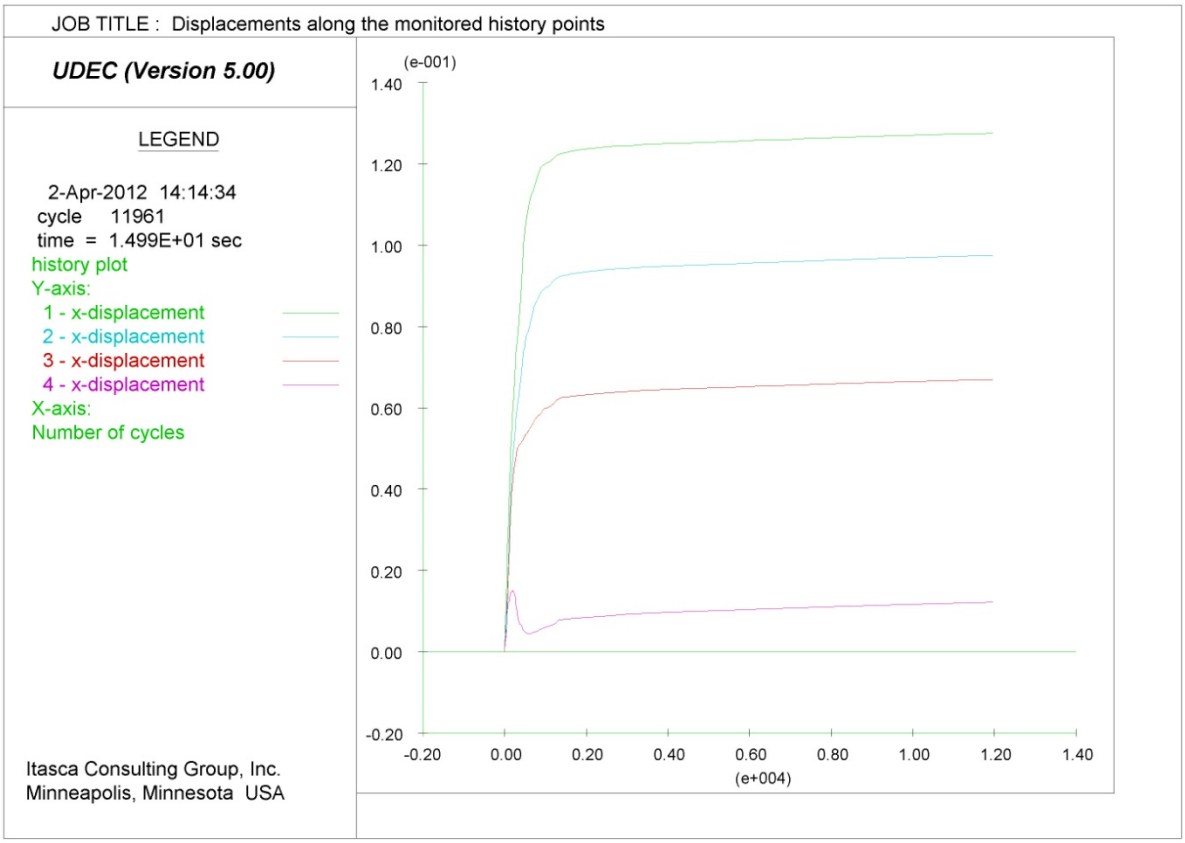

Figure 3.18: Shear displacements along the monitored history points indicating equilibrium conditions before seismic shaking.

(a)

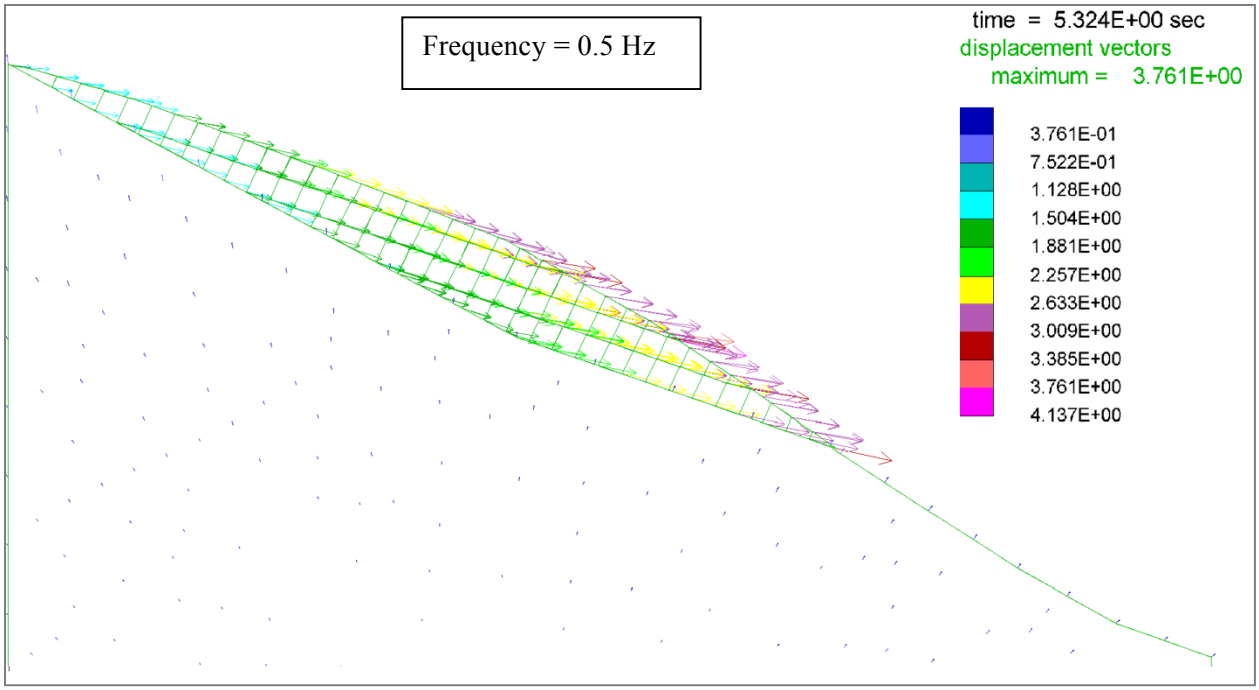
Frequency = 0.5 Hz
time = 5.324E+00 sec
displacement vectors
maximum = 3.761E+00
3.761E-01
7.522E-01
1.128E+00
1.504E+00
1.881E+00
2.257E+00
2.633E+00
3.009E+00
3.385E+00
3.761E+00
4.137E+00

(b)

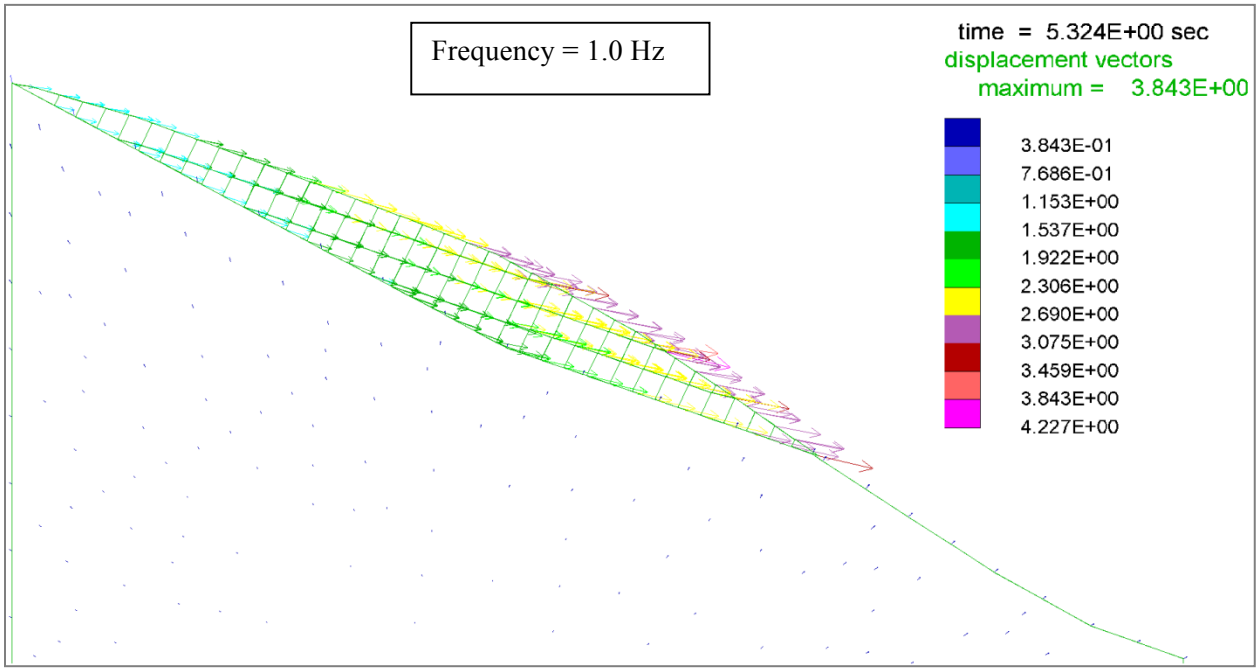
Frequency = 1.0 Hz
time = 5.324E+00 sec
displacement vectors
maximum = 3.843E+00
3.843E-01
7.686E-01
1.153E+00
1.537E+00
1.922E+00
2.306E+00
2.690E+00
3.075E+00
3.459E+00
3.843E+00
4.227E+00

(c)

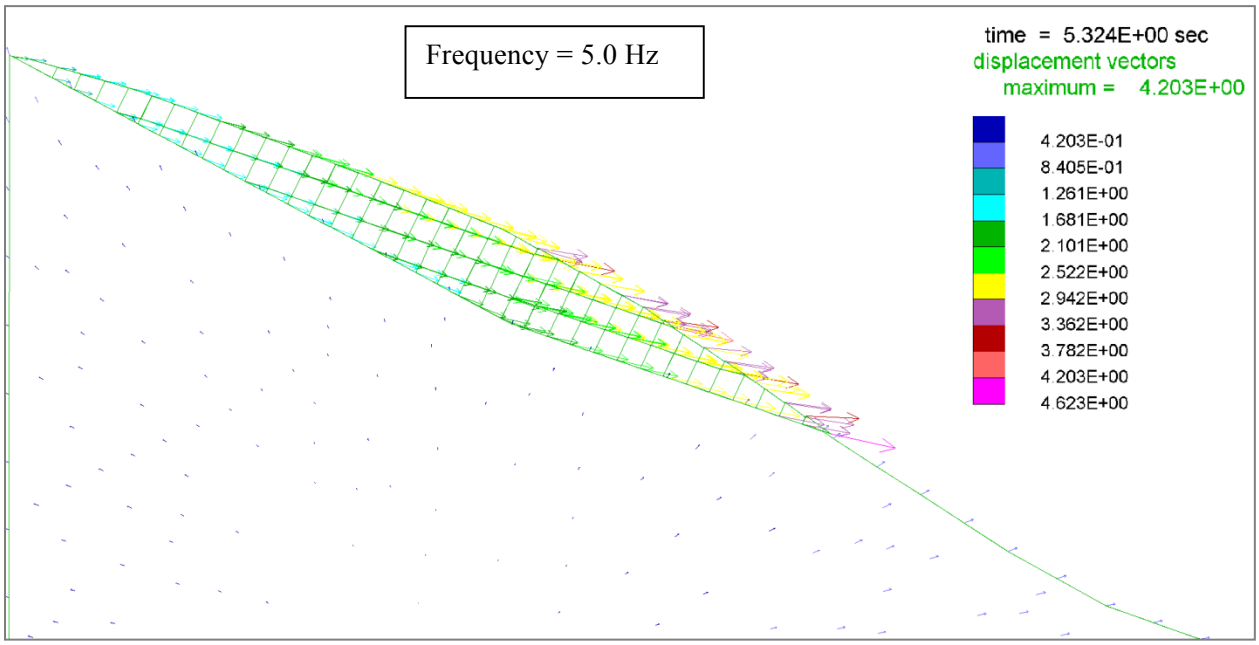

(d)

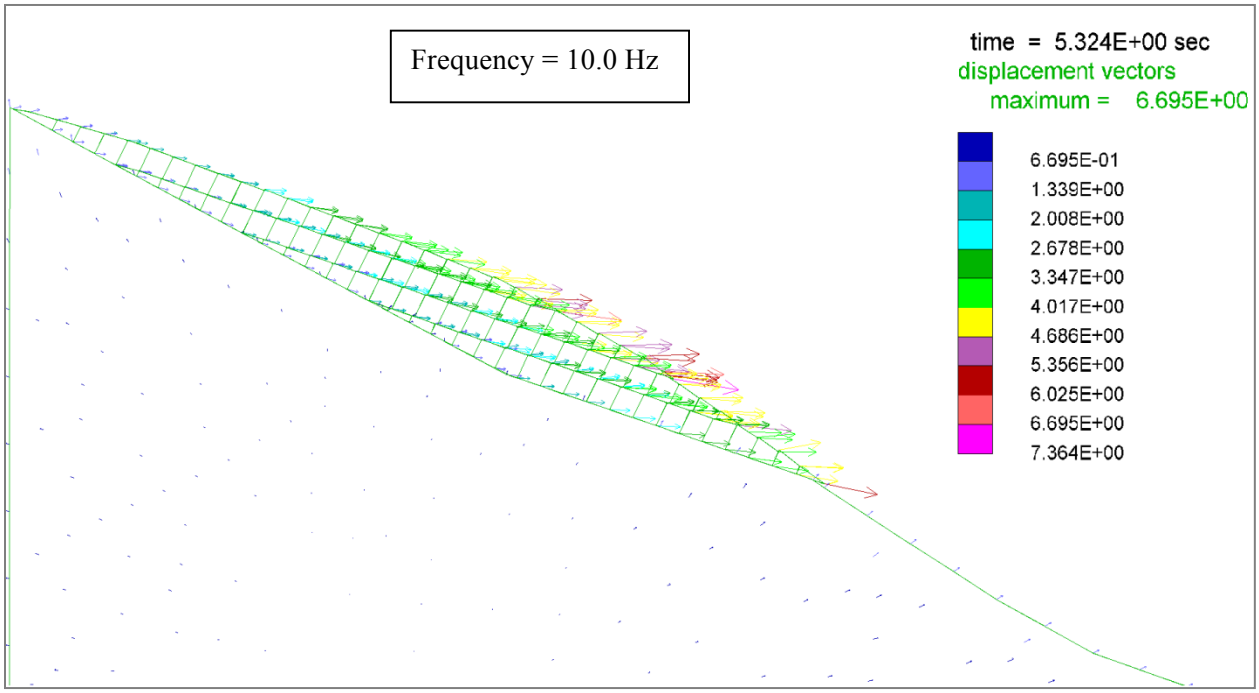

Figure 3.19: Frequency dependent behavior of the slope during the seismic shaking.

The arrows represent displacement directions, and their colors indicate the displacement values. Seismic loading was applied at frequencies of 0.5 Hz (part a), 1.0 Hz (part b), 5.0 Hz (part c), and 10 Hz (part d).

(a)

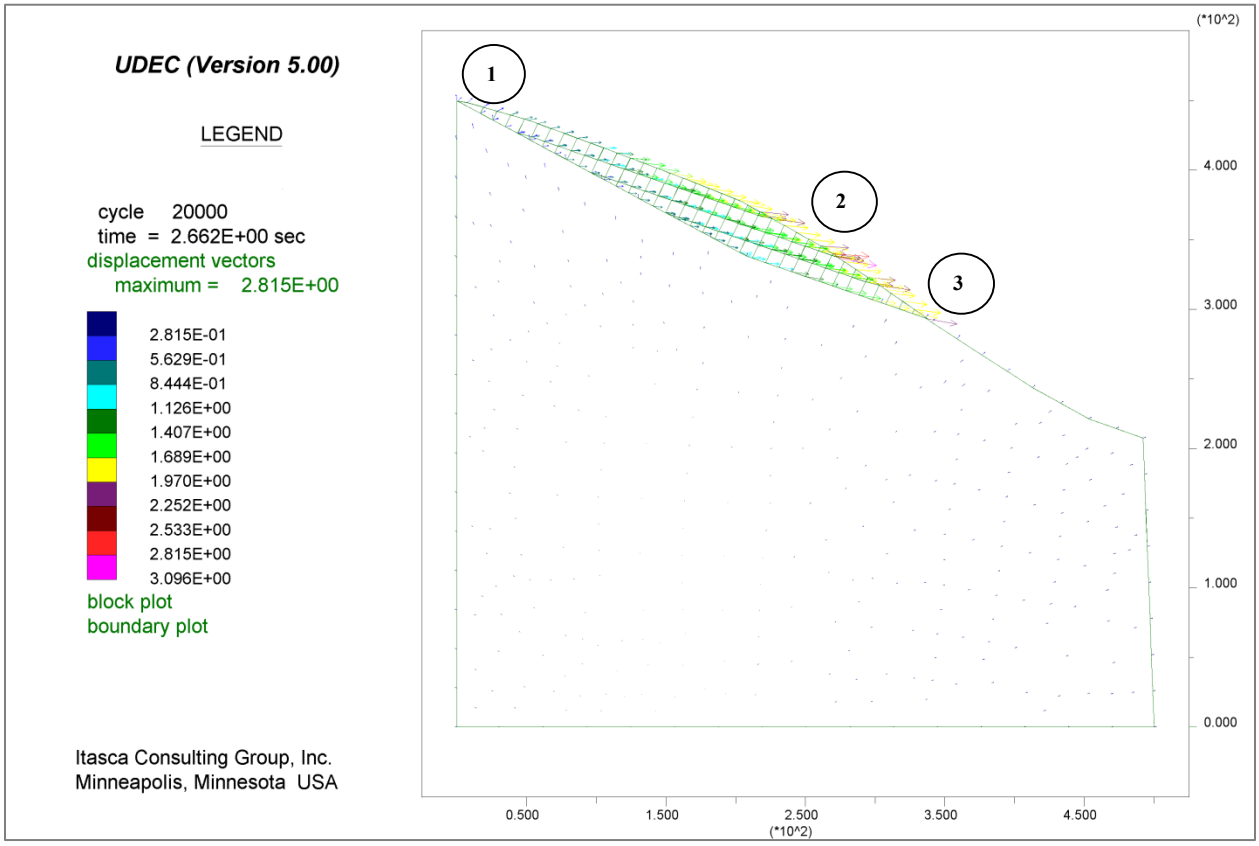
UDEC (Version 5.00)
LEGEND
cycle 20000
time = 2.662E+00 sec
displacement vectors
maximum = 2.815E+00
2.815E-01
5.629E-01
8.444E-01
1.126E+00
1.407E+00
1.689E+00
1.970E+00
2.252E+00
2.533E+00
2.815E+00
3.096E+00
block plot
boundary plot
Itasca Consulting Group, Inc.
Minneapolis, Minnesota USA
1
2
3
(*10^2)
4.000
3.000
2.000
1.000
0.000
0.500
1.500
2.500
3.500
4.500
(*10^2)

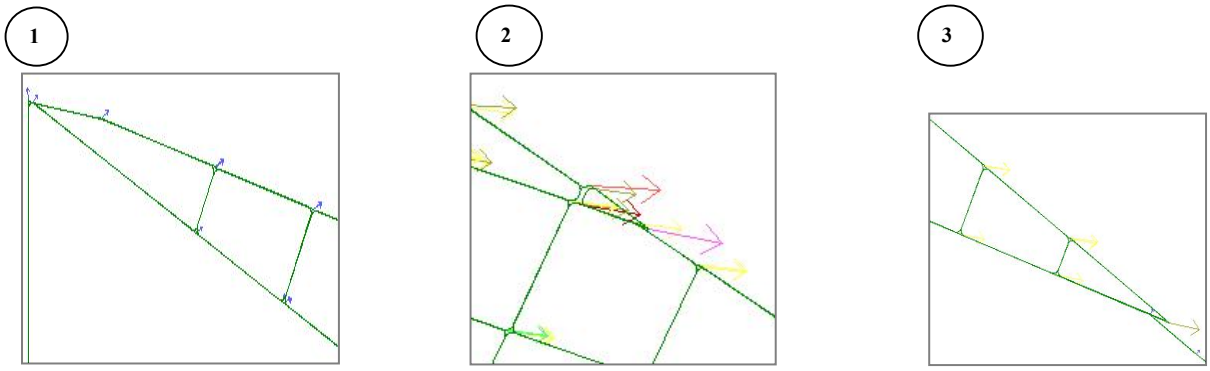
1
2
3

(b)

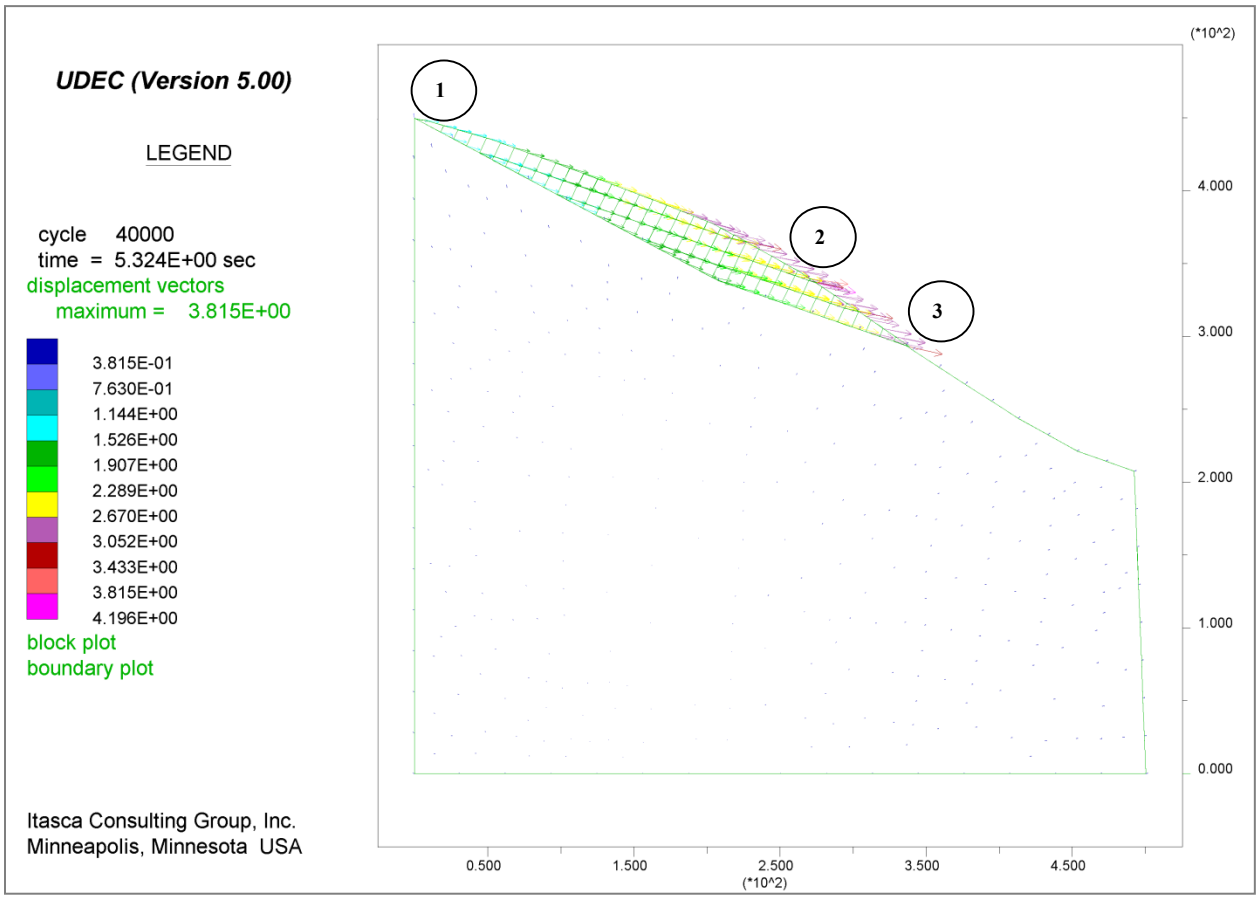
UDEC (Version 5.00)
LEGEND
cycle 40000
time = 5.324E+00 sec
displacement vectors
maximum = 3.815E+00
3.815E-01
7.630E-01
1.144E+00
1.526E+00
1.907E+00
2.289E+00
2.670E+00
3.052E+00
3.433E+00
3.815E+00
4.196E+00
block plot
boundary plot
Itasca Consulting Group, Inc.
Minneapolis, Minnesota USA
1
2
3
(*10^2)
4.000
3.000
2.000
1.000
0.000
0.500
1.500
2.500
3.500
4.500
(*10^2)

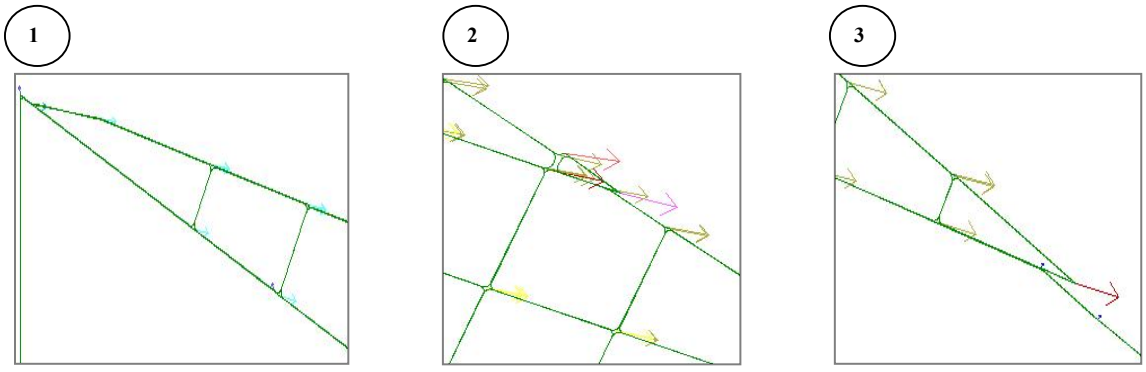
1
2
3

(c)

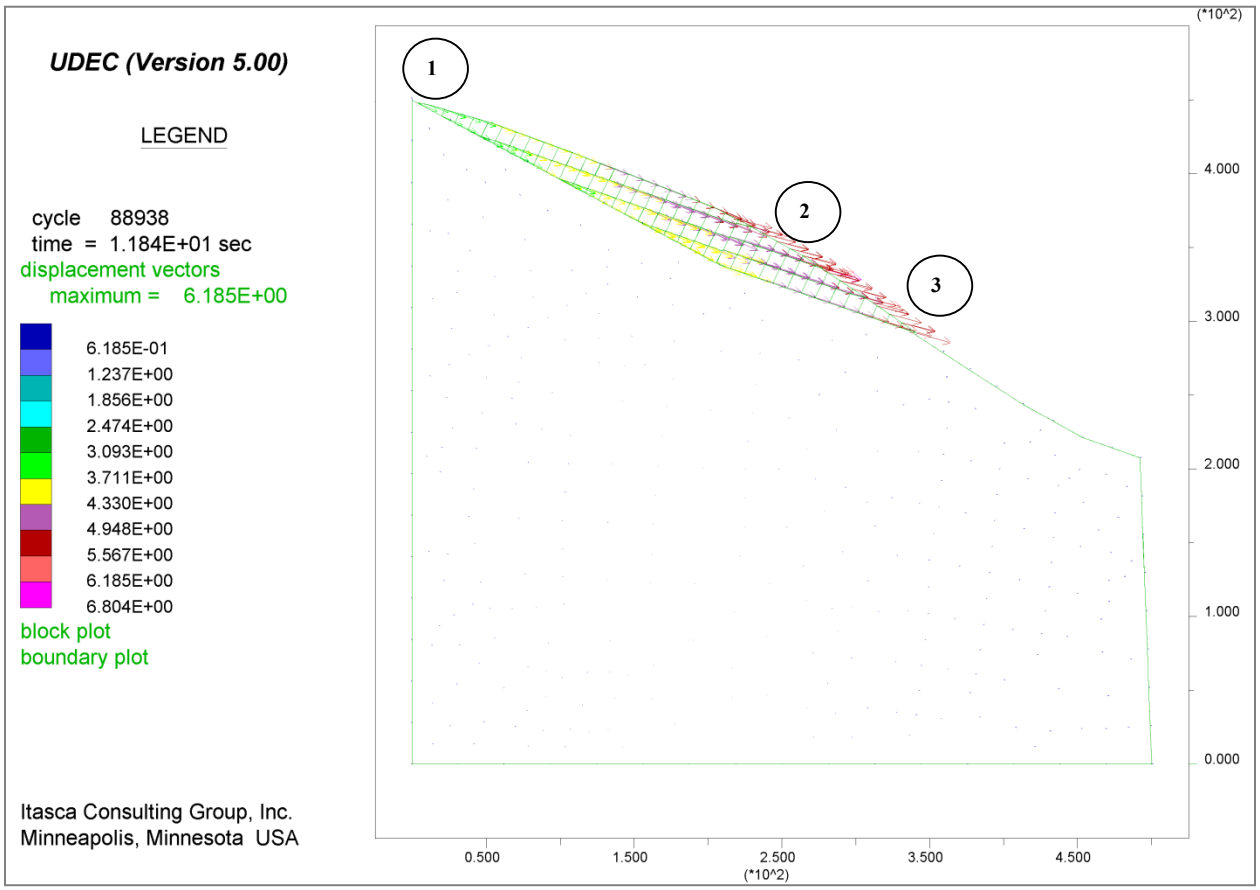

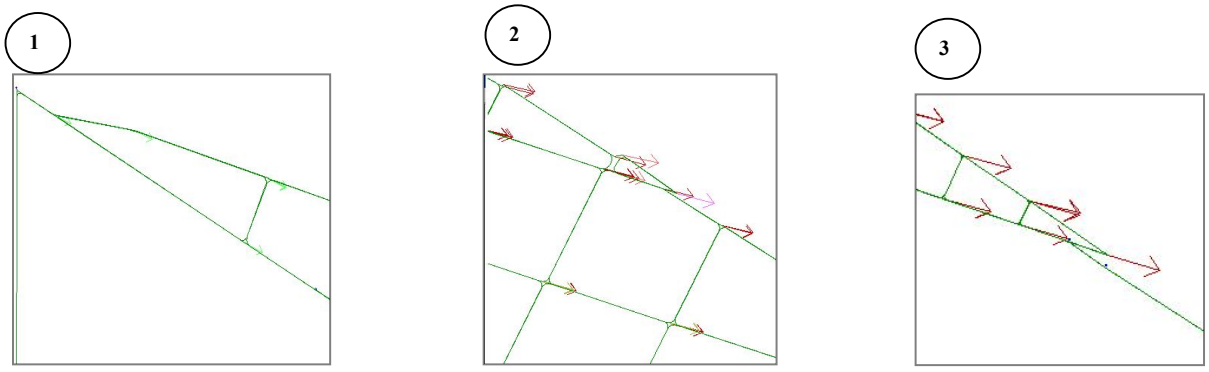

Figure 3.20: The sequence of movements on the slope after the applied seismic loading (velocity amplitude=0.1, frequency=1.0 Hz). Arrows indicating the sliding motion and their colors show the displacement values of the blocks.

Chapter 4

Summary and Conclusions

Landslides are complex natural phenomena that are commonly associated with a trigger, such as an earthquake, a rapid snowmelt or a heavy rain storm. This thesis is a comprehensive investigation of earthquake-triggered landslides. This study has gone some way towards enhancing our understanding of the behavior and occurrence of earthquake-triggered landslides in relation to earthquake parameters at both global and local scales. The research in Chapter 2 will serve as a basis for future study of landslide hazard and risk assessment, and the numerical stability analysis in Chapter 3 provides useful insights into the failure mechanisms in the North Nahanni rock slope. Since earthquake-triggered landslides are common geological phenomena in many parts of the world, understanding the failure mechanism of the North Nahanni rockslide provides some new insights into rock slope deformations under seismic loading. The main conclusions from each chapter are summarized in the following sections.

4.1 Global study

The compilation of a comprehensive global landslide or earthquake catalog sounds simple in theory; however, it is challenging in practice. Two new worldwide catalogs were compiled: one containing landslide-triggering earthquakes and one containing earthquake-triggered landslides during the period of 1998 to 2009, and 1900-2010, respectively. Data sources include a comprehensive review of the existing literature, and also PAGER-CAT (the USGS-based earthquake catalog), which contains information on earthquake-triggered

secondary hazards (e.g., landslide, tsunami). Analysis of the earthquake-triggered landslides from 1998 to 2009 indicated that the total number of landslides triggered by an earthquake is not a function of the earthquake magnitude. This result agrees with that of Rodriquez et al. (1999). The most dominant types of ETLs, during the period 1998-2009, are found to be rock fall and rockslide.

Analysis of the relationships between large-scale ETL characteristics and earthquake parameters has shown that the volume of the largest landslide triggered by a given LTE cannot be expressed as a simple function of earthquake magnitude, while the volume of those below a threshold of ca. 80 Mm^3 in the range of 20-80 Mm^3 has a relatively good correlation with calculated earthquake peak ground motions at the site of the earthquake-triggered landslide. This result is consistent with Meunier et al.'s (2007) findings which showed the rate of slope failure is proportional to the peak ground acceleration (PGA) or peak ground velocity (PGV) caused by an earthquake. However, our observation indicates that, landslide volumes greater than 80 Mm^3 are a consequence of complex progressive failure mechanisms initiated by earthquake shaking (i.e., above this threshold volume, landslide volume is independent of PGA, PGV and PSA). Surprisingly, when the magnitude and frequency curves of huge ETLs and non-ETLs are plotted, both curves have almost the same slope and intercept values. Distribution maps of large-scale landslides indicated that the large-scale ETLs and NETLs distributions during the period 1900-2010 are almost concentrated in the same regions. Observations showed that the type of triggering event (e.g., earthquake, heavy rain) does not change the general relationship between the frequency of landslides and their volume and generally, large-scale landslides occurred in areas which are prone to landslides.

4.2 1985 North Nahanni earthquake-triggered landslide

A detailed analysis of the 1985 North Nahanni earthquake-triggered landslide was carried out in Chapter 3, which also reviewed the structural geology of the North Nahanni slope. Detailed studies of the characteristics of the rockslide and of the two main Nahanni earthquakes are presented.

Chapter 3 also defined a method to estimate the October 1985 earthquake ground motion response spectra based on the available strong motion records from the second main shock on December 23. Estimated ground motion data were used as seismic inputs for dynamic stability analysis. The discontinuum numerical modeling technique, using UDEC Version 5.0, was applied in the analysis of the North Nahanni rockslide. Various cases were simulated to obtain a better understanding of the effects of static and dynamic loading. Based on static analysis, averaged factors of safety were found to have values of slightly larger than 1. The results indicate that the slope was marginally stable under static conditions, before the earthquake. Dynamic stability analysis was conducted by applying different series of sinusoidal shear waves to the model as plane waves. Overall, instability was observed for given seismic inputs at a specific range of friction angles (24^o to 30^o) for the sliding surface, and the deformation behavior of the North Nahanni rock masses was found to be dependent on the frequency of the seismic signals. Previous studies showed that the largest deformation occurs for source frequencies in the range of the natural frequency of the slope system. We estimated the natural frequency of the North Nahanni slope to be around 5 Hz.

Since the static slope stability analysis showed that the slope was close to instability prior to the seismic shaking, we suggest that the 1985 Nahanni earthquake operated as a trigger event that accelerated the occurrence of the slide. This finding supports our earlier results of the global scale study, which showed that the triggering event does not change the general trend of the frequency-volume distribution of landslides; however it can accelerate the occurrence of slope failure.

Appendix A

Lists of Class B and Class C landslide-triggering earthquakes worldwide, and Listing of literature sources for Class B

List of landslide-triggering earthquakes (Class B), 1998-2009

#	Date	Latitude	Longitude	M_w	Depth (km)	Location	Number of landslides
1	28/03/1999	30.51 N	79.40 E	6.6	15	India (chamoli)	Several, but 1 huge
2	15/06/1999	18.39 N	97.44 W	7	70	Mexico	Few
3	17/08/1999	40.75 N	29.86 E	7.6	17	Turkey(Izmit)	Several
4	26/01/2001	23.42 N	70.23 E	7.7	16	India (Bhuj)	Few
5	22/06/2002	35.63 N	49.05 E	6.5	10	Iran(Avaj)	Many
6	26/05/2003	38.85 N	141.57 E	7	68	Japan	Few
7	27/09/2003	50.04 N	87.81 E	7.3	16	Russian (Federation)	Few
8	20/03/2006	36.62 N	5.33 E	5	10	Algeria	Few
9	16/07/2007	37.53 N	138.45 E	6.6	12	Japan (Niigata-Chuetsu-Oki)	Several
10	15/08/2007	13.39 S	76.60 W	8	39	Peru	Few
11	24/05/2008	4.33 N	73.76 W	5.9	8	Colombia	Individual
12	08/01/2009	10.16 N	84.20 W	6.1	14	Costa Rica	Several
13	06/04/2009	42.33 N	13.33 E	6.3	8	Italy	Few

List of landslide-triggering earthquakes (Class C), 1998-2009

Number	Date	Latitude	Longitude	Mw	Depth	Location
1	10/01/1998	14.37 N	91.47 W	6.6	33	Guatemala
2	04/02/1998	37.08 N	70.09 E	5.9	33	Afghanistan
3	20/02/1998	36.48 N	71.09 E	6.4	235	Afghanistan
4	12/04/1998	46.25 N	13.65 E	5.7	10	Slovenia
5	17/07/1998	23.41 N	120.74 E	5.7	12	Taiwan, Province of China
6	29/07/1998	32.31 S	71.29 W	6.4	51	Chile
7	04/08/1998	0.59 S	80.39 W	7.2	33	Ecuador
8	13/11/1998	27.79 N	53.61 E	5.4	33	Iran
9	19/11/1998	27.31 N	101.03 E	5.6	33	China
10	25/01/1999	4.46 N	75.72 W	6.2	17	Colombia
11	03/04/1999	16.66 S	72.66 W	6.8	87	Peru
12	11/08/1999	34.79 N	32.94 E	5.6	33	Cyprus
13	25/09/1999	23.74 N	121.16 E	6.5	17	Taiwan, Province of China
14	30/09/1999	16.06 N	96.93 W	7.5	60	Mexico
15	12/11/1999	40.76 N	31.16 E	7.2	10	Turkey
16	26/11/1999	16.42 S	168.21 E	7.5	33	Vanuatu
17	03/12/1999	40.36 N	42.35 E	5.7	19	Turkey
18	07/02/2000	26.29 S	30.89 E	4.5	5	South Africa
19	17/05/2000	24.22 N	121.06 E	5.4	10	Taiwan; province of China
20	04/06/2000	4.72 S	102.09 E	7.9	33	Indonesia
21	10/06/2000	23.84 N	121.23 E	6.4	33	Taiwan, Province of China
22	17/06/2000	63.97 N	20.49 W	6.5	10	Iceland
23	01/07/2000	34.22 N	139.13 E	6.1	10	Japan
24	15/07/2000	34.32 N	139.26 E	6.1	10	Japan
25	16/07/2000	20.25 N	122.04 E	6.4	33	Philippines
26	28/07/2000	23.36 N	120.92 E	5.7	33	Taiwan; province of China
27	30/07/2000	33.90 N	139.38 E	6.5	10	Japan
28	04/08/2000	48.79 N	142.25 E	6.8	10	Russian federation
29	06/10/2000	35.46 N	133.13 E	6.7	10	Japan
30	16/11/2000	3.98 S	152.17 E	8	33	Papua New Guinea
31	17/02/2001	13.79 N	89.11 W	4.1	10	El Salvador
32	28/02/2001	47.15 N	122.73 W	6.8	51	United states

Number	Date	Latitude	Longitude	Mw	Depth	Location
33	12/04/2001	24.77 N	99.06 E	5.6	10	China
34	08/05/2001	13.61 N	88.80 W	5.7	10	El Salvador
35	05/06/2001	6.88 S	146.39 E	6.4	10	Papua New Guinea
36	07/07/2001	17.54 S	72.08 W	7.6	33	Peru
37	17/07/2001	46.74 N	11.20 E	4.7	10	Italy
38	02/01/2002	17.60 S	167.86 E	7.2	21	Vanuatu
39	03/03/2002	36.50 N	70.48 E	7.4	225	Afghanistan
40	05/03/2002	6.03 N	124.25 E	7.5	31	Philippines
41	25/03/2002	36.06 N	69.32 E	6.1	8	Afghanistan
42	27/03/2002	36.02 N	69.34 E	5.6	10	Afghanistan
43	31/03/2002	24.28 N	122.18 E	7.1	32	Taiwan; province of China
44	12/04/2002	35.96 N	69.42 E	5.9	10	Afghanistan
45	18/04/2002	27.54 S	70.59 W	6.7	62	Chile
46	15/05/2002	24.64 N	121.92 E	6.2	10	Taiwan; province of China
47	28/05/2002	28.94 S	66.80 W	6	22	Argentina
48	08/09/2002	3.30 S	142.95 E	7.6	13	Papua New Guinea
49	10/10/2002	1.76 S	134.30 E	7.6	10	Indonesia
50	31/10/2002	41.79 N	14.87 E	5.9	10	Italy
51	01/11/2002	35.52 N	74.65 E	5.4	33	Pakistan
52	20/11/2002	35.41 N	74.52 E	6.3	33	Pakistan
53	27/11/2002	14.49 S	167.83 E	5.9	33	Vanuatu
54	02/12/2002	37.75 N	21.09 E	5.7	10	Greece
55	01/05/2003	39.01 N	40.46 E	6.4	10	Turkey
56	21/05/2003	36.96 N	3.63 E	6.8	12	Algeria
57	24/06/2003	32.93 N	49.48 E	4.6	33	Iran
58	21/07/2003	25.98 N	101.29 E	6	10	China
59	25/07/2003	38.43 N	141.00 E	5.5	10	Japan
60	26/07/2003	22.85 N	92.31 E	5.7	10	Bangladesh
61	14/08/2003	39.16 N	20.61 E	6.3	10	Greece
62	22/09/2003	19.78 N	70.67 W	6.4	10	Dominican Republic
63	25/09/2003	41.82 N	143.91 E	8.3	27	Japan
64	18/11/2003	12.03 N	125.42 E	6.5	35	Philippines
65	10/12/2003	23.04 N	121.36 E	6.8	10	Taiwan; province of China

Number	Date	Latitude	Longitude	Mw	Depth	Location
66	22/12/2003	35.71 N	121.10 W	6.6	7	United states
67	26/12/2003	29.00 N	58.31 E	6.6	10	Iran
68	14/02/2004	34.77 N	73.22 E	5.5	11	Pakistan
69	24/02/2004	35.14 N	4.00 W	6.4	0	Morocco
70	01/05/2004	24.08 N	121.61 E	5.2	44	Taiwan; province of China
71	28/05/2004	36.29 N	51.61 E	6.3	17	Iran
72	12/07/2004	46.30 N	13.64 E	5.2	7	Slovenia
73	18/07/2004	38.00 S	176.51 E	5.6	5	New Zealand
74	08/11/2004	37.40 N	138.86 E	5.5	10	Japan
75	09/11/2004	37.37 N	138.83 E	5.1	10	Japan
76	11/11/2004	8.15 S	124.87 E	7.5	10	Indonesia
77	20/11/2004	9.60 N	84.17 W	6.4	16	Costa Rica
78	22/11/2004	33.30 N	47.98 E	5	36	Iran
79	20/12/2004	37.04 N	28.21 E	5.4	5	Turkey
80	26/12/2004	3.30 N	95.98 E	9	30	Indonesia
81	12/03/2005	39.44 N	40.98 E	5.6	11	Turkey
82	20/03/2005	33.81 N	130.13 E	6.6	10	Japan
83	19/04/2005	33.64 N	130.18 E	5.5	18	Japan
84	13/06/2005	19.99 S	69.20 W	7.8	115	Chile
85	14/12/2005	30.48 N	79.26 E	5.3	44	India
86	14/02/2006	27.38 N	88.39 E	5.3	30	India
87	14/03/2006	3.60 S	107.20 E	6.7	30	Indonesia
88	20/06/2006	33.07 N	104.95 E	5.1	24	China
89	22/07/2006	28.00 N	104.14 E	5	55	China
90	25/08/2006	28.01 N	104.15 E	5.2	21	China
91	15/10/2006	19.88 N	155.94 W	6.7	38	United states minor outlying islands
92	17/12/2006	0.63 N	99.86 E	5.8	30	Indonesia
93	02/06/2007	23.03 N	101.05 E	6.1	5	China
94	21/07/2007	38.94 N	70.49 E	5.2	10	Tajikistan
95	22/07/2007	30.88 N	78.24 E	5.1	19	India
96	26/10/2007	35.30 N	76.75 E	5.2	10	Pakistan
97	29/03/2008	12.18 S	77.16 W	5.3	51	Peru
98	25/05/2008	32.56 N	105.42 E	6.1	18	China

Number	Date	Latitude	Longitude	Mw	Depth	Location
99	29/05/2008	64.00 N	21.01 W	6.3	9	Iceland
100	01/07/2008	10.37 S	75.51 W	5.4	32	Central Peru
101	23/07/2008	39.80 N	141.46 E	6.8	108	Japan
102	01/08/2008	32.03 N	104.72 E	5.7	11	Sichuan-Gansu, China
103	28/10/2008	30.64 N	67.35 E	6.4	15	Pakistan
104	20/02/2009	34.20 N	73.90 E	5.5	12	Pakistan
105	19/05/2009	25.29 N	37.74 E	5.7	5	Western Saudi Arabia
106	29/05/2009	17.03 S	168.33 E	5.7	13	Vanuatu
107	02/06/2009	17.76 S	167.95 E	6.3	15	Vanuatu
108	15/07/2009	45.76 S	166.56 E	7.8	12	The South Island, N.Z
109	02/09/2009	7.78 S	107.30 E	7	46	Java, Indonesia
110	22/10/2009	36.52 N	70.95 E	6.2	185	Afghanistan

Appendix B

Cross-section map of the English Chief Anticline (taken from: *www.nrcan.gc.ca*)

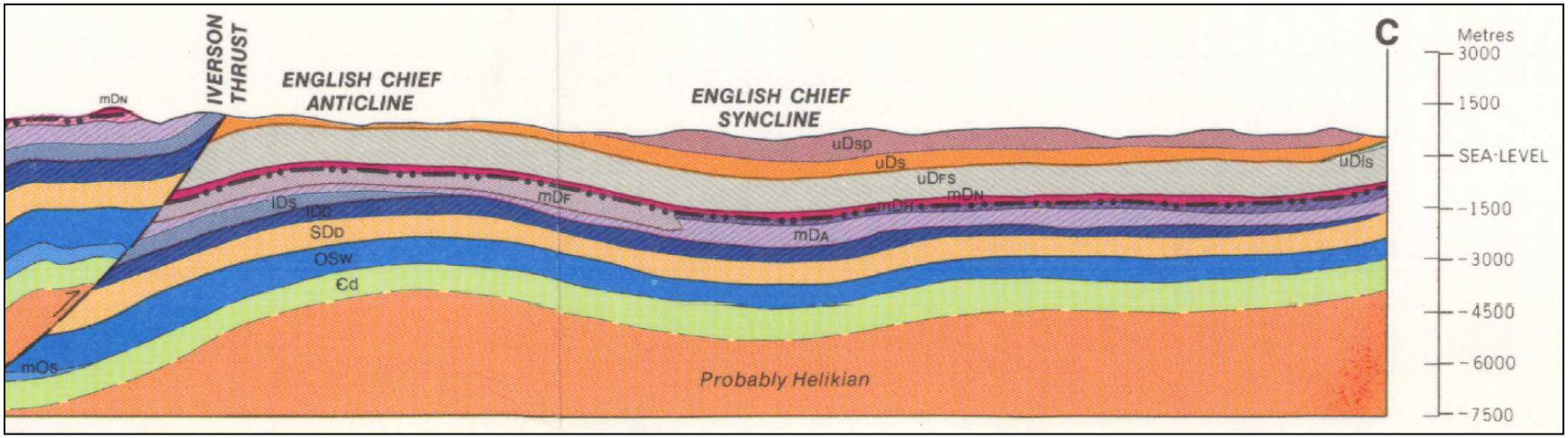

DEVONIAN

uDsP Sandstone, limestone, shale

uDIs Limestone, massive bedded, reefy

uDs Sandstone, siltstone, shale, limestone

uDFs FORT SIMPSON FORMATION: shale and mudstone, grey; siltstone, grey

LOWER DEVONIAN

IDs SOMBRE FORMATION: dolomite, cryptocrystalline to fine-grained

IDc CAMSELL FORMATION: massive breccias, cryptocrystalline limestone

ORDOVICIAN

mOs SUNBLOOD FORMATION: limestone, dark grey; dolomite, sandy

MIDDLE DEVONIAN

mDN Nahanni FORMATION: limestone, fine-to-medium-grained grey

mDF FUNERAL FORMATION: limestone, argillaceous; shale grey

mDA ARNICA FORMATION: dolomite, crypto-to fine-grained, banded dark grey and black weathering

SILURIAN AND DEVONIAN

SD_D DOLOMITE FORMATION: dolomite, limestone, siltstone, shale, grey, banded buff and brown weathering

OSw WHITTAKER FORMATION: limestone, dolomite massive

CAMBRIAN

Cd Dolomite, buff and orange, locally sandy

Appendix C

List of all discontinuities' orientation at the site of North Nahanni rockslide

Dip	Dip direction	Discontinuity type	Domain
29	355	Bedding	1
17	44	Bedding	1
22	18	Bedding	1
24	36	Bedding	1
18	34	Bedding	1
22	355	Bedding	1
23	24	Bedding	1
87	130	Joint	1
69	221	Joint	1
80	175	Joint	1
35	55	Bedding	2
32	45	Bedding	2
41	38	Bedding	2
35	35	Bedding	2
32	35	Bedding	2
32	55	Bedding	2
38	62	Bedding	2
45	68	Bedding	2
48	60	Bedding	2
38	36	Bedding	2
37	84	Bedding	2
40	35	Bedding	2
30	26	Bedding	2
33	70	Bedding	2
35	36	Bedding	2
30	50	Bedding	2
32	30	Bedding	2
35	21	Bedding	2
32	40	Bedding	2
40	40	Bedding	2
35	45	Bedding	2
28	38	Bedding	2
42	50	Bedding	2
34	24	Bedding	2
39	16	Bedding	2

Dip	Dip direction	Discontinuity type	Domain
36	28	Bedding	2
38	28	Bedding	2
30	41	Bedding	2
39	40	Bedding	2
31	26	Bedding	2
40	34	Bedding	2
40	34	Bedding	2
31	30	Bedding	2
38	37	Bedding	2
36	38	Bedding	2
42	56	Bedding	2
32	28	Bedding	2
30	34	Bedding	2
32	33	Bedding	2
32	48	Bedding	2
29	51	Bedding	2
44	55	Bedding	2
36	62	Bedding	2
34	55	Bedding	2
45	48	Bedding	2
44	50	Bedding	2
45	51	Bedding	2
44	38	Bedding	2
41	40	Bedding	2
36	33	Bedding	2
45	31	Bedding	2
37	22	Bedding	2
31	51	Bedding	2
32	51	Bedding	2
35	57	Bedding	2
29	24	Bedding	2
27	8	Bedding	2
34	48	Bedding	2
36	53	Bedding	2
42	69	Bedding	2
23	21	Bedding	2
33	30	Bedding	2
32	40	Bedding	2

Dip	Dip direction	Discontinuity type	Domain
47	55	Bedding	2
36	51	Bedding	2
46	32	Bedding	2
26	46	Bedding	2
37	58	Bedding	2
28	40	Bedding	2
27	46	Bedding	2
35	40	Bedding	2
29	30	Bedding	2
28	35	Bedding	2
26	47	Bedding	2
28	42	Bedding	2
35	43	Bedding	2
85	316	Joint	2
58	223	Joint	2
14	30	Bedding	3
16	62	Bedding	3
14	43	Bedding	3
18	62	Bedding	3
21	65	Bedding	3
7	79	Bedding	3
15	63	Bedding	3
21	64	Bedding	3
24	87	Bedding	3
10	111	Bedding	3
25	84	Bedding	3
21	84	Bedding	3
15	60	Bedding	3
16	82	Bedding	3
63	189	Bedding	3
19	162	Bedding	3
64	212	Bedding	3
40	194	Bedding	3
19	209	Bedding	3
12	202	Bedding	3
15	96	Bedding	3
23	196	Bedding	3
17	60	Bedding	3

Dip	Dip direction	Discontinuity type	Domain
12	67	Bedding	3
30	52	Bedding	3
28	60	Bedding	3
28	54	Bedding	3
54	42	Bedding	3
37	55	Bedding	3
33	78	Bedding	3
30	92	Bedding	3
25	30	Bedding	3
25	47	Bedding	3
30	45	Bedding	3
25	38	Bedding	3
22	39	Bedding	3
32	62	Bedding	3
25	35	Bedding	3
31	20	Bedding	3
24	50	Bedding	3
20	33	Bedding	3
23	41	Bedding	3
21	22	Bedding	3
22	20	Bedding	3
82	308	Joint	3
65	215	Joint	3
84	175	Joint	3
18	24	Bedding	4
17	21	Bedding	4
16	22	Bedding	4
17	21	Bedding	4
16	20	Bedding	4
17	27	Bedding	4
16	28	Bedding	4
18	23	Bedding	4
15	18	Bedding	4
20	16	Bedding	4
20	26	Bedding	4
16	28	Bedding	4
17	25	Bedding	4
19	24	Bedding	4

Dip	Dip direction	Discontinuity type	Domain
18	26	Bedding	4
19	40	Bedding	4
19	32	Bedding	4
20	33	Bedding	4
16	41	Bedding	4
18	27	Bedding	4
20	25	Bedding	4
19	27	Bedding	4
19	30	Bedding	4
18	38	Bedding	4
20	33	Bedding	4
20	39	Bedding	4
19	41	Bedding	4
21	36	Bedding	4
19	34	Bedding	4
19	28	Bedding	4
18	37	Bedding	4
18	34	Bedding	4
19	33	Bedding	4
21	33	Bedding	4
21	33	Bedding	4
21	28	Bedding	4
24	32	Bedding	4
18	24	Bedding	4
22	33	Bedding	4
18	24	Bedding	4
22	33	Bedding	4
21	44	Bedding	4
20	30	Bedding	4
22	27	Bedding	4
20	30	Bedding	4
21	34	Bedding	4
22	35	Bedding	4
23	38	Bedding	4
22	37	Bedding	4
21	27	Bedding	4
23	29	Bedding	4
23	35	Bedding	4

Dip	Dip direction	Discontinuity type	Domain
24	35	Bedding	4
22	40	Bedding	4
23	34	Bedding	4
20	31	Bedding	4
90	48	Joint	4

Appendix D

Original GSI chart (taken from Hoek and Brown, 1997)

GSI values ranging between 70 and 75 can be assigned to the limestone rock of the Middle Devonian Nahanni Formation.

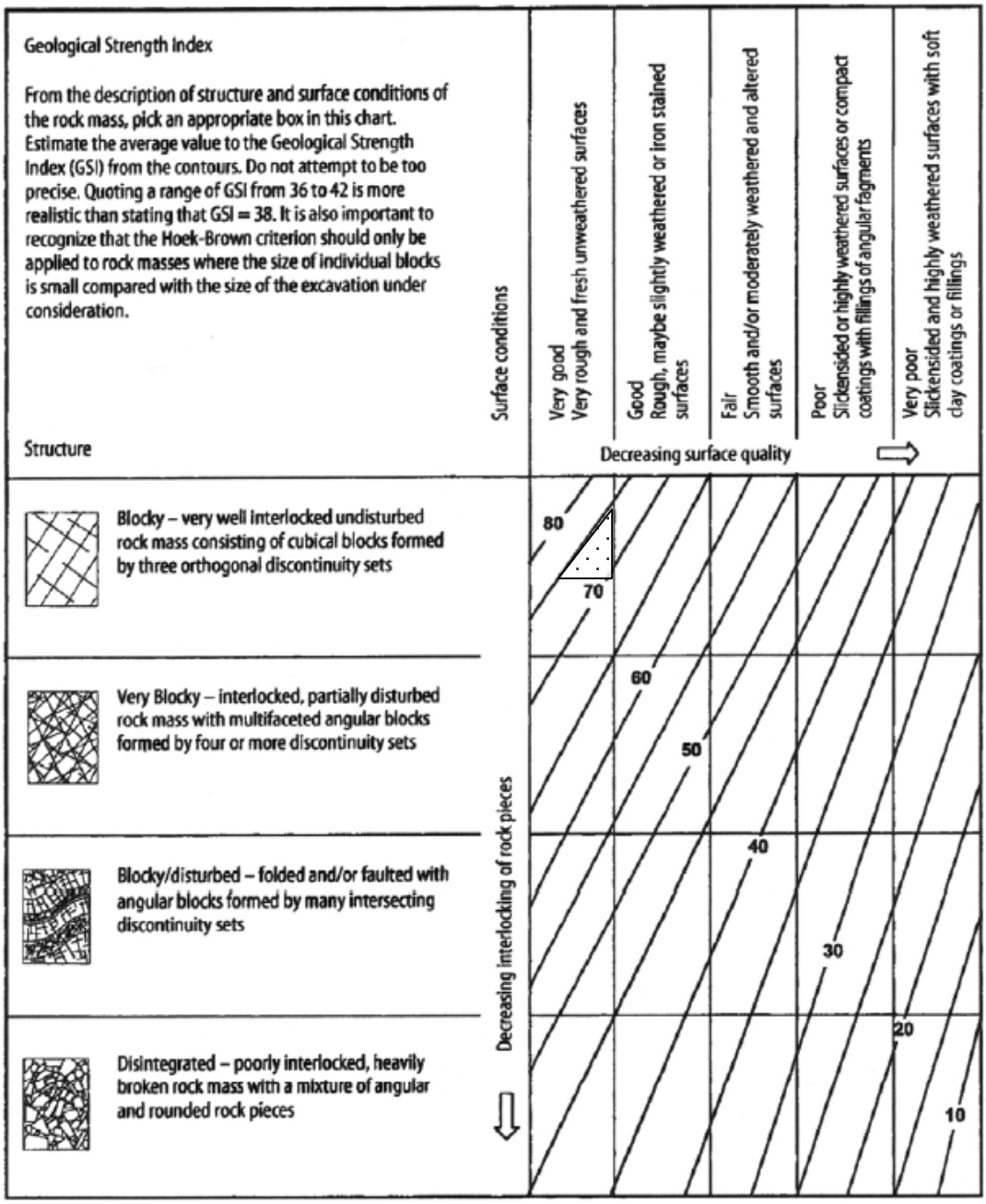

References

Abrahamson, N. A. and Silva, W. J., 1997. Empirical Response Spectral Attenuation Relations for Shallow Crustal Earthquakes. Seismological Research Letters. 68, 94-127.

Aki, K., 1967. Scaling Law of Seismic Spectrum. Journal of Geophysical Research. 72, 1217-1231.

Allen, T. I., Marano, K. D., Earle, P. S., Wald, D. J., 2009. PAGER-CAT: A Composite Earthquake Catalog for Calibrating Global Fatality Models. Seismological Research Letters. 80, 57-62.

Bak, P., 1996. How Nature Works: The Science of Self-Organized Criticality. Copernicus, New York.

Bak, P., Tang, C., Wiesenfeld, K., 1987. Self-Organized Criticality - an Explanation of 1/f Noise. Physical Review Letters. 59, 381-384.

Basham, P. W., Weichert, D. H., Anglin, F. M., Berry, M. J., 1985. New Probabilistic Strong Seismic Ground Motion Maps of Canada. Bulletin of the Seismological Society of America. 75, 563-595.

Benko, B. and Stead, D., 1998. The Frank slide: a reexamination of the failure mechanism. Canadian Geotechnical Journal. 35, 299-311.

Bhasin, R. and Kaynia, A. M., 2004. Static and dynamic simulation of a 700-m high rock slope in western Norway. Engineering Geology. 71, 213-226.

Bieniawski, Z. T., 1978. Determining rock mass deformability: experience from case histories. International Journal of Rock Mechanics and Mining Sciences and Geomechanics Abstracts. 15, 237-247.

Biot, M. A., 1941. A mechanical analyzer for the prediction of earthquake stresses. Bulletin of the Seismological Society of America. 31, 151-171.

Boore, D. M., Joyner, W. B., Fumal, T. E., 1997. Equations for Estimating Horizontal Response Spectra and Peak Acceleration from Western North American Earthquakes: A Summary of Recent Work. Seismological Research Letters. 68, 128-153.

Boore, D. M., 2005. Equations for estimating horizontal response spectra and peak acceleration from western north American earthquakes: A summary of recent work (vol 68, pg 128, 1997). Seismological Research Letters. 76, 368-369.

Boore, D. M. and Atkinson, G. M., 1989. Spectral Scaling of the 1985 to 1988 Nahanni, Northwest-Territories, Earthquakes. Bulletin of the Seismological Society of America. 79, 1736-1761.

Boore, D. M. and Atkinson, G. M., 2008. Ground-motion prediction equations for the average horizontal component of PGA, PGV, and 5%-damped PSA at spectral periods between 0.01 s and 10.0 s. Earthquake Spectra. 24, 99-138.

Bouhadad, Y., Benhamouche, A., Bourenane, H., Ouali, A. A., Chikh, M., Guessoum, N., 2010. The Laalam (Algeria) damaging landslide triggered by a moderate earthquake (Mw = 5.2). Natural Hazards. 54, 261-272.

Bruce, I. G., Cruden, D. M., Eaton, T. M., 1989. Use of a tilting table to determine the basic friction angle of hard rock samples. Canadian Geotechnical Journal. 26, 474-479.

Cai, M., Kaiser, P. K., Uno, H., Tasaka, Y., Minami, M., 2004. Estimation of rock mass deformation modulus and strength of jointed hard rock masses using the GSI system. International Journal of Rock Mechanics and Mining Sciences. 41, 3-19.

Cetin, K. O., Isik, N., Unutmaz, B., 2004. Seismically induced landslide at Degirmendere Nose, I˙zmit bay during Kocaeli (I˙zmit) Turkey earthquake. Soil Dynamics and Earthquake Engineering. 24, 189-197.

Chael, E. P., 1987. Spectral Scaling of Earthquakes in the Miramichi Region of New-Brunswick. Bulletin of the Seismological Society of America. 77, 347-365.

Chen, T., Lin, M., Hung, J., 2004. Pseudostatic analysis of Tsao-Ling rockslide caused by Chi-Chi earthquake. Engineering Geology. 71, 31-47.

Chigira, M. and Yagi, H., 2006. Geological and geomorphological characteristics of landslides triggered by the 2004 Mid Niigta prefecture earthquake in Japan. Engineering Geology. 82, 202-221.

Chigira, M., Wang, W., Furuya, T., Kamai, T., 2003. Geological causes and geomorphological precursors of the Tsaoling landslide triggered by the 1999 Chi-Chi earthquake, Taiwan. Engineering Geology. 68, 259-273.

Chigira, M., Wu, X., Inokuchi, T., Wang, G., 2010. Landslides induced by the 2008 Wenchuan earthquake, Sichuan, China. Geomorphology. 118, 225-238.

Choy, G. L. and Boatwright, J., 1988. Teleseismic and near field analysis of the Nahanni earthquakes in the Northwest Territories, Canada. Bulletin of the Seismological Society of America. 78, 1627-1652.

Clough, R. W. and Chopra, A. K., 1966. Earthquake stress analysis in earth dams. ASCE Journal of the Engineering Mechanics Division. 92, 197-211.

Cui, P., Chen, X., Zhu, Y., Su, F., Wei, F., Han, Y., Liu, H., Zhuang, J., 2011. The Wenchuan Earthquake (May 12, 2008), Sichuan Province, China, and resulting geohazards. Natural Hazards. 56, 19-36.

Cundall, P.A., 1987. Distinct element models of rock and soil structure, in: Brown, E. T. (Ed.), Analytical and Computational Methods in Engineering Rock Mechanics. George Allen and Unwin, London, pp. 129-163.

Douglas, R. J. W. and Norris, D. K., 1976. Root River, District of Mackenzie. Map 1376A ed. Geological Survey of Canada.

Dunning, S. A., Mitchell, W. A., Rosser, N. J., Petley, D. N., 2007. The Hattian Bala rock avalanche and associated landslides triggered by the Kashmir Earthquake of 8 October 2005 RID A-1820-2010. Engineering Geology. 93, 130-144.

Earthquakes Canada, GSC, earthquake search (on-line bulletin). Retrieved March 22, 2012, from http://www.earthquakescanada.nrcan.gc.ca/stndon/NEDB-BNDS/bull-eng.php.

Eberhardt, E., Stead, D., Coggan, J. S., 2004. Numerical analysis of initiation and progressive failure in natural rock slopes—the 1991 Randa rockslide. International Journal of Rock Mechanics and Mining Sciences. 41, 69-87.

Evans, S. G., Aitken, J. D., Wetmiller, R. J., Horner, R. B., 1987. A rock avalanche triggered by the October 1985 North Nahanni earthquake, District of Mackenzie, N.W.T. Canadian Journal of Earth Sciences. 24, 176-184.

Evans, S. G., Roberts, N. J., Ischuk, A., Delaney, K. B., Morozova, G. S., Tutubalina, O., 2009. Landslides triggered by the 1949 Khait earthquake, Tajikistan, and associated loss of life RID G-2008-2011. Engineering Geology. 109, 195-212.

Forlati, F., Gioda, G., Scavia, C., 2001. Finite Element Analysis of a Deep-seated Slope Deformation. Rock Mechanics and Rock Engineering. 34, 135-159.

Fukuoka, H., Wang, G., Sassa, K., Wang, F. W., Matsumoto, T., 2004. Earthquake-induced rapid long-traveling flow phenomenon: May 2003 Tsukidate landslide in Japan. Landslides. 1, 151-155.

Giardini, D., Grunthal, G., Shedlock, K. M., Zhang, P., 1999. The GSHAP Global Seismic Hazard Map. Ann. Geofis. 42, 1225-1230.

Gutenberg, B. and Richter, C. F., 1956. Earthquake magnitude, intensity, energy, and acceleration. Bulletin of Seismological Society of America. 46, 105-145.

Hancox, G. T., Cox, S. C., Turnbull, I. M., Crozier, M. J., 2003. Reconnaissance studies of landslides and other ground damage caused by the MW7.2 Fiordland earthquake of 22 August 2003.

Hanks, T. C. and Kanamori, H., 1979. A moment magnitude scale. Journal of Geophysical Research. 84, 2348-2350.

Havenith, H. B., Strom, A., Calvetti, F., Jongmans, D., 2003. Seismic triggering of landslides. Part B: Simulation of dynamic failure processes. Natural Hazards and Earth System Sciences. 3, 663-682.

Henkel, D. J., 1967. Local geology and the stability of natural slopes. ASCE Journal of the Soil Mechanics and Foundations Division. 93, 437-446.

Hoek, E., 1994. Strength of rock and rock masses. International Society for Rock Mechanics News Journal. 2, 4-16.

Hoek, E. and Brown, E. T., 1997. Practical estimates of rock mass strength. International Journal of Rock Mechanics and Mining Sciences. 34, 1165-1186.

Housner, G. W., 1941. Calculation of the response of an oscillator to arbitrary ground motion. Bulletin of Seismological Society of America. 32, 143-149.

Hu, X. Q. and Evans, S. G., 1993. Stability and Movement of the Earthquake Triggered North Nahanni Rockslide. Unpublished Contract Report.

Huang, R. Q. and Li, W. L., 2009. Analysis of the geo-hazards triggered by the 12 May 2008 Wenchuan Earthquake, China. Bulletin of Engineering Geology and the Environment. 68, 363-371.

Itasca Consulting Group. Inc., 2011. UDEC Version 5.0. Users Manuals Itasca Consulting Group Inc., Minneapolis.

Jibson, R. W., Harp, E. L., Schulz, W., Keefer, D. K., 2006. Large rock avalanches triggered by the M 7.9 Denali Fault, Alaska, earthquake of 3 November 2002. Engineering Geology. 83, 144-160.

Jibson, R. W., 2011. Methods for assessing the stability of slopes during earthquakes—A retrospective. Engineering Geology. 122, 43-50.

Jibson, R. W., Crone, A. J., Harp, E. L., Baum, R. L., Major, J. J., Pullinger, C. R., Demetrio Escobar, C., Martinez, M., Smith, M. E., 2004. Landslides triggered by the 13 January and 13 February 2001 earthquakes in El Salvador. Natural Hazards in El Salvador. 375, 69-88.

Keefer, D. K., 1984. Landslides Caused by Earthquakes. Geological Society of America Bulletin. 95, 406-421.

Keefer, D. K., 1994. The Importance of Earthquake-Induced Landslides to Long-Term Slope Erosion and Slope-Failure Hazards in Seismically Active Regions. Geomorphology. 10, 265-284.

Keefer, D. K., 2002. Investigating landslides caused by earthquakes - A historical review. Surveys in Geophysics. 23, 473-510.

Keefer, D. K. and Moseley, M. E., 2004. Southern Peru desert shattered by the great 2001 earthquake: implications for paleoseismic and paleo-El Niño southern oscillation records. PNAS. 101, 10878-10883.

Keefer, D. K., Wartman, J., Navarro Ochoa, C., Rodriguez-Marek, A., Wieczorek, G. F., 2006. Landslides caused by the M 7.6 Tecoman, Mexico earthquake of January 21, 2003. Engineering Geology. 86, 183-197.

Kobayashi, Y., 1981. Causes of fatalities in recent earthquakes in Japan. Journal Disaster Science. 3, 15-22.

Kramer, S.L., 1996. Geotechnical Earthquake Engineering. Prentice Hall, Upper Saddle River, N.J.

Lin, C., Shieh, C., Yuan, B., Shieh, Y., Liu, S., Lee, S., 2004. Impact of Chi-Chi earthquake on the occurrence of landslides and debris flows: example from the Chenyulan River watershed, Nantou, Taiwan. Engineering Geology. 71, 49-61.

Malamud, B. D. and Turcotte, D. L., 1999. Self-organized criticality applied to natural hazards. Natural Hazards. 20, 93-116.

Malamud, B. D., Turcotte, D. L., Guzzetti, F., Reichenbach, P., 2004. Landslides, earthquakes, and erosion. Earth and Planetary Science Letters. 229, 45-59.

McAdoo, B. G., Fritz, H. M., Jackson, K. L., Kalligeris, N., Kruger, J., Bonte-Grapentin, M., Moore, A. L., Rafiau, W. B., Billy, D., Tiano, B., 2008. Solomon Islands tsunami, one year later. Eos, Transactions, American Geophysical Union. 89, 169-170.

McCalpin, J. P. and Thakkar, M. G., 2003. 2001 Bhuj-Kachchh earthquake: surface faulting and its relation with neotectonics and regional structures, Gujarat, western India. Annals Geophysics. 46, 937-956.

McMartin, I. and Evans, S. G., 1994. North Nahanni rockslide, report on macro and micro structural data. Geological Survey of Canada.

Meunier, P., Hovius, N., Haines, A. J., 2007. Regional patterns of earthquake-triggered landslides and their relationto ground motion. Geophysical Research Letters. 34, L20408.

Miyagi, T., Yamashina, S., Esaka, F., Abe, S., 2011. Massive landslide triggered by 2008 Iwate–Miyagi inland earthquake in the Aratozawa Dam area, Tohoku, Japan. Landslides. 8, 99-108.

Newman, W. I. and Turcotte, D. L., 2002. A simple model for the earthquake cycle combining self-organized complexity with critical point behavior. Nonlinear Processes in Geophysics. 9, 453-461.

Newmark, N. M., 1965. Effects of earthquakes on dams and embankments. Geotechnique. 15, 139-159.

Nigam, N.C., Jennings, P.C. (Eds.), 1968. Digital Calculation of Response Spectra from Strong-Motion Earthquake Records. California Institute of Technology, Pasadena, U.S.A.

Owen, L. A., Kamp, U., Khattak, G. A., Harp, E. L., Keefer, D. K., Bauer, M. A., 2008. Landslides triggered by the 8 October 2005 Kashmir earthquake. Geomorphology. 94, 1-9.

Rodriguez, C. E., Bommer, J. J., Chandler, R. J., 1999. Earthquake-induced landslides: 1980-1997. Soil Dynamics and Earthquake Engineering. 18, 325-346.

Rosyidi, S. A. P., Fahmi, A., Nazib, F. M., Raihan, T., 2011. Lesson Learned from Road Infrastructure Deterioration Caused by Earthquake 7.6 M_W and 6.2 M_W Padang, September 30, 2009, September 30, 2009. Paper presented at Advances in Unsaturated Soil, Geo-Hazard, and Geo-Environmental Engineering (GSP 217) Proceedings of the 2011 GeoHunan International Conference.

Sarkar, I., Pachauri, A. K., Israil, M., 2000. On the damage caused by the Chamoli earthquake of March 29, 1999. Journal of Asian Earth Sciences. 19, 129-134.

Sato, H. P. and Harp, E. L., 2009. Interpretation of earthquake-induced landslides triggered by the 12 May 2008, M7.9 Wenchuan earthquake in the Beichuan area, Sichuan Province, China using satellite imagery and Google Earth. Landslides. 6, 153-159.

Sepúlveda, S., Serey, A., Lara, M., Pavez, A., Rebolledo, S., 2010. Landslides induced by the April 2007 Aysén Fjord earthquake, Chilean Patagonia. Landslides. 7, 483-492.

Terzhagi, K., 1950. Mechanism of landslides, in: In: Paige, S. (Ed.), Application of Geology to Engineering Practice. Geological Society of America, New York, pp. 83-123.

Turcotte, D. L., 1999. Self-organized criticality. Reports on Progress in Physics. 62, 1377-1429.

USGS., 2012. Earthquake Hazards Program. http://earthquake.usgs.gov/earthquakes/eqarchives/epic/

Utsu, T., 2002. A list of deadly earthquakes in the World: 1500-2000, in: Lee, W. K., Kanamori, H., Jennings, P. C., Kisslinger, C. (Eds.), International handbook of earthquake engineering and seismology. Academic Press, Amsterdam, pp. 691-717.

Wasowski, J., Keefer, D. K., Lee, C., 2011. Toward the next generation of research on earthquake-induced landslides: Current issues and future challenges. Engineering Geology. 122, 1-8.

Weichert, D. H., Wetmiller, R. J., Munro, P., 1986. Vertical earthquake acceleration exceeding 2 *g*? The case of the missing peak. Bulletin of the Seismological Society of America. 76, 1473-1478.

Wetmiller, R. J., Horner, R. B., Hasegawa, H. S., North, R. G., Lamontagne, M., Weichert, D. H., Evans, S. G., 1988. An Analysis of the 1985 Nahanni Earthquakes. Bulletin of the Seismological Society of America. 78, 590-616.

Yagi, H., Sato, G., Higaki, D., Yamamoto, M., Yamasaki, T., 2009. Distribution and characteristics of landslides induced by the Iwate-Miyagi Nairiku Earthquake in 2008 in Tohoku District, Northeast Japan. Landslides. 6, 335-344.

Yin, Y., Wang, F., Sun, P., 2009. Landslide hazards triggered by the 2008 Wenchuan earthquake, Sichuan, China. Landslides. 6, 139-152.